Acta Materialia 289 (2025) 120932

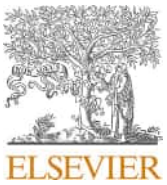

Contents lists available at ScienceDirect

Acta Materialia

journal homepage: www.elsevier.com/locate/actamat

Thermodynamics-guided design of sustainable secondary Al-Si alloys for enhanced Fe-impurity tolerance and optimized Mn doping

Waleed Mohammed *, Xinren Chen *, Dirk Ponge, Dierk Raabe

Max Planck Institute for Sustainable Materials, Düsseldorf 40237, Germany

ARTICLE INFO

Keywords:
Sustainable alloys
Green aluminum
Thermodynamics
Intermetallic phases
Microstructure formation

ABSTRACT

The accumulation of Fe impurities throughout the lifecycle of secondary scrap-based Al-Si alloys can degrade their mechanical properties. This often necessitates neutralizing the detrimental Fe contamination with Mn addition. However, some reports suggest that specific ranges of Fe concentrations have minimal deleterious effects, and Mn introduction can yield only minor or even adverse impacts. Our working hypothesis is that the tolerances for Fe and Mn can be rationalized based on the underlying microstructure-property relationships. Calculations of non-equilibrium solidification paths, evaluations of precipitation driving force, and estimations of interfacial energy were employed to predict the resulting microstructure characteristics. The findings indicate that in moderately-contaminated alloys with 0.8 wt.% Fe, near-eutectic compositions demonstrate greater Fe tolerance than far-from-eutectic alloys. This is because near-eutectic alloys require less undercooling to promote the preferred formation of the metastable Chinese-script α phase and inhibit the undesired platelet-shaped β and δ phases. Conversely, in severely-contaminated alloys with 2.0 wt.% Fe, far-from-eutectic compositions display better Fe tolerance. The enhanced tolerance is attributed to the higher nucleation rate of the platelet β phase in far-from-eutectic alloys, leading to a more refined size distribution. Sufficient undercooling of the platelet phases facilitates the formation of the Chinese-script α phase in moderately-contaminated alloys and the polyhedral γ phase in severely-contaminated alloys. Consequently, Mn addition for neutralizing Fe contamination becomes redundant. This study investigates how Si, Fe, Mn, and cooling rate affect the formation of Fe-rich intermetallic phases. Moreover, it provides general recommendations for designing sustainable Al-Si alloys with less compromised properties.

1. Introduction

Primary Al production accounts for about 3% of all global greenhouse gas emissions, due to the energy-intensive electrolysis process [1,2]. The rising demand for sustainable design in the industry has sparked a trend of utilizing secondary materials [3–5]. Al recycling can save up to 95% of the energy used per ton of Al [1,2]. However, the recycling process entails remelting Al scraps of various compositions, which leads to the enrichment of impurity elements in the secondary alloys [6–9]. This may alter the physical metallurgy characteristics and impact the properties [1,2,4,7]. Furthermore, the removal of these impurities is frequently an expensive, energy-intensive, and time-consuming process [1,10].

The most common impurity element in Al recycling is Fe [1,10–12]. Due to the limited solubility of Fe in Al solid solutions, complex iron intermetallic (Fe-IMC) phases can develop in the microstructure [1,10,12]. In the Al-Fe-Si system, there exist ten stable ternary Fe-IMC phases: τ_1 or τ_9 ($Al_2Fe_3Si_3$), τ_2 or γ (Al_3FeSi), τ_3 (Al_2FeSi), τ_4 or δ (Al_4FeSi_2), τ_5 or α (Al_8Fe_2Si), τ_6 or β ($Al_{4.5}FeSi$), τ_7 ($Al_3Fe_2Si_3$), τ_8 ($Al_2Fe_3Si_4$), τ_{10} ($Al_9Fe_4Si_3$), and τ_{11} (Al_5Fe_2Si) [13–15]. The most commonly observed phases in industrial casting include the monoclinic β-$Al_{4.5}FeSi$, tetragonal δ-Al_4FeSi_2, and hexagonal α-Al_8Fe_2Si [1,10,12]. In addition, a metastable α-AlFeSi phase was observed during rapid cooling [16–19]. This phase has a cubic crystal structure and manifests in varying stoichiometries, such as $Al_{14}Fe_3Si_2$ [18,19]. The phase equilibria become intricate when Mn is introduced to the system. One particularly important phase in the Al-Fe-Mn-Si system is the cubic α-$Al_{15}(Fe,Mn)_3Si_2$ [1,10,12]. Table 1 summarizes the crystallography data of the aforementioned Fe-IMC phases.

Fe-IMC phases demonstrate different morphologies based on their chemical composition, formation temperature, and solidification conditions. Both β-$Al_{4.5}FeSi$ and δ-Al_4FeSi_2 exhibit a platelet-like

* Corresponding authors.
E-mail addresses: w.mohammed@mpie.de (W. Mohammed), x.chen@mpie.de (X. Chen).

https://doi.org/10.1016/j.actamat.2025.120932
Received 6 July 2024; Received in revised form 10 March 2025; Accepted 11 March 2025
Available online 13 March 2025

Table 1
Ternary Fe-IMC phases in the Al-Fe-Si system, together with the quaternary α-Al (Fe,Mn)Si phase found in the Al-Fe-Mn-Si system.

Fe-IMC phase	Composition *	Space group	Lattice parameter, Å	Ref. / Notes
τ_1 or τ_9	$Al_2Fe_3Si_3$	Triclinic $P\bar{1}$	$a = 4.651$, $b = 6.326$, $c = 7.499$, $\alpha = 101.375°$, $\beta = 105.923°$, $\gamma = 101.237°$	[20]
τ_2 or γ	Al_3FeSi	Trigonal $R\bar{3}$	$a = 10.199$, $c = 19.532$	[21,22]
		Monoclinic	$a = 17.8$, $b = 10.25$, $c = 8.9$, $\beta = 132°$	No space group was reported [23]
τ_3	Al_2FeSi	Orthorhombic Cmma	$a = 7.995$, $b = 15.162$, $c = 15.221$	[24]
τ_4 or δ	Al_4FeSi_2	Tetragonal I4/mcm	$a = 6.07$, $c = 9.5$	[25]
τ_5 or α	Al_8Fe_2Si	Hexagonal $P6_3/mmc$	$a = 12.345$, $c = 26.21$	[26]
τ_6 or β	$Al_{4.5}FeSi$	Monoclinic A2/a	$a = 6.161$, $b = 6.175$, $c = 20.813$, $\beta = 90.42°$	[27]
τ_7	$Al_3Fe_2Si_3$	Monoclinic $P2_1/n$	$a = 7.179$, $b = 8.354$, $c = 14.455$, $\beta = 93.80°$	[28]
τ_8	$Al_2Fe_3Si_4$	Orthorhombic Cmcm	$a = 3.669$, $b = 12.385$, $c = 10.147$	[20]
τ_{10}	$Al_9Fe_4Si_3$	Hexagonal	$a = 15.518$, $c = 7.297$	No space group was reported [29].
τ_{11}	Al_5Fe_2Si	Hexagonal $P6_3/mmc$	$a = 7.509$, $c = 7.594$	[30]
Metastable α	$Al_{14}Fe_3Si_2$	Cubic $Im\bar{3}$	$a = 12.53$	[19,22]. Proposed as a near isomorph to the α-AlMnSi phase with $a = 12.68$ Å [31,32]. Although the crystal structure was reported as $Im\bar{3}$ (bcc), there was also a suggestion that it could consist of two interpenetrating $Pm\bar{3}$ (sc) cells [32].
α-Al(Fe, Mn)Si	$Al_{15}(Fe, Mn)_3Si_2$	Cubic $Pm\bar{3}$	$a = 12.65$	Isomorphic with α-AlMnSi phase [33].
		Cubic $Im\bar{3}$	$a = 12.56$	[25]. The transition from $Im\bar{3}$ (bcc) to $Pm\bar{3}$ (sc) depends on Mn/Fe ratio [34, 35].

* Each composition refers to the approximate stoichiometry, as Fe-IMC phases typically exhibit stoichiometry ranges.

morphology, which appears as needles in 2D micrographs. On the other hand, α_H-Al_8Fe_2Si and α_C-$Al_{15}(Fe, Mn)_3Si_2$ (α_H and α_C were used for clarity) show two distinct morphologies. They assume a polyhedral shape as primary phases. Alternatively, they display a branched morphology that, in 2D sections, resembles a Chinese-script when they form through a eutectic reaction with the Al phase [1,10,12]. The size, morphology, and volume fraction of these Fe-IMC phases have a pronounced effect on mechanical properties.

Increasing Fe levels worsen the ductility of Al-Si alloys, typically leading to a decrease in the tensile strength, while the yield strength remains unaffected [1,10,12,36–40]. Mohamed et al. [38] reported that increasing the Fe content from 0.4 wt.% to 0.9 wt.% in an Al-11wt.%Si alloy reduced the elongation and tensile strength by 32% and 5%, respectively. Similarly, Malavazi et al. [39] observed a 67% and 24% drop in elongation and tensile strength, respectively, with a rise in Fe level from 0.8 wt.% to 1.2 wt.% in an Al-9wt.%Si alloy. This detrimental impact stems from the formation of brittle Fe-IMC phases, particularly the β phase. Due to its high aspect ratio platelet morphology, the β phase typically acts as a stress concentration and crack initiation site [1,10,12,36]. Besides morphology, the size of the Fe-IMC phases significantly influences the mechanical properties. Bjurenstedt et al. [41] observed that alloys with varying Fe contents but identical platelet β sizes showed similar ultimate tensile strength and elongation despite varying platelet β phase fraction.

In contrast to the common belief about the negative effect of Fe, a few studies have interestingly shown that controlled enrichment with a certain amount of Fe has only a slight detrimental impact [38,39,42,43]. This implies that the mechanical properties of Al-Si alloys do not generally or consistently decline as the Fe concentration rises; instead, they deteriorate sharply once surpassing a critical Fe content. Taylor [11] introduced the notion of critical Fe content, correlating it with the β phase formation. To support this rationale, the author used a liquidus projection of the Al-Fe-Si system to elucidate that increasing Si content in hypoeutectic Al-Si alloys raises the maximum Fe level beyond which the β phase forms before the ternary eutectic point.

To counter the deleterious effect of Fe, one solution is to introduce so-called "Fe corrector" elements, such as Mn [1,10,12,36]. Previous studies have thoroughly investigated the impact of Mn correction; however, there appear to be inconsistencies in the literature. While some studies report significant improvements in mechanical properties with the addition of Mn, others claim negligible or negative impacts [44–51]. Baldan et al. [49] incorporated Mn to an Al-9wt.%Si-0.8wt.%Fe alloy and observed an elongation rise from 4.7 ± 0.8% to 6.9 ± 0.7% with 0.2wt.% Mn. Further Mn addition led to a slight decrease in elongation, reaching 5.6 ± 1.7% at 0.7wt.% Mn. Song et al. [51] reported a 168% elongation enhancement when 0.73wt.% Mn was introduced to an Al-7wt.%Si-1.2wt.%Fe alloy. However, higher Mn concentrations reduced both elongation and ultimate tensile strength. These inconsistencies and even contradictory observations underline that the precise amount of Mn required to neutralize the detrimental effects of Fe is still not well established and understood [51,52]. This has been ascribed to the complex interaction of several factors affecting the Mn correction process, such as cooling rate, Fe/Mn ratio, and the presence of further alloying elements [51–53].

Anticipating the formation of Fe-IMC phases during solidification is crucial for microstructure control. The Scheil–Gulliver solidification model [54,55] is extensively used to analyze solidification behavior and elucidate the influence of alloy composition on phase formation. The model assumes infinitely fast diffusion in the liquid phase, negligible diffusion in the solid phases, and local equilibrium at the solid/liquid interface. In addition, nucleation of the solid phases is instantaneous and occurs under the assumption of no undercooling [54,55]. These assumptions yield an upper limit for solute partitioning between the liquid and solid phases. The segregation of solute into the liquid then follows the so-called Scheil equation:

$$(1-k)\cdot C_L \cdot df_s = (1-f_s)\cdot dC_L \quad (1)$$

where k is the equilibrium partition coefficient, C_L is the concentration of a solute in the residual liquid, df_s is the incremental increase in solid

fraction, f_s is the solid fraction, and dC_L is the increment of the solute concentration in the residual liquid. Despite the effectiveness of the Scheil–Gulliver model in estimating solidification paths, the predicted Fe-IMC phases frequently deviate from experimental observations [16,18,56,57]. For example, Becker et al. [57] observed the formation of the δ-Al_4FeSi_2 phase instead of the β-$Al_{4.5}FeSi$ phase, and the β-$Al_{4.5}FeSi$ phase instead of the α-Al_8Fe_2Si phase, during the solidification of Al-Si-Fe alloys at elevated cooling rates. These findings contradict the upper bound predictions made by the Scheil calculations. This discrepancy is attributed to the simplified assumptions behind the Scheil–Gulliver model. Therefore, it is important to refine the model to address its shortcomings with respect to the current study targets.

The objective of this study is to develop a systemic understanding of the interplay between Si content, Fe impurity, Mn doping, and casting parameters in influencing the microstructure formation and mechanical properties of secondary Al-Si alloys. We use thermodynamic methods and experimental validation to address two key questions: Which Al-Si alloys exhibit greater tolerance to Fe? Under what conditions is Mn addition necessary and even beneficial to neutralize the negative effects of Fe?

2. Methods

2.1. Fe and Mn tolerance in Al-Si alloys

Impurity tolerance refers to the capacity of an alloy to accommodate varying amounts of impurities without experiencing an abrupt or unpredictable deterioration in its properties. The conventional method for assessing the Fe and Mn tolerance starts with equilibrium and non-equilibrium solidification path calculations for a certain set of compositions to predict the occurrence of Fe-IMC phases. These calculations are subsequently validated through systematic casting experiments where Fe and Mn contents are systematically varied, and the resulting microstructural changes are compared with the predictions [51,53,57,58]. However, this conventional method suffers from limitations. Firstly, the calculations are restricted to the narrow composition ranges investigated experimentally. Secondly, discrepancies in the formation of Fe-IMC phases often arise between calculated and experimental results without thorough exploration into the underlying thermodynamic and kinetic reasons. As a result, reliably predicting the formation of Fe-IMC phases under different alloying and cooling conditions based on well-established thermodynamic and kinetic principles remains challenging. In this work, a different approach was adopted. A series of calculations were performed to identify the Al-Si-Fe-Mn compositions that meet specific predefined criteria. This method eliminates the necessity to present and analyze a vast set of equilibrium phase diagrams and non-equilibrium solidification paths. Additionally, specific thermodynamic and kinetic metrics were employed to predict microstructure formation. These metrics enable identifying both equilibrium and non-equilibrium Fe-IMC phases that may arise within the microstructure, in addition to the solidification stages at which these phases are likely to form. Consequently, this offers qualitative insights into their predicted size distribution and assumed morphology. This approach provides a holistic view of the possible scenarios for microstructure formation without the need for tedious casting experiments.

Our approach started by proposing criteria for Fe and Mn tolerance in Al-Si alloys based on certain microstructure-property relationships. As explained earlier, coarse and brittle phases within the alloy matrix can compromise the ductility. Therefore, the targeted microstructure with high Fe and Mn tolerance should encompass a high phase fraction as possible of refined Fe-IMC phases without the presence of coarse Fe-IMC particles. To implement these criteria into the thermodynamic modelling step, we need to initially define thermodynamically-informed critical limits for Fe and Mn contents. These critical contents were inspired by the equilibrium phase diagram. The possible microstructure formation scenarios for Al-Si alloys with Fe and Mn, assuming equilibrium solidification conditions, were postulated based on the equilibrium phase diagram and literature reports [42,47,50,51,53,57,58]. For instance, these scenarios are depicted in Fig. 1. Figs. 1(a) and 1(b) illustrate simplified vertical sections (isopleths) of the quaternary Al-Si-Fe-Mn system for two exemplary compositions: a moderately Fe-contaminated alloy (11wt.%Si-0.7wt.%Fe-Xwt.%Mn) and a severely Fe-contaminated alloy (11wt.%Si-1.4wt.%Fe-Xwt.%Mn). In moderately Fe-contaminated Al-Si alloys, Fe-IMC phases become thermodynamically stable at the later stages of solidification after the formation of the Al dendrites. Conversely, in severely Fe-contaminated Al-Si alloys, Fe-IMC phases become thermodynamically stable at the onset of solidification and form as primary crystals before Al dendrites formation. This categorization into moderately and severely contaminated alloys based on equilibrium phase stability and similarities in non-equilibrium solidification paths simplifies the complex relationship between alloy chemistry, microstructure, and resulting properties and offers a more holistic insight into the alloy design space. Each potential microstructure formation scenario, presented in Figs. 1(c)-1(j), corresponds to a specific composition range within these phase diagrams. By analyzing these scenarios, the microstructure in Fig. 1(c) aligns with our proposed criteria for Fe and Mn tolerance. Accordingly, the critical Fe and Mn contents were determined as the maximum concentrations of both Fe and Mn that inhibit the occurrence of Fe-IMC phases during the early stages of solidification and restrict their formation to the final complex eutectic reaction at the end of solidification. When the Fe and Mn contents fall below critical levels (Fig. 1(c)), the time available for crystal growth is limited. Therefore, this refines the size of the Fe-IMC phases and concurrently reduces the phase fraction of the detrimental platelet-shaped phases due to the presence of Mn. Thus, higher critical Fe and Mn contents generally indicate larger impurity tolerance. Exceeding the critical Mn content can reduce the phase fraction of the fine platelet β-$Al_{4.5}FeSi$ phase but promote the growth of a larger Chinese-script α_C-$Al_{15}(Fe,Mn)_3Si_2$ phase (Fig. 1(d)). Further Mn addition eliminates the fine β-$Al_{4.5}FeSi$ phase but leads to the formation of coarse polyhedral α_C-$Al_{15}(Fe,Mn)_3Si_2$ primary crystals (Figs. 1(e) and 1(f)). On the other hand, severe Fe contamination triggers the development of enlarged β-$Al_{4.5}FeSi$ platelets (Fig. 1(g)) as primary crystals during the onset of solidification at high temperatures. In such a case, Mn introduction initially decreases the phase fraction of the coarse β-$Al_{4.5}FeSi$ platelets by promoting the formation of the Chinese-script α_C-$Al_{15}(Fe,Mn)_3Si_2$ phase (Fig. 1(h)). The increase in Mn content reduces both the phase fraction and size of the coarse β-$Al_{4.5}FeSi$ platelets by favoring the occurrence of the smaller and more globular polyhedral α_C-$Al_{15}(Fe,Mn)_3Si_2$ phase and suppressing the β-$Al_{4.5}FeSi$ phase to lower temperatures (Fig. 1(i)). Nevertheless, excessive Mn addition stabilizes the α_C-$Al_{15}(Fe,Mn)_3Si_2$ phase at elevated temperatures without further suppressing the formation temperature of β-$Al_{4.5}FeSi$. This results in the presence of coarse polyhedral α_C-$Al_{15}(Fe,Mn)_3Si_2$ particles without the benefit of refining the β-$Al_{4.5}FeSi$ phase (Fig. 1(j)).

The solidification conditions encountered in practical casting processes usually deviate from the thermodynamic equilibrium solution. The non-equilibrium solidification paths of moderately and severely contaminated alloys were determined using the Scheil-Gulliver model. Moreover, Scheil calculations were performed across the entire compositional range of Al-Si-Fe-Mn alloys to identify the critical Fe and Mn contents at varying Si concentration values. However, Scheil calculations often fail to predict non-equilibrium Fe-IMC phases, as elucidated in the introduction section. To address this limitation, a new approach was proposed in this work that leverages the simplicity of the Scheil-Gulliver non-equilibrium solidification model. The temperature and composition inputs derived from Scheil calculations under the condition of undercooled Fe-IMC phases were integrated with nucleation-related kinetic parameters such as the precipitation driving force and the interfacial energy. This integration enables circumventing the lack of a nucleation model within the Scheil solidification model and predicting the potential non-equilibrium microstructure formation

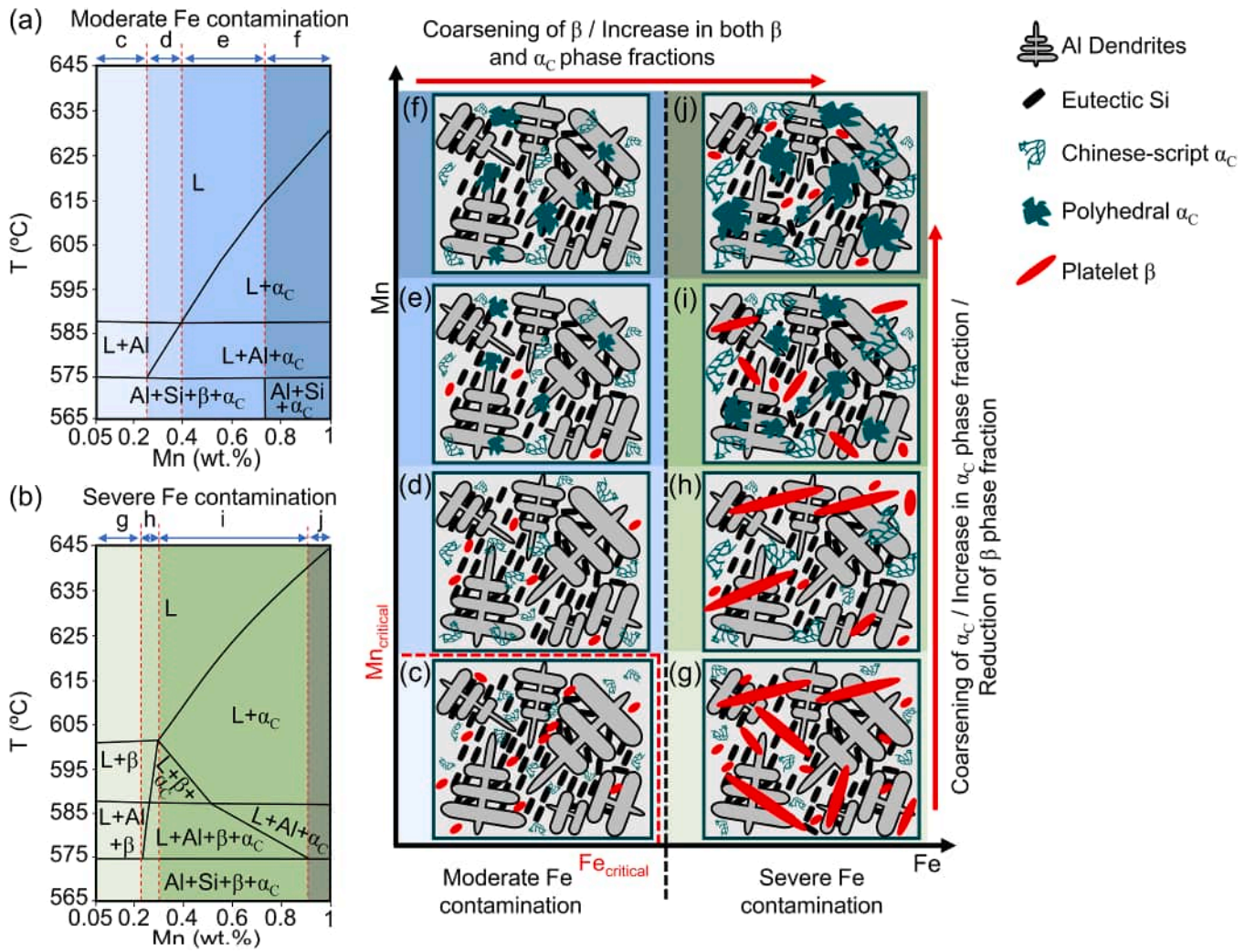

Fig. 1. Exemplary as-cast microstructure formation in Al-Si alloys under the assumption of equilibrium solidification conditions. (a,b) Simplified isopleths of the quaternary Al-Si-Fe-Mn system at 11wt.%Si-0.7wt.%Fe-Xwt.%Mn (moderate Fe contamination) and 11wt.%Si-1.4wt.%Fe-Xwt.%Mn (severe Fe contamination), respectively, indicating the corresponding composition range for each potential microstructure formation scenario. (c) Fe and Mn levels are below the proposed critical contents, restricting the occurrence of the platelet and Chinese-script Fe-IMC phases to the final eutectic reaction at the end of solidification. (d) A rise in Mn content reduces the platelet β-$Al_{4.5}FeSi$ phase fraction but raises the fraction and size of the pre-eutectic Chinese-script α_C-$Al_{15}(Fe,Mn)_3Si_2$. (e, f) Excessive Mn addition eventually eliminates the fine platelet β-$Al_{4.5}FeSi$ but forms coarser polyhedral α_C-$Al_{15}(Fe,Mn)_3Si_2$ phases. (g) When the Fe level increases, coarse platelet β-$Al_{4.5}FeSi$ forms earlier during solidification as pre-eutectic and primary phases. (h) Mn doping initially decreases the phase fraction of coarse platelet β-$Al_{4.5}FeSi$ by forming a pre-eutectic Chinese-script α_C-$Al_{15}(Fe,Mn)_3Si_2$ phase. (i) Increasing the Mn content reduces both the phase fraction and size of the coarse platelet β-$Al_{4.5}FeSi$ by promoting the primary polyhedral and pre-eutectic Chinese-script α_C-$Al_{15}(Fe,Mn)_3Si_2$ phases and suppressing the formation temperature of β-$Al_{4.5}FeSi$ phase. (j) Any additional Mn content stabilizes the primary polyhedral α_C-$Al_{15}(Fe,Mn)_3Si_2$ phase at higher temperatures without further suppression of the platelet β-$Al_{4.5}FeSi$ formation temperature.

scenarios. The detailed workflow of the modeling approach is illustrated in Fig. 2. More details on the model-building process can be found in supplementary material S1.

2.2. Thermodynamic modelling

Thermodynamic calculations based on the CALPHAD (CALculation of PHAse Diagrams) approach were performed using the Thermo-Calc software version 2022b [59]. The thermodynamic database used in this work is TCAL5.1. In this database, the ternary Al-Fe-Si system has been assessed over almost the entire composition and temperature range, while the quaternary Al-Fe-Mn-Si system has been assessed in the Al-rich corner [60].

The critical Fe and Mn contents were determined using Scheil–Gulliver simulations of non-equilibrium solidification paths [54,55]. Additionally, the ratio between the phase fraction of the script-like (α phases) to the overall phase fraction of the Fe-IMC phases was calculated. This ratio was referred to as the "corrected fraction (*f*)". A higher corrected fraction indicates a reduced presence of the detrimental platelet phases. When the corrected fraction reaches a value of one, it implies that the amount of added Mn is sufficient to correct all the Fe, i.e., converting all the undesired platelet-shaped phases into the Chinese-script phase. The corrected fractions at each critical Fe and Mn content were calculated under Scheil–Gulliver conditions.

The precipitation driving force of the Fe-IMC phases from the liquid phase was determined using the parallel tangent construction procedure [61,62]. For a binary system A-B, the change in molar Gibbs free energy that accompanies the formation of an arbitrary phase β from a liquid phase L can be calculated using the formula below:

$$\Delta G^{M} = \left(\mu^{M}_{A,\beta} X^{M}_{A,\beta} + \mu^{M}_{B,\beta} X^{M}_{B,\beta}\right) - \left(\mu_{A,L} X^{M}_{A,\beta} + \mu_{B,L} X^{M}_{B,\beta}\right) \quad (2)$$

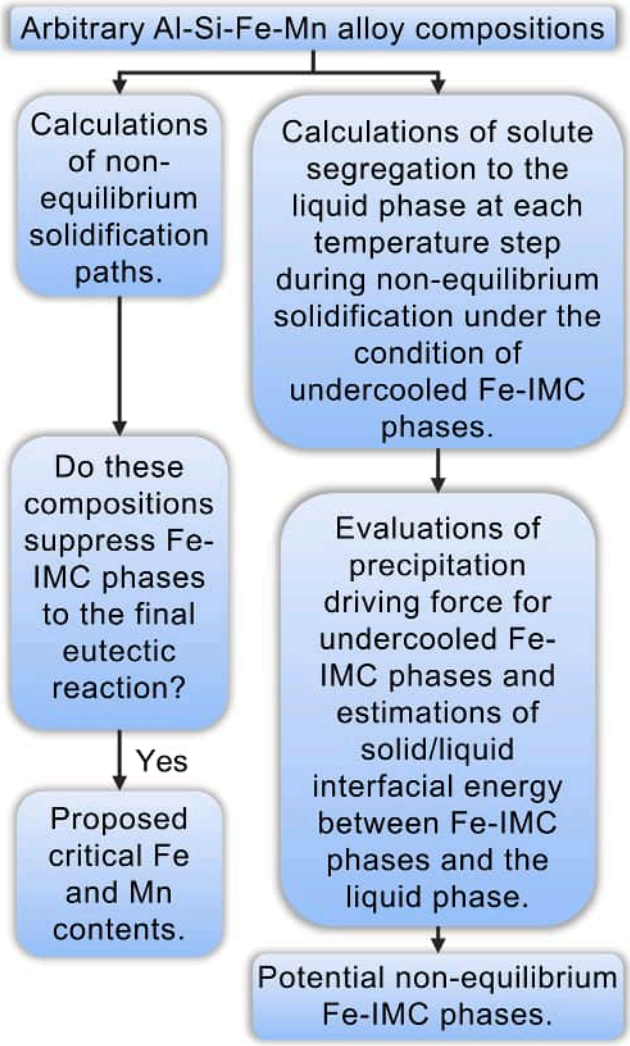

Fig. 2. Detailed workflow of the techniques applied in this study to predict the formation of non-equilibrium Fe-IMC phases.

where $X^{M}_{A,\beta}$ and $X^{M}_{B,\beta}$ are the mole fractions of elements A and B, respectively, in the β phase; $\mu^{M}_{A,\beta}$ and $\mu^{M}_{B,\beta}$ are the chemical potentials of A and B, respectively, in the β phase; $\mu_{A,L}$ and $\mu_{B,L}$ are the chemical potentials of A and B, respectively in the liquid phase L. The value $-\Delta G^{M}$ is the chemical driving force for precipitation. Two assumptions were employed: first, the increase in Gibbs free energy as a result of curvature induced pressure, i.e., the capillarity effect, was neglected; second, the nucleus composition aligns with the composition that maximizes the driving force (hence the superscript M). The driving force was calculated for the ten stable Fe-IMC phases in the ternary Al-Fe-Si system. Additionally, the calculations were extended to the metastable α-AlFeSi. This was performed by adjusting the α_C-$Al_{15}(Fe,Mn)_3Si_2$ phase constitution in the TCAL5.1 thermodynamic database. The α_C-$Al_{15}(Fe,Mn)_3Si_2$ phase model is described using four sublattices: $(Al)_{15}(Fe,Mn)_4(Si)_1(Al,Si)_2$. In our approach, Mn was rejected from the $(Fe,Mn)_4$ sublattice, hence obtaining a description for the metastable α_C-AlFeSi phase with a cubic crystal structure similar to that of α_C-$Al_{15}(Fe,Mn)_3Si_2$ phase. The driving force was calculated during the solidification at varying temperatures and liquid compositions. The enrichment of the liquid with solutes at any temperature during solidification was assumed to follow the Scheil–Gulliver conditions explained earlier. Furthermore, the precipitation of the Fe-IMC phases from the supersaturated liquid during solidification was suspended.

2.3. Estimation of interfacial energy

The solid–liquid interfacial energy between the Fe-IMC phases and the liquid phase was estimated using the Generalized Nearest-Neighbor Broken-Bond method [63], which models a coherent planar sharp interface. In this study, a short-range order in the liquid phase region surrounding the precipitate was assumed, hence, the atoms in the liquid adjacent to the precipitate adopt the same lattice configuration as the precipitating Fe-IMC phase. The interfacial energy $\gamma_{S/L}$ was calculated using the formula:

$$\gamma_{S/L} = \frac{n_s \cdot Z_{s,eff}}{N_A \cdot Z_{L,eff}} \cdot \Delta E_{sol} \tag{3}$$

where n_s is the number of atoms per unit interface area, $Z_{s,eff}$ is the effective number of broken bonds across the interface, N_A is Avogadro's number, $Z_{L,eff}$ is the effective coordination number, and ΔE_{sol} is the change in solution enthalpy associated with the precipitation of one mole of precipitate [63,64]. The structural factors n_s, $Z_{s,eff}$, and $Z_{L,eff}$ depend on the crystal structure and interface orientation. In this work, these structural factors were calculated for the crystal plane with the fewest number of broken nearest-neighbor bonds, thereby minimizing interfacial energy. This particular plane corresponds to the one with the highest planar packing density, which refers to the specific plane of atoms in the unit cell with the highest fraction of filled space. Thus, the planar packing densities for the symmetrically unique crystallographic planes in the α_C, α_H, γ, δ, and β Fe-IMC phases were first determined (available in supplementary material S2). The crystallographic information of these Fe-IMC phases including the atomic positions and unit cell parameters were obtained from literature [26,65–68]. To calculate $Z_{s,eff}$ and $Z_{L,eff}$ a weighting scheme was implemented that assigns lower weights to atoms located farther from a central atom, while nearer atoms receive higher weights [69–71]. This approach accounts for the reduced binding energies of atoms positioned at greater distances from a central atom. The following weighting scheme was used:

$$Z_{eff} = \sum_i w_i \tag{4}$$

$$w_i = \exp\left(1 - \left(\frac{l_i}{l_{avg}}\right)^6\right) \tag{5}$$

$$l_{avg} = \frac{\sum_i l_i \exp\left(1 - \left(\frac{l_i}{l_{min}}\right)^6\right)}{\sum_i \exp\left(1 - \left(\frac{l_i}{l_{min}}\right)^6\right)} \tag{6}$$

where w_i is the bond weight, l_i is the bond distance to the i^{th} atom, l_{avg} is the weighted average bond length, and l_{min} is the minimum bond distance to the first nearest-neighbor atom. Since the bonds distances differ between different Fe-IMC phases, the $Z_{s,eff}$ and $Z_{L,eff}$ were calculated for all neighboring atoms up to a distance of five angstroms (Å). Any bond distance greater than five angstroms (Å) was excluded due to negligibly low weight. Lastly, ΔE_{sol} was calculated assuming stoichiometric Fe-IMC phases using the following formula:

$$\frac{\partial H_{sol}}{\partial x_{pre}} = H_{pre} - H_{mat} + \sum_i \frac{\partial H_{mat}}{\partial x_{i,mat}} \cdot \left(x_{i,mat} - x_{i,pre}\right) \tag{7}$$

where H_{sol} is the molar solution enthalpy, x_{pre} is the mole fraction of the precipitate phase, H_{pre} is the precipitate molar enthalpy, H_{mat} is the matrix molar enthalpy, $x_{i,mat}$ is the mole fraction of a component *i* in the matrix, and $x_{i,pre}$ is the mole fraction of a component *i* in the precipitate. The derivation of this formula is provided in Appendix B. ΔE_{sol} was calculated for a broad temperature range that covers the solidification range of the alloys. The change in liquid composition caused by solute

segregation at each temperature step was assumed to follow the Scheil assumptions mentioned earlier. Finally, the nucleation energy barrier was estimated using the driving force and specific interfacial energy values in accordance with classical nucleation theory (CNT) [72], assuming homogeneous nucleation of Fe-IMC phases within the liquid phase. Based on the observed morphologies of Fe-IMC phases, two nucleus shapes were considered, a sphere and an oblate spheroid. The latter was assumed specifically for the platelet Fe-IMC phases. The formulae for calculating the spheroid volume and surface area are provided in Appendix B.

2.4. Sample preparation

Three alloy groups were prepared to investigate a range of Fe-contamination levels. Alloy group one corresponds to moderately-contaminated alloys, while alloy groups two and three represent severely-contaminated alloys. The compositions of these alloys were chosen based on the results of the modeling step to serve as model compositions to validate the calculations. The alloys were synthesized using pure Al (99.8%), Fe (99.9%), Mn (99.8%), and Si (99.9%) in a vacuum induction furnace under an argon (Ar) atmosphere. First, the crucible and other casting components were dried using hot air. Next, a near vacuum condition of five mbar was applied for two hours, followed by the injection of high-purity argon at a pressure of 800 mbar. The pure materials were then melted at 1000 °C and mixed for 10 min. Finally, the molten material was poured into the molds at a temperature of 1000 °C. The compositions of the alloys (in wt.%) are presented in Table 2. The compositions were measured by standard-less quantitative energy dispersive X-ray spectroscopy (EDS). 10 different EDS measurements, each covering an area of 1.5 mm^2, were conducted. Additionally, the Mn content in the Mn-free alloys was determined using inductively coupled plasma optical emission spectroscopy (ICP-OES), revealing a trace amount of 0.002 %.

In order to compare the predicted and actual microstructures that form under non-equilibrium solidification conditions, it is essential to reproduce these non-equilibrium scenarios in casting experiments. This was achieved using two mold design types with distinct dimensions and heat transfer characteristics, resulting in varying cooling rates and a wide range of non-equilibrium solidification conditions. Alloy group one was cast into a cylindrical Magnesium Oxide (MgO) mold with a copper base and iron frame. The mold had an outer diameter of 90 mm, an inner diameter of 40 mm, and a height of 200 mm. On the other hand, alloy groups two and three were prepared in a 20 mm thick cylindrical copper mold with a diameter of 25 mm and a height of 200 mm. Disk-shaped metallography samples were sectioned at the same positions from the top and the bottom parts of the ingots to ensure the same cooling conditions (Fig. 3). Additionally, the tensile samples were cut from the axial cross sections of the cylindrical cast ingots, extending from near the outer wall to the center along the radial direction, as shown in Fig. 3.

Table 2
Nominal and actual compositions of the alloys measured by EDS.

Alloy group No.	Composition (wt.%)			
	Si	Fe	Mn	Al
1	7 (8.7 ± 0.3)	0.8 (0.73 ± 0.03)	–	Bal.
	11 (12.6 ± 0.1)	0.8 (0.76 ± 0.03)	–	Bal.
2	7 (7.7 ± 0.1)	2.0 (1.92 ± 0.07)	–	Bal.
	11 (11.6 ± 0.4)	2.0 (1.93 ± 0.05)	–	Bal.
3	7 (7.6 ± 0.3)	2.0 (1.87 ± 0.13)	0.5 (0.46 ± 0.04)	Bal.
	11 (11.7 ± 0.2)	2.0 (1.91 ± 0.09)	0.5 (0.45 ± 0.02)	Bal.

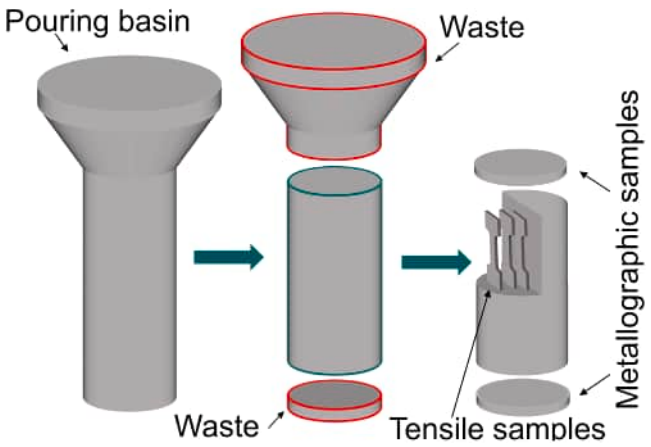

Fig. 3. Casting and preparation of metallographic and tensile specimens.

Because the cooling rate is higher near the walls and lower toward the center, these samples capture the variations in mechanical properties resulting from the difference in cooling rates and associated changes in microstructure. A total of at least nine tensile samples per alloy were prepared. Standard metallographic sample preparation techniques were followed to prepare the sample for microstructure analysis by Scanning Electron Microscopy (SEM), Energy Dispersive Spectroscopy (EDS), and Electron Backscatter Diffraction (EBSD). The specimens were ground using SiC papers, then polished with diamond polishing suspension, and finally chemo-mechanically polished with colloidal silica. Samples for EBSD mapping were further polished with colloidal silica in a vibratory polisher to remove topographical artifacts.

2.5. Microstructure and property characterization

Microstructural observations were conducted in a ZEISS Sigma field emission scanning electron microscope (FE-SEM). Both secondary electron images (SE-images) and backscattered electron images (BSE-images) were obtained from the microstructures. Chemical composition information was obtained through EDS at an acceleration voltage of 20 KV, an electron beam current of 6.6 nA, and a working distance of 10 mm. In addition, EBSD was used to determine the crystal structure of the Fe-IMC phases. The specimens were tilted to 70 °, and the working distance was 16 mm. The acceleration voltage and electron beam current were 15 KV and 5.4 nA, respectively. The mechanical properties were investigated by uniaxial tensile testing. Tensile specimens with a total length of 54 mm, a gauge length of 30 mm, a gauge width of 5 mm, and a thickness of 2 mm were used. The tensile tests were performed at room temperature and an initial strain rate of 0.001 s^{-1}.

The obtained microstructure micrographs were analysed using the ImageJ/Fiji image processing package [73]. This enabled determining the area fraction of the Fe-IMC phases and consequently the corrected fraction, as well as the size (Feret diameter) and aspect ratio of these phases. Additionally, it allowed the calculation of the secondary dendrite arm spacing (SDAS) of the Al dendrites using the linear intercept method. For the moderately-contaminated alloys, image analysis was conducted on a minimum of 30 randomly selected fields of view at a magnification of 250x, covering a total investigated area of at least four mm^2. In the case of severely-contaminated alloys, at least eight fields of view at 50x were randomly chosen for image analysis, corresponding to a minimum area of around 38 mm^2. During image processing, the discrimination between Fe-IMC phases based on morphology was facilitated using various shape descriptors such as roundness and circularity [74]. This is due to the lack of contrast between different Fe-IMC phases. Image analysis was also applied to determine the orientation of the coarse platelets in the severely-contaminated alloys. This was performed by measuring the angle between the major axis of a

platelet particle and the tensile axis. Orientations of 0° and 90° represent a platelet particle aligned parallel and perpendicular to the tensile direction, respectively. The angle distributions of the coarse platelets in two distinct tensile samples before fracture and at the fracture surface were compared to derive statistically meaningful results.

3. Results

3.1. Moderately-contaminated alloys (0.8wt.% Fe)

3.1.1. Thermodynamic calculations

The graph in Fig. 4(a) depicts the critical levels of Fe and Mn. The y-axis denotes the critical Mn content, while the x-axis represents the Si concentration. Moreover, the color bar and contour lines indicate the critical Fe content that prevents the pre-eutectic formation of the Fe-IMC phases. At a fixed Si concentration, any increase in the critical Mn content decreases the critical Fe content, and vice versa. For instance, at 7% Si and 0.2% Mn, the critical Fe content is 0.37%, resulting in an overall critical Fe + Mn content of 0.57%. When the Si content remains at 7% but the Mn content increases to 0.3%, the critical Fe content drops to approximately 0.14%, leading to an overall critical Fe + Mn content of 0.44%. The overall critical Fe + Mn content rises with Si concentration, peaking at approximately 1.1% (0.77% Fe + 0.31% Mn) at the eutectic point, around 12.67% Si. Subsequently, there is a negligible decrease in the overall critical Fe + Mn content within the hypereutectic region. Fig. 4(b) illustrates the corrected fractions calculated for each critical Mn concentration value and corresponding critical Fe contents. The corrected fraction rises with the increase in the Mn content. However, at the same Mn concentration, the corrected fraction near the eutectic composition with the higher critical Fe content is less than that in the far-from-eutectic region with the lower critical Fe content. The corrected fraction at the peak value of the overall critical Fe + Mn content is 0.47.

In Figs. 5(a)-5(c), the precipitation driving force of the stable and metastable ternary Fe-IMC phases is presented. Fig. 5(a) illustrates the driving force during solidification of a composition aligned with the ternary Al-Fe-Si eutectic point (12.67% Si and 0.89% Fe). At elevated temperatures, the driving force is negative. The driving force gradually increases as the temperature decreases and then experiences a sharp rise at approximately the Al + Si eutectic reaction temperature, i.e., at 575 °C. During solidification, the β phase consistently exhibits the highest driving force to form at any given temperature, followed by δ, γ, α_H, and α_C. The driving force of these phases undergoes a strong transition from negative to positive with small undercooling below the eutectic temperature. In contrast, the remaining phases maintain a negative driving force throughout the process. Figs. 5(b) and 5(c) display the driving force of the β, δ, and α_C phases during the solidification of the moderately-contaminated far-from-eutectic Al-7wt.%Si-0.8wt.%Fe and near-eutectic Al-11wt.%Si-0.8wt.%Fe alloys. The liquidus temperatures of these alloys are 615 °C and 588 °C, respectively. At their respective liquidus temperatures, both alloys exhibit a negative precipitation driving force. As the temperature decreases during solidification, the driving force gradually increases. In the Al-7wt.%Si-0.8wt.%Fe alloy, the driving force for β and δ turns positive at temperatures of 593 °C and 585 °C, respectively. However, α_C exhibits a positive driving force with small undercooling below 575 °C. Conversely, in the Al-11wt.%Si-0.8wt.%Fe alloy, the driving force for β becomes positive at approximately 577 °C. On the other hand, the driving force for the δ and α_C phases undergoes a negative to positive transition with slight undercooling under 575 °C.

3.1.2. Microstructure characteristics

The microstructures of the Al-7wt.%Si-0.8wt.%Fe and Al-11wt.%Si-0.8wt.%Fe alloys are depicted in Figs. 6(a) and 6(b), respectively. Both alloys exhibit four distinct phases: Al dendrites, dark gray platelet eutectic Si, white platelet Fe-IMC, and white Chinese-script Fe-IMC. The mean SDAS values of the Al-11wt.%Si-0.8wt.%Fe and Al-7wt.%Si-0.8wt.%Fe alloys close to the mold wall are 26.2 ± 5.9 μm and 25 ± 5.3 μm, respectively. In both alloys, the Chinese-script phase and a fine platelet phase are embedded between the eutectic Si in the interdendritic region. However, in the Al-7wt.%Si-0.8wt.%Fe alloy, larger platelets can be observed growing parallel to the adjacent Al secondary dendrite arms. Figs. 6(c) and 6(d) present the dendritic grain sizes of Al in the Al-7wt.%Si-0.8 wt.%Fe and Al-11wt.%Si-0.8wt.%Fe alloys, respectively. The near-eutectic alloy (Al-11wt.%Si-0.8wt.%Fe) exhibits a larger mean grain diameter compared to the far-from-eutectic alloy (Al-7wt.%Si-0.8 wt.% Fe). The Al-7wt.%Si-0.8wt.%Fe alloy has a mean grain diameter of 550 ± 401 μm and a maximum grain diameter of 1946 μm. In contrast, the Al-11wt.%Si-0.8wt.%Fe alloy displays a mean grain diameter of 962 ± 484 μm and a maximum grain diameter of 1963 μm. The thickness of the interdendritic region between the Al dendrites is larger in the near-eutectic alloy compared to the far-from-eutectic alloy. The size and aspect ratio of the eutectic Si phase varies between the two alloys. The near-eutectic alloy generally forms larger platelet-shaped Si

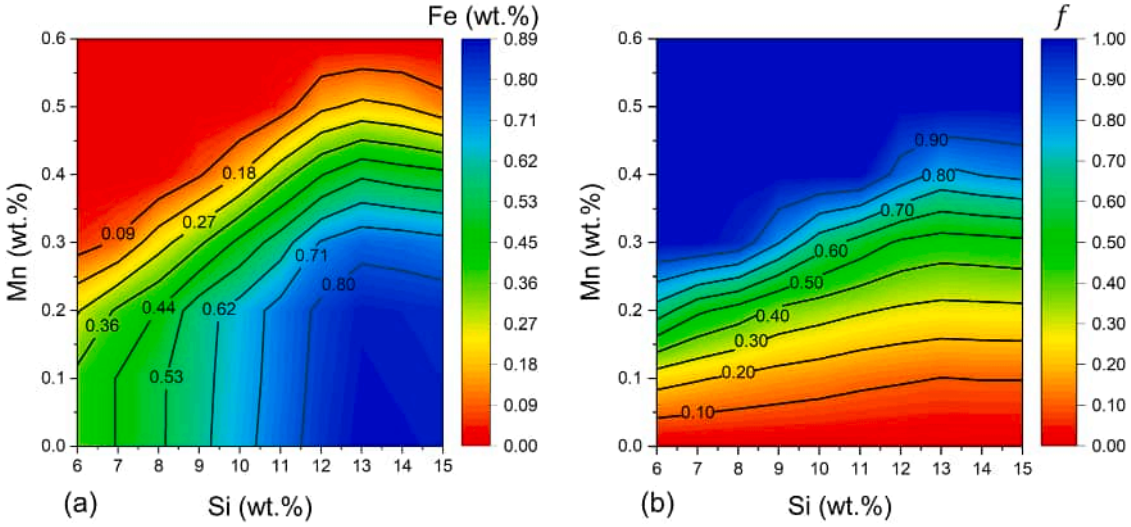

Fig. 4. Thermodynamic modelling results of the hypothesized Fe and Mn tolerances. (a) The color bar and contour lines denote the critical Fe content at each critical Mn content and Si amount. (b) The corrected fraction at each critical Fe and Mn contents. The parameter *f* is the relative phase fraction of the least harmful Chinese-script phase to the total fraction of the Fe-IMC phases.

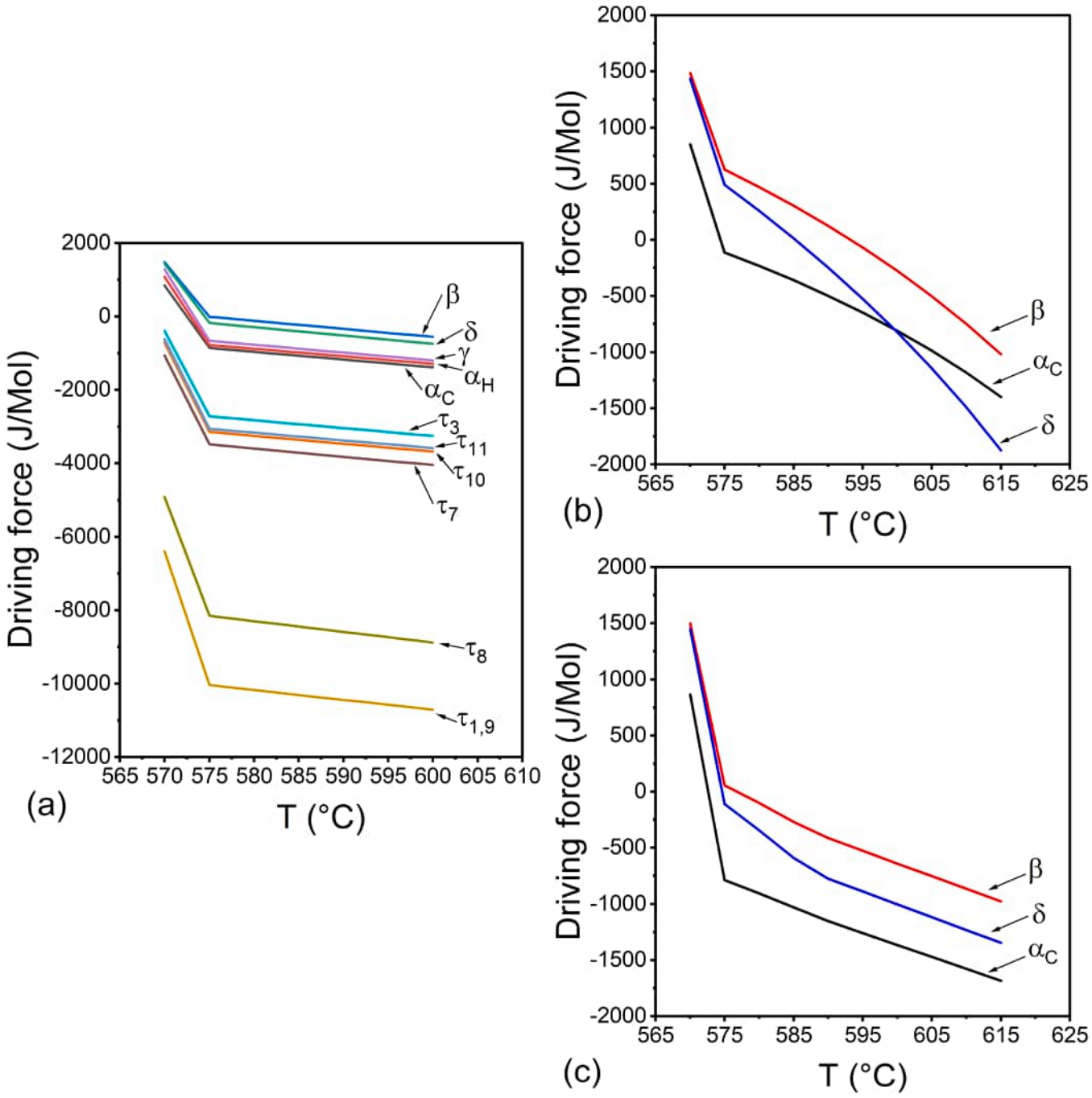

Fig. 5. Chemical driving force for the precipitation of the stable and metastable ternary Fe-IMC phases (Table 1) during the solidification of (a) a composition corresponding to the ternary Al-Fe-Si eutectic point, (b) far-from-eutectic Al-7wt.%Si-0.8wt.%Fe alloy, and (c) near-eutectic Al-11wt.%Si-0.8wt.%Fe alloy.

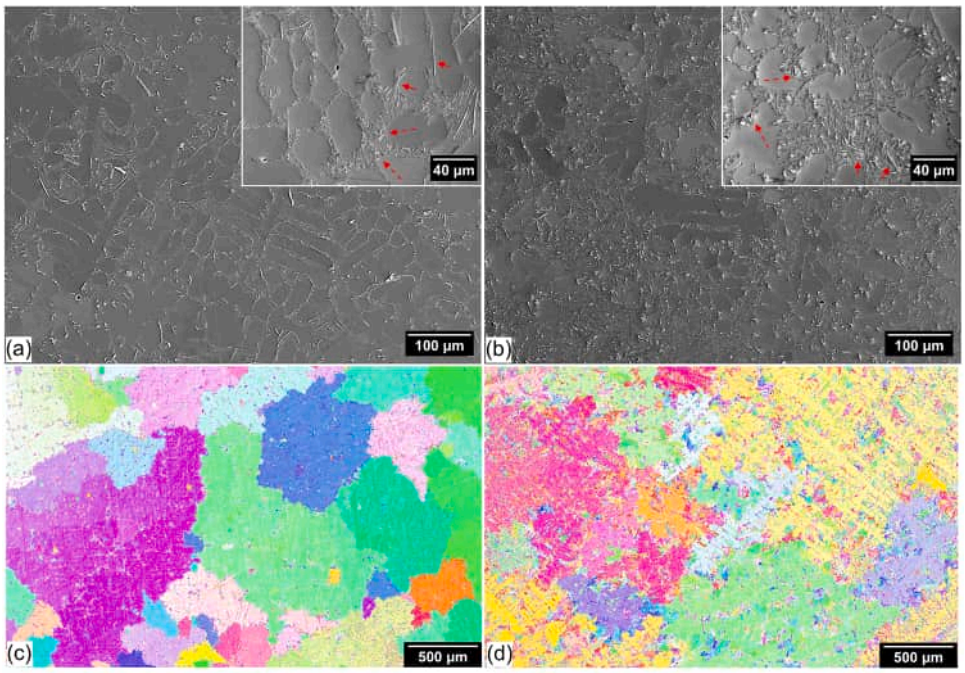

Fig. 6. Microstructures of the moderately-contaminated alloys (a) Al-7wt.%Si-0.8wt.%Fe and (b) Al-11wt.%Si-0.8wt.%Fe. The solid and dashed arrows indicate a platelet phase and a Chinese-script phase, respectively. (c,d) EBSD informed grain maps of the Al dendrites in Al-7wt.%Si-0.8wt.%Fe and Al-11wt.%Si-0.8wt.%Fe alloys, respectively.

with higher aspect ratios compared to the far-from-eutectic alloy. In the Al-7wt.%Si-0.8wt.%Fe alloy, which has a lower Si concentration, the eutectic Si has a mean grain size of 2.8 ± 2.5 μm and a maximum size of 26.8 μm. Additionally, the mean aspect ratio of eutectic Si in this alloy is 2.6 ± 1.7, with a maximum aspect ratio of 23.2. Conversely, the Al-11wt.%Si-0 .8wt.%Fe alloy, containing a higher Si concentration, exhibits eutectic Si with a mean grain size of 3.3 ± 2.7 μm and a maximum size of 35 μm. The mean aspect ratio of eutectic Si in this near-eutectic alloy is 3.5 ± 2.5, and the maximum aspect ratio reaches 30.3.

Fig. 7 presents EBSD phase and inverse pole figure (IPF) maps obtained from the interdendritic region of the Al-11wt.%Si-0.8 wt.%Fe alloy. The Chinese-script phase consists of two distinct Fe-IMC phases, α_C and γ, while the platelet phase corresponds to the δ phase. Representative raw and indexed EBSD patterns for the Chinese-script α_C phase are shown in Figs. 7(c1) and 7(c2), respectively. The pattern is indexed according to the cubic α-AlMnSi phase with the space group $Pm\bar{3}$ (No. 200) and lattice parameter a = 12.64 Å [65]. Four reflections {530}, {235}, {013}, and {600} were considered in the indexing process. This indexing gave a confidence index of 0.46 and a fit of 0.27°. Similarly, Figs. 7(d1) and 7(d2) display the raw and indexed EBSD patterns for the Chinese-script γ phase. The pattern is indexed according to the trigonal γ-Al_3FeSi with the space group $R\bar{3}$ (No. 148) and cell parameters a = 10.199 Å, b = 10.199 Å, c = 19.532 Å, α=90° β=90 °, γ=120 ° [21]. 12 reflectors $\{12\bar{3}8\}$, $\{13\bar{4}\bar{5}\}$, $\{1\bar{5}40\}$, $\{1\bar{3}27\}$, $\{2\bar{5}3\bar{2}\}$, $\{04\bar{4}1\}$, $\{04\bar{4}5\}$, $\{01\bar{1}\bar{1}0\}$, $\{13\bar{4}4\}$, $\{12\bar{3}7\}$, $\{12\bar{3}\bar{4}\}$, and $\{11\bar{2}3\}$ were used for indexing. This yielded a confidence index of 0.89 and a fit of 0.26°. The phase fraction of the Chinese-script α_C phase is more than five times higher than the phase fraction of the Chinese-script γ phase. Figs. 7(e1)-7(e3) illustrate the Chinese-script α_C phase growing in contact with neighboring eutectic Si phase flakes. Table 3 shows the measured chemical compositions of the observed Fe-IMC phases.

The impact of Si content on the formation of Fe-IMC phases in the moderately-contaminated alloys is presented in Table 4. The quantitative microstructural analysis reveals a notable difference in the area fraction of the Chinese-script and platelet phases between the alloys. The Al-11wt.%Si-0.8wt.%Fe alloy exhibits a substantially higher area fraction of the Chinese-script phase and a lower area fraction of the platelet phase compared to the Al-7wt.%Si-0.8wt.%Fe alloy. These area fraction values correspond to a corrected fraction of 0.41 ± 0.09 and 0.82 ± 0.08 for the Al-7wt.%Si-0.8wt.%Fe and Al-11wt.%Si-0.8wt.%Fe alloys, respectively. On the other hand, the mean size of the platelet phase is similar between the alloys, but the maximum size in the Al-7wt.%Si-0.8wt.%Fe alloy is considerably larger than in the Al-11wt.%Si-0.8wt.% Fe alloy. The aspect ratio of the platelet phase follows the same trend. In contrast, the mean and maximum sizes and aspect ratios of the Chinese-script phase remain comparable in both alloys. The platelet phase displays higher mean and maximum sizes and aspect ratios than the Chinese-script phase.

3.1.3. *Mechanical properties and fracture behavior*

Fig. 8(a) illustrates the tensile properties of the moderately-contaminated alloys. The near-eutectic Al-11wt.%Si-0.8wt.%Fe alloy has a mean yield strength (YS) of 87 ± 3 MPa, a mean ultimate tensile strength (UTS) of 121 ± 27 MPa, and a mean elongation at fracture (E_f) of 3.0 ± 1.2%. In contrast, the far-from-eutectic Al-7wt.%Si-0.8wt.%Fe alloy has a mean YS of 78 ± 5 MPa, a mean UTS of 100 ± 19 MPa, and a mean E_f of 2.2 ± 0.9%. Figs. 8(b)-8(d) depict the cracked Fe-IMC and Si phases near the fracture surface. The white arrow indicates the stretching direction during tensile testing. In Fig. 8(b), a long and wide transgranular crack develops within a platelet particle alongside multiple shorter transgranular cracks in a neighboring platelet particle. A similar pattern is observed for the Chinese script particles in Fig. 8(d).

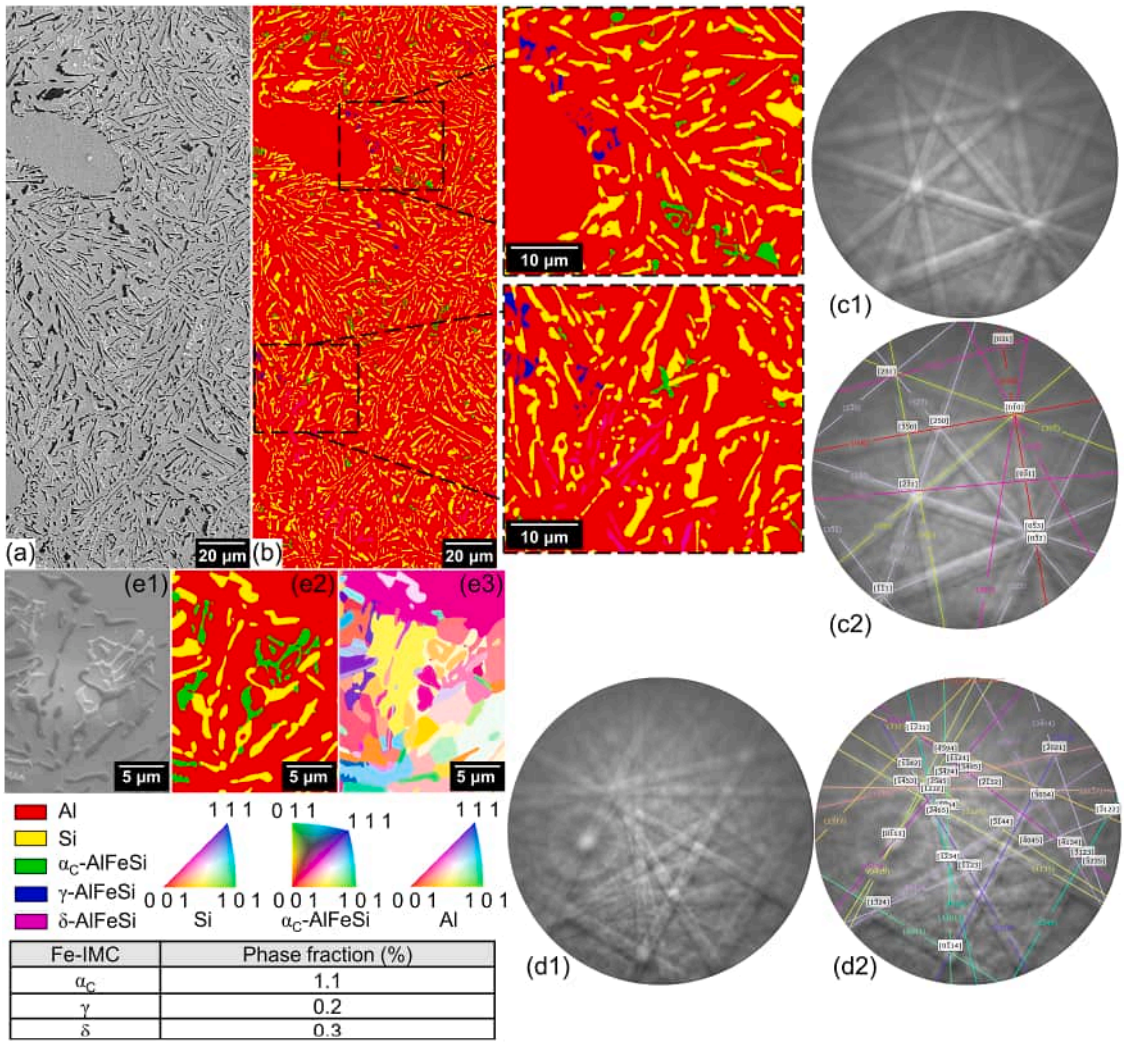

Fe-IMC	Phase fraction (%)
α_C	1.1
γ	0.2
δ	0.3

Fig. 7. The identified Fe-IMC phases inside the interdendritic region of the Al-11wt.%Si-0.8wt.%Fe alloy. (a, b) The microstructure of the interdendritic region, and the corresponding EBSD phase map indicating the formation of α_C, γ, and δ Fe-IMC phases. (c1, c2) Raw EBSD pattern acquired from the Chinese-script phase, and the indexed pattern according to the cubic α-AlMnSi with the space group $Pm\bar{3}$ (No. 200). (d1, d2) Raw EBSD pattern acquired from the Chinese-script phase, and the indexed pattern according to the trigonal γ-Al_3FeSi with the space group $R\bar{3}$ (No. 148). (e1-e3) A phase map and an inverse pole figure (IPF) map display small protuberances pertaining to the α_C Chinese-script phase growing from adjacent eutectic Si phase substrates.

Table 3
Chemical compositions of the Fe-IMC phases in the moderately-contaminated alloys.

Alloy	Morphology	Composition (at.%)			Calculated formula
		Al	Si	Fe	
Al-7wt.%Si-0.8wt.%Fe	Chinese-script	82.7 ± 2.5	8.9 ± 1.8	8.4 ± 1.5	$Al_{9.85}FeSi_{1.06}$
	Platelet	76.8 ± 4.3	17 ± 3.1	6.2 ± 1.5	$Al_{12.39}FeSi_{2.74}$
Al-11wt.%Si-0.8wt.%Fe	Chinese-script (α_C)	83.4 ± 2.6	8.4 ± 2.2	8.2 ± 1.2	$Al_{10.17}FeSi_{1.02}$
	Chinese-script (γ)	72.5 ± 2.9	13.2 ± 1.2	14.3 ± 2.4	$Al_{5.72}Fe_{1.08}Si$
	Platelet	74.6 ± 2.9	19.1 ± 2.9	6.3 ± 0.8	$Al_{11.84}FeSi_{3.03}$

Table 4
The area fraction, size (Feret diameter), and aspect ratio statistics of the Fe-IMC phases in the moderately-contaminated alloys. The maximum values are written in brackets.

Alloy	Area fraction (%)		Size (μm)		Aspect ratio	
	Chinese-script	Platelet	Chinese-script	Platelet	Chinese-script	Platelet
Al-7wt.%Si-0.8wt.%Fe	1.14 ± 0.3	1.65 ± 0.29	1.5 ± 1.6 (31.5)	6.4 ± 5.5 (49.5)	1.5 ± 0.6 (3.0)	5.9 ± 3.7 (36.4)
Al-11wt.%Si-0.8wt.%Fe	2.27 ± 0.44	0.54 ± 0.3	2.1 ± 1.9 (35.3)	6.2 ± 3.7 (31.2)	1.7 ± 0.6 (3.5)	5.1 ± 2.6 (31.3)

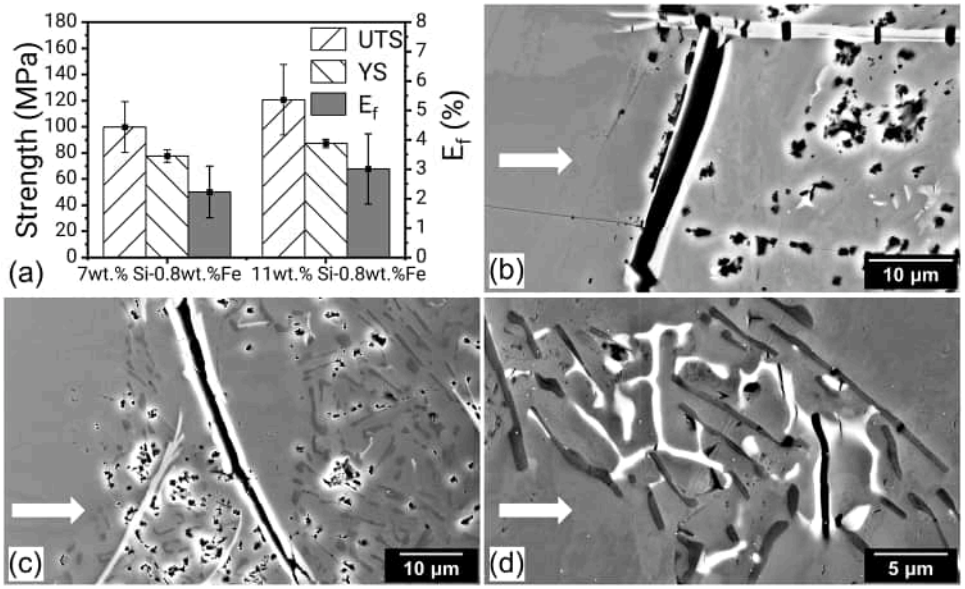

Fig. 8. (a) Ultimate tensile strength (UTS), yield strength (YS), and elongation at fracture (E_f) of the moderately-contaminated alloys. (b)-(d) Side views of the fracture surface showing transgranular cracks growing through the Fe-IMC phases in the Al-7wt.%Si-0.8wt.%Fe alloy (b and c) and the Al-11wt.%Si-0.8wt.%Fe alloy (d). The white arrows indicate the tensile direction.

However, the cracks in the platelet phase appear larger than those in the Chinese-script phase. In addition to transgranular cracks in the Si and Fe-IMC phases, microvoids can be seen nucleating inside the interdendritic region.

3.2. Severely-contaminated alloys (2.0wt.% Fe)

3.2.1. Thermodynamic calculations

Table 5 presents the predicted solidification paths for the severely-contaminated near-eutectic Al-11wt.%Si-2wt.%Fe and far-from-eutectic Al-7wt.%Si-2wt.%Fe alloys. In the Al-7wt.%Si-2wt.%Fe alloy, solidification starts with the primary α_H phase formation at 622 °C. With progressive cooling to 613 °C, Al dendrites emerge alongside the α_H phase through a binary eutectic reaction. At 612 °C, the α_H phase decomposes into the β phase through a quasi-peritectic reaction. As the temperature decreases, the β phase remains the only thermodynamically stable Fe-IMC phase. The solidification concludes with a ternary eutectic reaction at 575 °C. In contrast, the solidification path of the Al-11wt.%Si-2wt.%Fe alloy commences with the formation of the primary β phase instead of the primary α_H phase. The β phase maintains thermodynamic stability throughout the entire solidification process. At 588 °C, Al dendrites and binary eutectic β form. The solidification process ends with the ternary eutectic reaction.

Figs. 9(a)-9(c) illustrate the precipitation driving force of the Fe-IMC phases during the solidification of the alloys Al-11wt.%Si-2wt.%Fe and Al-7wt.%Si-2wt.%Fe, respectively. In both alloys, the Fe-IMC phases that demonstrate a positive driving force at elevated temperatures during the early stages of solidification include the β, δ, γ, α_H, and α_C phases. However, the evolution of the driving force differs between the two alloys. For instance, in the Al-7wt.%Si-2wt.%Fe alloy (Fig. 9(a)), the α_H phase exhibits the highest driving force at the start of solidification. However, as solidification progresses, the driving force of β surpasses that of α_H at an intermediate temperature, approximately 593 °C. Conversely, the β phase consistently maintains the highest driving force in the Al-11wt.%Si-2wt.%Fe alloy (Fig. 9(b)). The contrasting evolution of the β phase driving force between the Al-7wt.%Si-2wt.%Fe and Al-11wt.%Si-2wt.%Fe alloys is depicted in Fig. 9(c). At the beginning of solidification, the driving force for β in the Al-7wt.%Si-2wt.%Fe alloy is

Table 5
Predicted solidification paths based on Scheil-Gulliver model.

Al-7wt.%Si-2wt.%Fe		Al-11wt.%Si-2wt.%Fe	
Reaction	Onset T (°C)	Reaction	Onset T (°C)
L→ L+ α_H-Al_8Fe_2Si	622	L→ L+ β-$Al_9Fe_2Si_2$	621
L→ L+ α_H-Al_8Fe_2Si + Al	613	L→ L+ β-$Al_9Fe_2Si_2$ + Al	588
L+ α_H-Al_8Fe_2Si → L+ β-$Al_9Fe_2Si_2$ + Al	612	L→ β-$Al_9Fe_2Si_2$ + Al + Si	575
L→ β-$Al_9Fe_2Si_2$ + Al + Si	575		

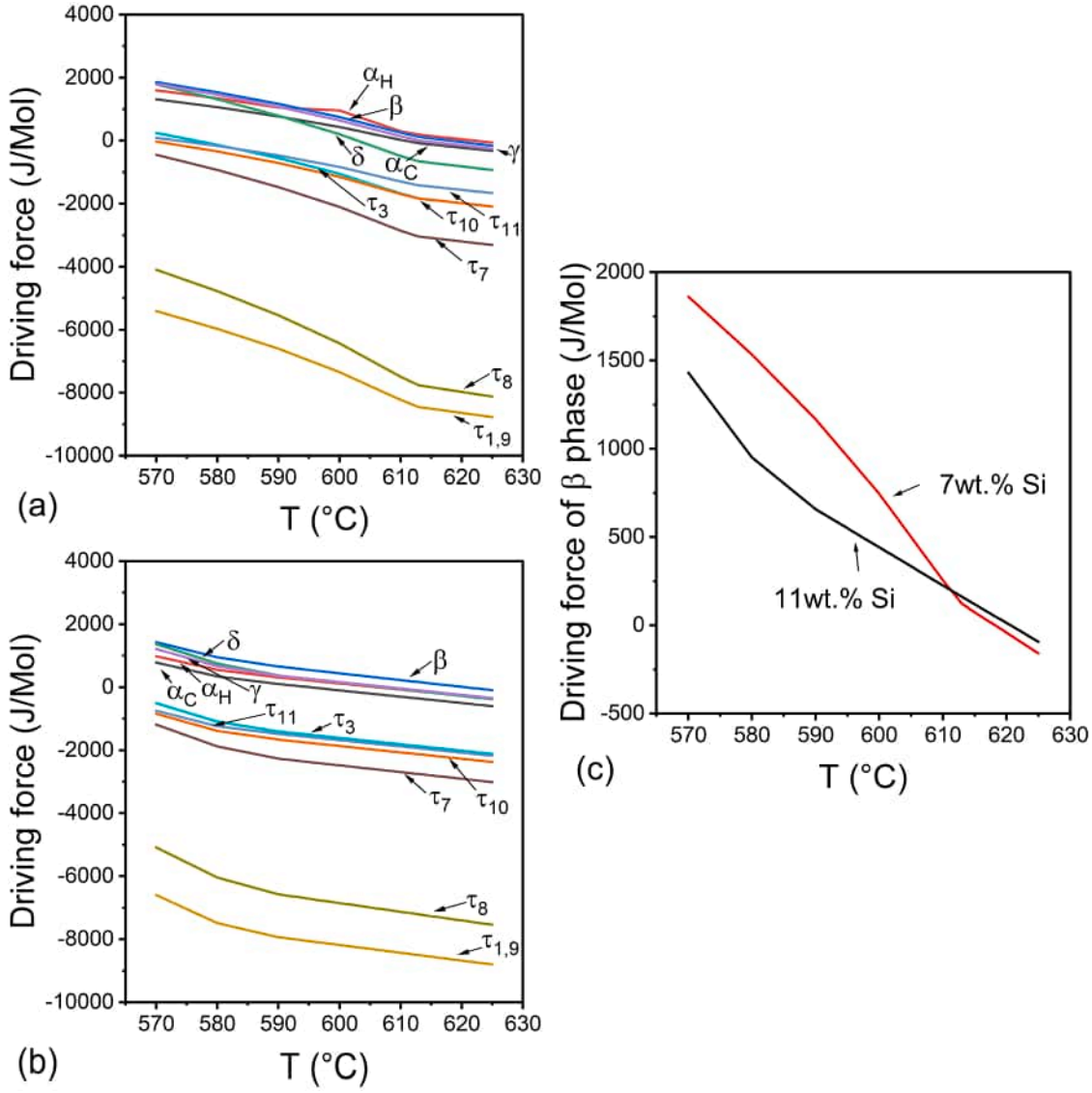

Fig. 9. Chemical driving force for the precipitation of the stable and metastable ternary Fe-IMC phases (Table 1) during the solidification of (a)Al-7wt.%Si-2wt.%Fe and (b)Al-11wt.%Si-2wt.%Fe. (c) Evolution of β phase driving force.

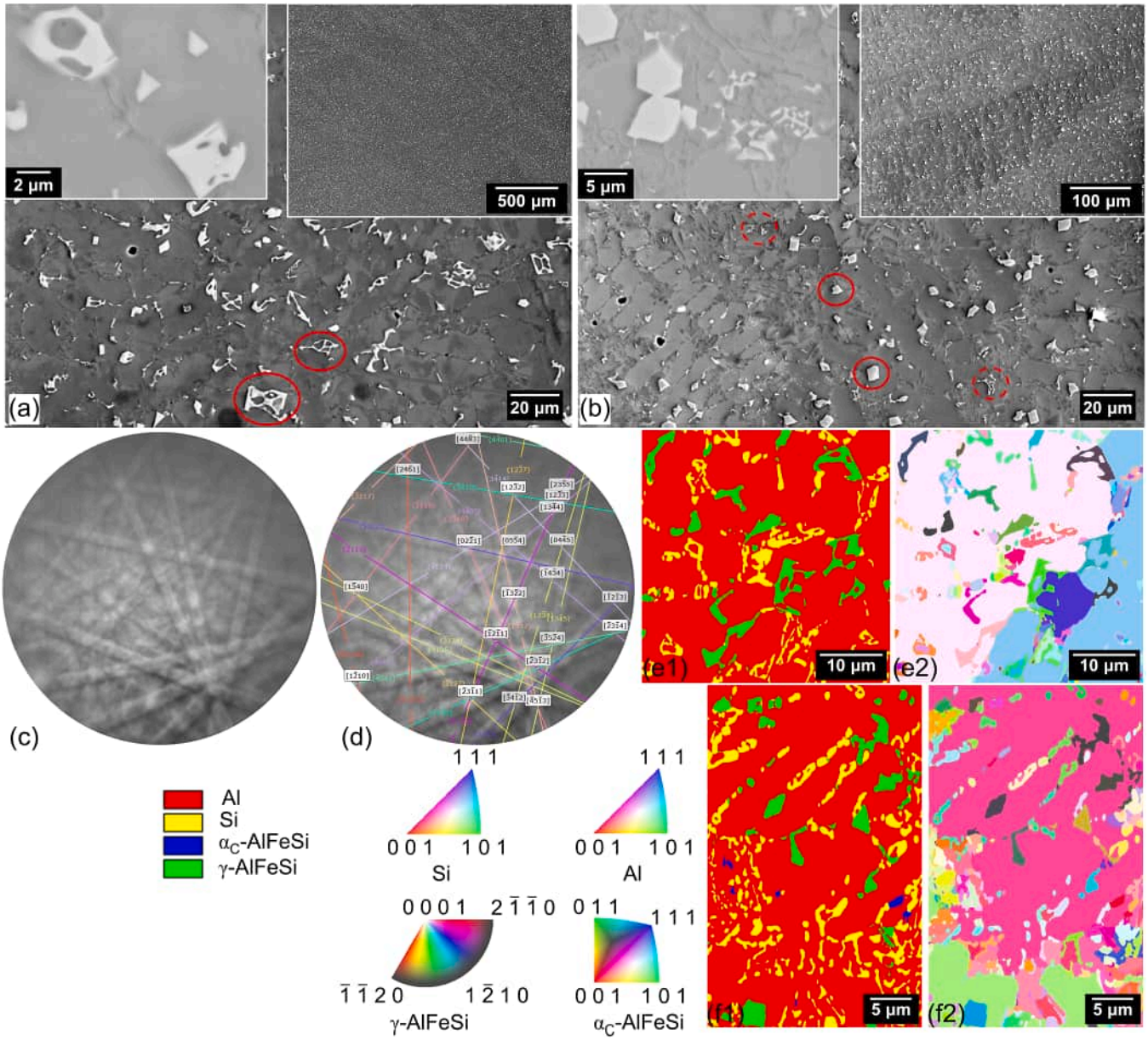

Fig. 10. The refined microstructures near the mold wall of the severely-contaminated alloys (a) Al-7wt.%Si-2wt.%Fe and (b) Al-11wt.%Si-2wt.%Fe. The fine polyhedral phase is marked with solid circles, while the Chinese-script phase is denoted by dashed circles. (c) Raw EBSD pattern obtained from the fine polyhedral phase. (d) The indexed pattern according to the trigonal γ-Al_3FeSi with the space group $R\bar{3}$ (No. 148). (e1, e2) Phase and IPF maps of the Al-7wt.%Si-2wt.%Fe alloy. (f1, f2) Phase and IPF maps of the Al-11wt.%Si-2wt.%Fe alloy. The γ-Al_3FeSi phase grows inside the Al dendrites in both alloys, while the metastable α_C-AlFeSi phase is only present in the interdendritic region of the Al-11wt.%Si-2wt.%Fe alloy.

slightly lower than in the Al-11wt.%Si-2wt.%Fe alloy. However, at approximately 613 °C, the driving force for the β phase in the Al-7wt.%Si-2wt.%Fe alloy experiences a rapid increase, surpassing that of the β phase in the Al-11wt.%Si-2wt.%Fe alloy.

3.2.2. Microstructure characteristics

The microstructures of the severely-contaminated alloys near the mold wall differ significantly from those near the center in terms of the types of Fe-IMC phases and the size of shrinkage porosity defects. Figs. 10(a) and 10(b) illustrate the microstructures near the mold wall. In both alloys, the region adjacent to the wall exhibits a refined microstructure that extends approximately six millimeters from the wall. The SDAS in the refined region measures 9.5 ± 1.4 μm and 7.7 ± 1.4 μm for the Al-7wt.%Si-2wt.%Fe and Al-11wt.%Si-2wt.%Fe alloys, respectively. This refined microstructure features a fine polyhedral Fe-IMC phase. The fine polyhedral phase in the Al-7wt.%Si-2wt.%Fe alloy has a branched structure, while in the Al-11wt.%Si-2wt.%Fe alloy, it appears mostly as a regular polyhedron. Moreover, the refined region in the Al-11wt.%Si-2wt.%Fe alloy contains a fine Chinese-script phase, whereas no such phase is evident in the Al-7wt.%Si-2wt.%Fe alloy. Figs. 10(c) and 10(d) demonstrate the raw and indexed EBSD patterns of the fine polyhedral phase. The pattern is indexed according to the trigonal γ-Al_3FeSi with the space group $R\bar{3}$ (No. 148) and cell parameters a = 10.199 Å, b = 10.199 Å, c = 19.532 Å, α=90° β=90 °, γ=120 ° [21]. 12 reflectors {12$\bar{3}$8}, {13$\bar{4}$5}, {1$\bar{5}$40}, {1$\bar{3}$27}, {2$\bar{5}$3$\bar{2}$}, {04$\bar{4}$1}, {04$\bar{4}$5}, {01$\bar{1}\bar{1}$0}, {13$\bar{4}$4}, {12$\bar{3}$7}, {12$\bar{3}$4}, and {11$\bar{2}\bar{3}$} were used for indexing. This yielded a confidence index of 0.87 and a fit of 0.24°. In Figs. 10(e1) and 10(e2), the phase and IPF maps of the Al-7wt.%Si-2wt.%Fe alloy are shown, while Figs. 10(f1) and 10(f2) display the corresponding maps for the Al-11wt.%Si-2wt.%Fe alloy. The fine polyhedral γ phase grows inside the Al dendrites in both alloys. In contrast, the Chinese-script metastable α_C-AlFeSi phase in the Al-11wt.%Si-2wt.%Fe alloy is located between the eutectic Si flakes in the interdendritic region.

Figs. 11(a) and 11(b) present the microstructures of the severely-contaminated alloys (2.0wt.% Fe) near the cast center. The SDAS measures 17.0 ± 3.9 μm for the Al-7wt.%Si-2wt.%Fe alloy and 14.2 ± 2.9 μm for the Al-11wt.%Si-2wt.%Fe alloy. The microstructures in the cast center are characterized by the formation of coarse and relatively finer

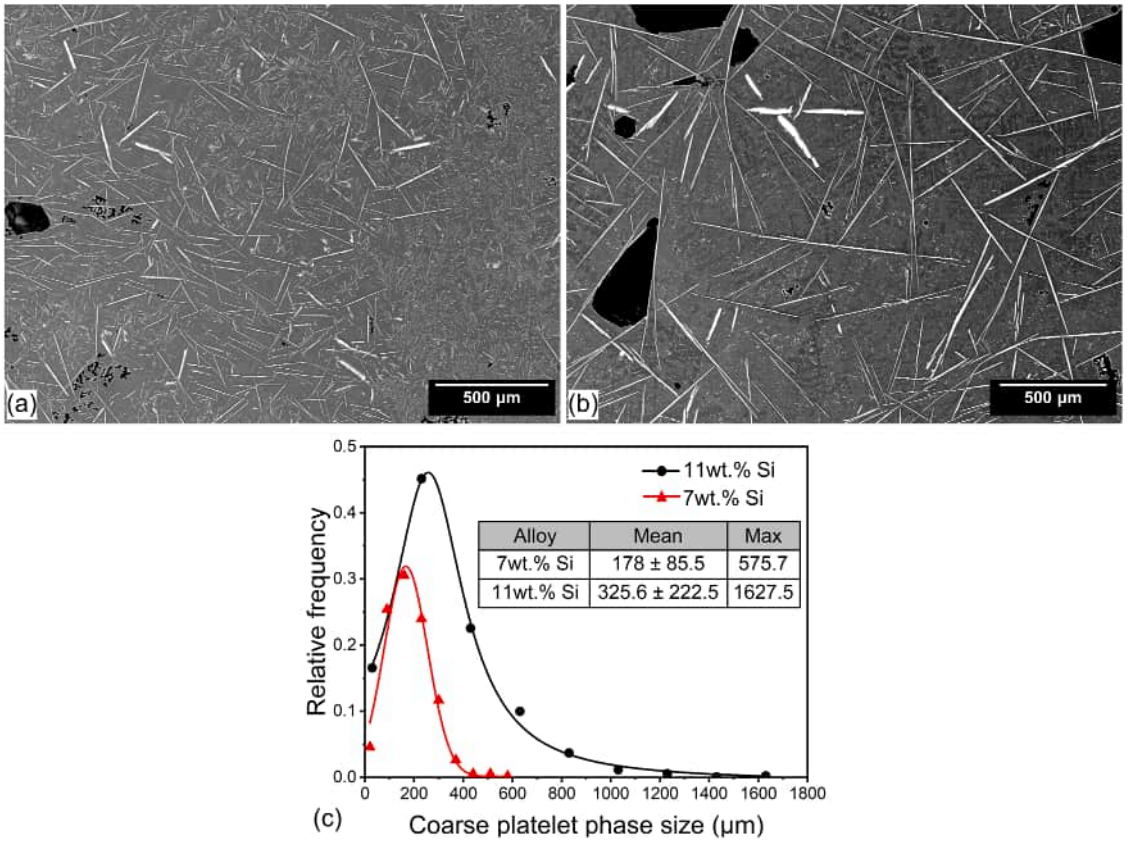

Fig. 11. Large area BSE images from the central region of the severely-contaminated alloys (a) Al-7wt.%Si-2wt.%Fe and (b) Al-11wt.%Si-2wt.%Fe. (c) Size distribution of the coarse platelet phase.

Table 6
Compositions of the observed phases in the severely-contaminated alloys.

Alloy	Morphology	Composition (at.%)			Calculated formula
		Al	Si	Fe	
Al-11wt.%Si-2wt.%Fe	Chinese-script	81.8 ± 1.6	10.4 ± 0.7	7.8 ± 1.3	$Al_{10.49}FeSi_{1.3}$
	Fine Polyhedral	67.8 ± 1.62	14.4 ± 0.5	17.8 ± 1.2	$Al_{4.7}Fe_{1.24}Si$
	Fine Platelet	73.1 ± 3.8	17.9 ± 1.4	9 ± 2.8	$Al_{8.12}FeSi_{1.99}$
	Coarse Platelet	67.9 ± 0.6	16.8 ± 0.4	15.2 ± 0.6	$Al_{4.46}$ $FeSi_{1.11}$
Al-7wt.%Si-2wt.%Fe	Fine Polyhedral	74.3 ± 5.5	12.2 ± 2.2	13.6 ± 3.9	$Al_{6.1}Fe_{1.11}Si$
	Fine Platelet	77.7 ± 4.8	14.5 ± 3.5	7.8 ± 1.8	$Al_{9.96}FeSi_{1.86}$
	Coarse Platelet	69.6 ± 2.3	15.1 ± 0.1	15.3 ± 0.1	$Al_{4.61}Fe_{1.01}Si$

platelet phases. The size distributions of the coarse platelet phase in the alloys are shown in Fig. 11(c). The mean and the maximum sizes of the coarse platelet phase in the Al-11wt.%Si-2wt.%Fe alloy are significantly higher than in the Al-7wt.%Si-2wt.%Fe alloy. In addition to the platelet phases, large pores with sizes that can reach up to one mm are present in the microstructures. These pores are predominantly located between the coarse platelet phase. The compositions of the observed phases in both alloys, including the refined region near the walls and the coarser regions near the center, are provided in Table 6. The compositions of the Chinese-script and fine platelet phases in the severely-contaminated alloys are close to those in the moderately-contaminated alloys.

3.2.3. Mechanical properties and fracture behavior

Fig. 12(a) depicts the tensile properties of the severely-contaminated alloys. The far-from-eutectic Al-7wt.%Si-2wt.%Fe alloy exhibits an average improvement of around 133.3% in E_f and 58% in UTS compared to the near-eutectic Al-11wt.%Si-2wt.%Fe alloy. The Al-11wt.%Si-2wt.%Fe alloy exhibits coincident values for the mean YS and UTS at 50 ± 9 MPa, and a mean E_f of 0.3 ± 0.2%. In contrast, the mean YS and UTS values of the Al-7wt.%Si-2wt.%Fe alloy are 72 ± 28 MPa and 79 ± 37 MPa, respectively, and the mean E_f is 0.7 ± 0.5%. Notably, the YS and UTS values of the Al-7wt.%Si-2wt.%Fe alloy show considerable variation, as indicated by the large standard deviation. Figs. 12(b) and 12(c) display the tensile fracture surfaces of the severely-contaminated alloys. The coarse platelets do not show any signs of decohesion from the matrix. Fig. 12(d) illustrates the orientation distribution of the coarse platelet phase with respect to the tensile loading axis. The orientation distribution appears uniform in the tensile samples before fracture (Fig. 12(d1)). However, at the fracture surface, a significant proportion of the coarse platelets are aligned at approximately 80–90° degrees with respect to the tensile direction (Fig. 12(d2)).

3.3. Impact of Mn on severely-contaminated alloys (2.0wt.% Fe-0.5wt.% Mn)

3.3.1. Thermodynamic calculations

Table 7 outlines the solidification paths for the Al-11wt.%Si-2wt.% Fe and Al-7wt.%Si-2wt.% Fe alloys after the addition of 0.5wt.% Mn. In both alloys, the solidification starts with the formation of the primary α_C-$Al_{15}(Fe,Mn)_3Si_4$ phase. However, significant discrepancies between their solidification paths emerge as solidification progresses. In the Al-7wt.%Si-2wt.%Fe-0.5wt.%Mn alloy, the Al dendrites become thermodynamically stable at 614 °C through a binary eutectic reaction with the α_C-$Al_{15}(Fe,Mn)_3Si_4$ phase. Conversely, in the Al-11wt.%Si-2wt.%Fe-0.5wt.%Mn alloy at 613 °C the β-$Al_9Fe_2Si_2$ phase becomes stable. In the Al-7wt.%Si-2wt.%Fe-0.5wt.%Mn alloy at 607 °C, the α_C-$Al_{15}(Fe,Mn)_3Si_4$ phase becomes unstable while the β-$Al_9Fe_2Si_2$ phase becomes stable. However, at around 581 °C, the α_C-$Al_{15}(Fe,Mn)_3Si_4$ phase regains stability and coexists with the β-$Al_9Fe_2Si_2$ and the Al dendrites. In contrast, this stable/unstable transition of α_C-$Al_{15}(Fe,Mn)_3Si_4$ is not

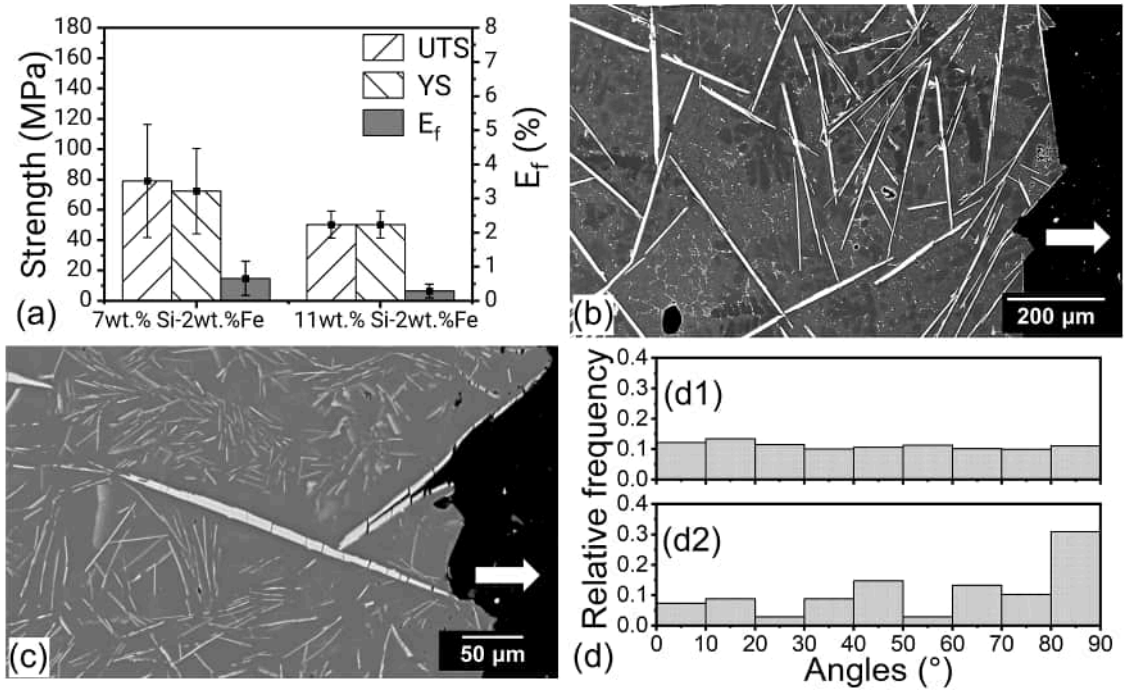

Fig. 12. (a) Ultimate tensile strength (UTS), yield strength (YS), and elongation at fracture (E_f) of the severely-contaminated alloys. (b, c) The fracture surfaces of Al-11wt.%Si-2wt.%Fe and Al-7wt.%Si-2wt.%Fe alloys, respectively. The white arrows indicate the tensile direction. (d) Orientation distribution of the coarse platelet phase: (d1) In the tensile specimens before fracture; (d2) At the fracture surface.

Table 7
Predicted solidification paths of the severely-contaminated alloys after Mn addition based on the Scheil-Gulliver solidification model.

Al-7wt.%Si-2wt.%Fe-0.5wt.%Mn		Al-11wt.%Si-2wt.%Fe-0.5wt.%Mn	
Reaction	Onset T (°C)	Reaction	Onset T (°C)
L→ L + α_C-$Al_{15}(Fe, Mn)_3Si_2$	642	L→ L + α_C-$Al_{15}(Fe, Mn)_3Si_2$	630
L→ L + α_C-$Al_{15}(Fe, Mn)_3Si_2$ + Al	614	L→ L + α_C-$Al_{15}(Fe, Mn)_3Si_2$ + β-$Al_9Fe_2Si_2$	613
L + α_C-$Al_{15}(Fe, Mn)_3Si_2$ → L + β-$Al_9Fe_2Si_2$ + Al	607	L→ L + α_C-$Al_{15}(Fe, Mn)_3Si_2$ + β-$Al_9Fe_2Si_2$ + Al	587
L→ L + α_C-$Al_{15}(Fe, Mn)_3Si_2$ + β-$Al_9Fe_2Si_2$ + Al	581	L→ α_C-$Al_{15}(Fe, Mn)_3Si_2$ + β-$Al_9Fe_2Si_2$ + Al + Si	575
L→ α_C-$Al_{15}(Fe, Mn)_3Si_2$ + β-$Al_9Fe_2Si_2$ + Al + Si	575		

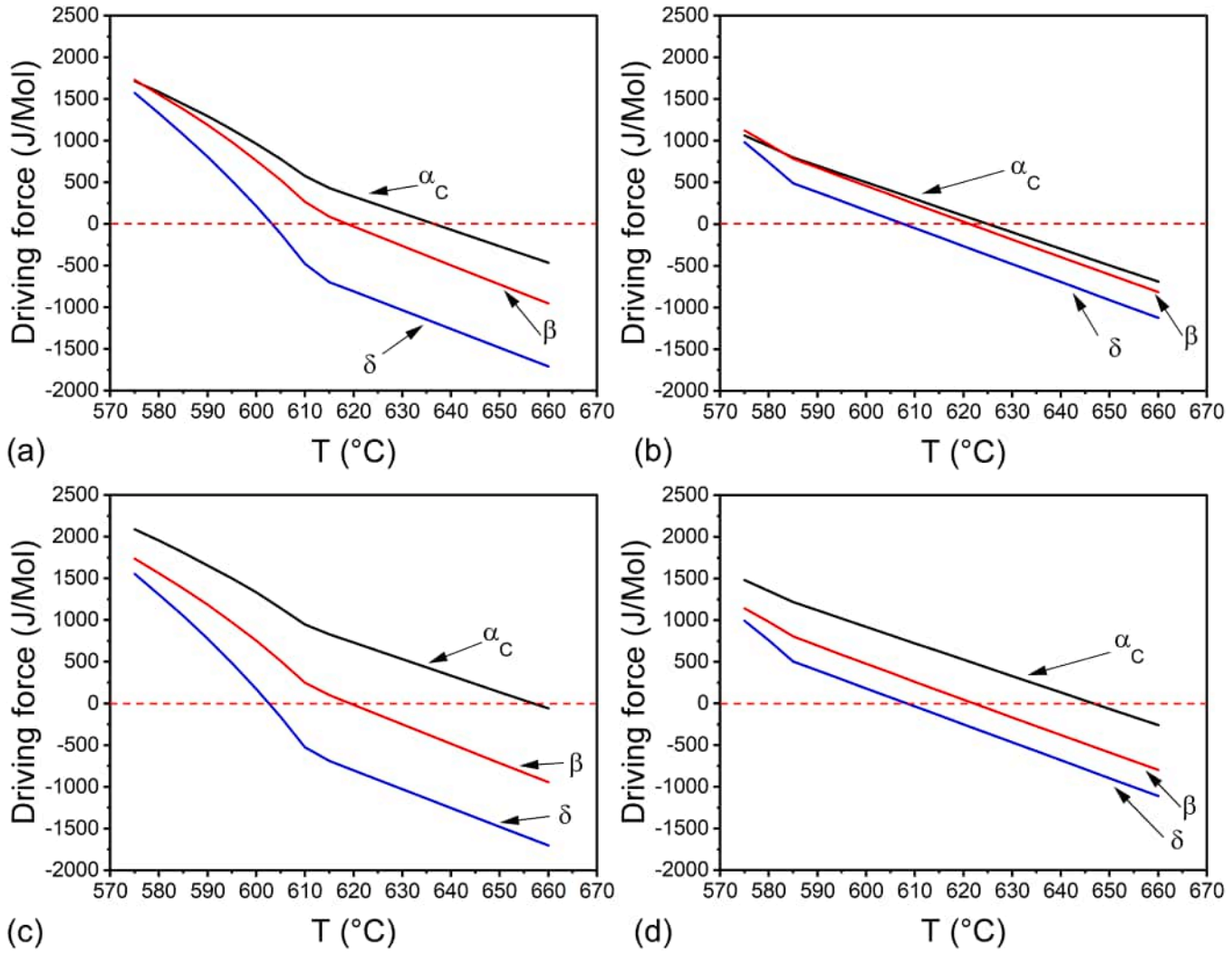

Fig. 13. Chemical driving force for the precipitation of the polyhedral/Chinese-script α_C-$Al_{15}(Fe, Mn)_3Si_2$ phase and the platelet β-$Al_9Fe_2Si_2$ and δ-Al_4FeSi_2 phases in the quaternary Al-Fe-Mn-Si system during the solidification of: (a) Al-7wt.%Si-2wt.%Fe-0.4wt.%Mn; (b) Al-11wt.%Si-2wt.%Fe-0.4wt.%Mn; (c) Al-7wt.%Si-2wt.%Fe-0.8wt.%Mn; (d) Al-1wt.%Si-2wt.%Fe-0.8wt.%Mn. The far-from-eutectic alloys (7wt.%Si) consistently maintain a wider temperature difference between the temperatures at which the α_C-$Al_{15}(Fe, Mn)_3Si_2$ and β phases show positive driving force compared to the near-eutectic alloys (11wt.%Si).

observed in the Al-11wt.%Si-2wt.%Fe-0.5wt.%Mn alloy, which instead sees the formation of Al dendrites at 587 °C. Ultimately, the solidification paths for both alloys end at a quaternary eutectic reaction at 575 °C.

Figs. 13(a)-13(d) depict the precipitation driving force of the α_C-$Al_{15}(Fe, Mn)_3Si_2$, β-$Al_9Fe_2Si_2$, and δ-Al_4FeSi_2 phases during the solidification of the severely-contaminated alloys (2.0wt.% Fe) upon the addition of 0.4wt.% and 0.8wt.% Mn. Across all alloys, the first Fe-IMC phase to exhibit a positive precipitation driving force is the α_C-$Al_{15}(Fe, Mn)_3Si_2$ phase, followed by the β phase and finally the δ phase. Despite this similarity, there are discrepancies in the driving force evolution between the near-eutectic (11wt.%Si) and the far-from-eutectic (7wt.% Si) alloys. In the Al-7wt.%Si-2wt.%Fe-0 .4wt.%Mn alloy (Fig. 13(a)), the addition of 0.4wt.%Mn results in a temperature difference of about 18 °C between the temperatures at which the α_C-$Al_{15}(Fe, Mn)_3Si_2$ and β phases exhibit a positive driving force. However, in the case of Al-11wt. %Si-2wt.%Fe-0.4wt.%Mn (Fig. 13(b)), this temperature difference diminishes to around 3 °C. With a two-fold increase in the Mn content to 0.8wt.%, the temperature difference rises in both alloys, reaching 38 °C for the Al-7wt.% Si-2wt.% Fe-0.8wt.% Mn alloy (Fig. 13(c)) and 24 °C for the Al-11wt.% Si-2wt.%Fe-0.8wt.%Mn alloy (Fig. 13(d)). The temperature difference in the far-from-eutectic alloy remains higher than in the near-eutectic alloy, regardless of the increase in Mn content.

3.3.2. *Microstructure characteristics*

Figs. 14(a)-14(c) present the microstructure near the wall of the severely-contaminated alloys (2.0wt.% Fe) after the addition of 0.5wt.% Mn. The SDAS near the wall measures 8.9 ± 1.6 μm for the Al-7wt.%Si-2wt.%Fe-0.5wt.%Mn alloy and 9.4 ± 1.4 μm for the Al-11wt.%Si-2wt.% Fe-0.5wt.%Mn alloy. The microstructure near the wall features the presence of fine polyhedral phases surrounding agglomerates of Chinese-script phases in the Al-7wt.%Si-2wt.%Fe-0.5wt.%Mn alloy (Fig. 14(a)), or agglomerates of relatively larger polyhedral phases in the Al-11wt.%Si-2wt.%Fe-0.5wt.%Mn alloy (Fig. 14(b)). The EBSD phase map in Fig. 14(c2) indicates that the fine polyhedral phase corresponds to the γ phase, while the agglomerates are identified as the α_C-$Al_{15}(Fe, Mn)_3Si_2$ phase (indexed as isomorphic to cubic α-AlMnSi). The size distribution of the Fe-IMC phases (without the agglomerates) in the refined region before and after Mn addition is shown in Fig. 14(d). The addition of Mn does not influence the size of the Fe-IMC phases.

The microstructure at the center of the severely-contaminated alloys (2.0wt.% Fe) after the addition of 0.5wt.% Mn and the resulting tensile properties are illustrated in Fig. 15. Figs. 15(a) and 15(b) display micrographs from the same longitudinal sections of the disk-shaped samples for the Al-11wt.%Si-2wt.%Fe-0.5wt.%Mn and Al-7wt.%Si-2wt.% Fe-0.5wt.%Mn alloys, respectively. Their respective SDAS values are

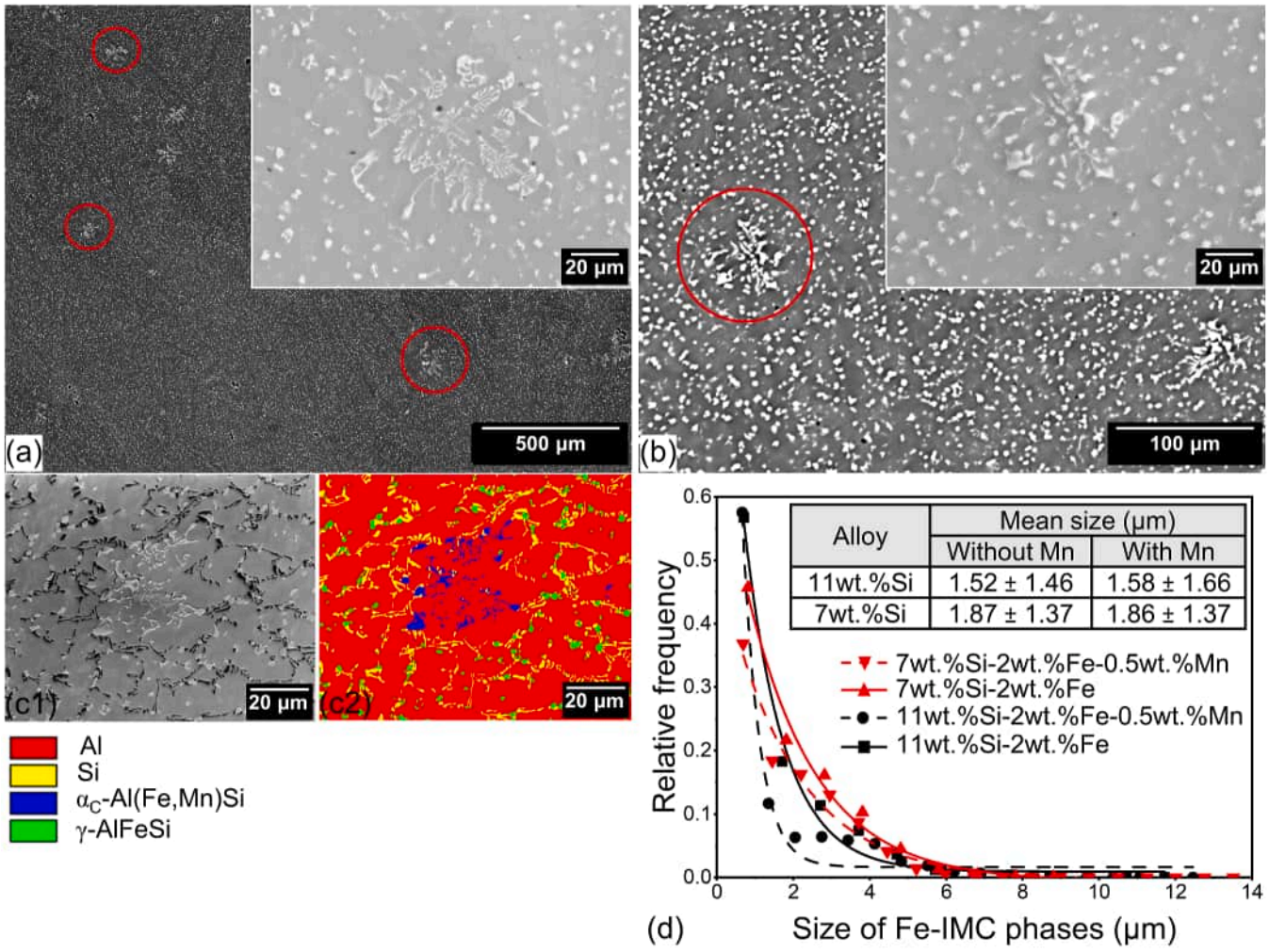

Fig. 14. The refined region near the wall of the severely-contaminated alloys (2wt.% Fe) after the addition of 0.5 wt.% Mn. (a) Fine polyhedral phases surrounding agglomerates of Chinese-script phases (indicated by red circles) in the Al-7wt.%Si-2wt.%Fe-0.5wt.%Mn alloy. (b) Fine polyhedral phases surrounding agglomerates of relatively larger polyhedral phases (indicated by red circles) in the Al-11wt.%Si-2wt.%Fe-0.5wt.%Mn alloy. (c1, c2) EBSD phase map of the Fe-IMC phases in the Al-7wt.%Si-2wt.%Fe-0.5wt.%Mn alloy. (d). The size distribution of the Fe-IMC phases (excluding the agglomerates) in the refined region near the wall before and after Mn addition.

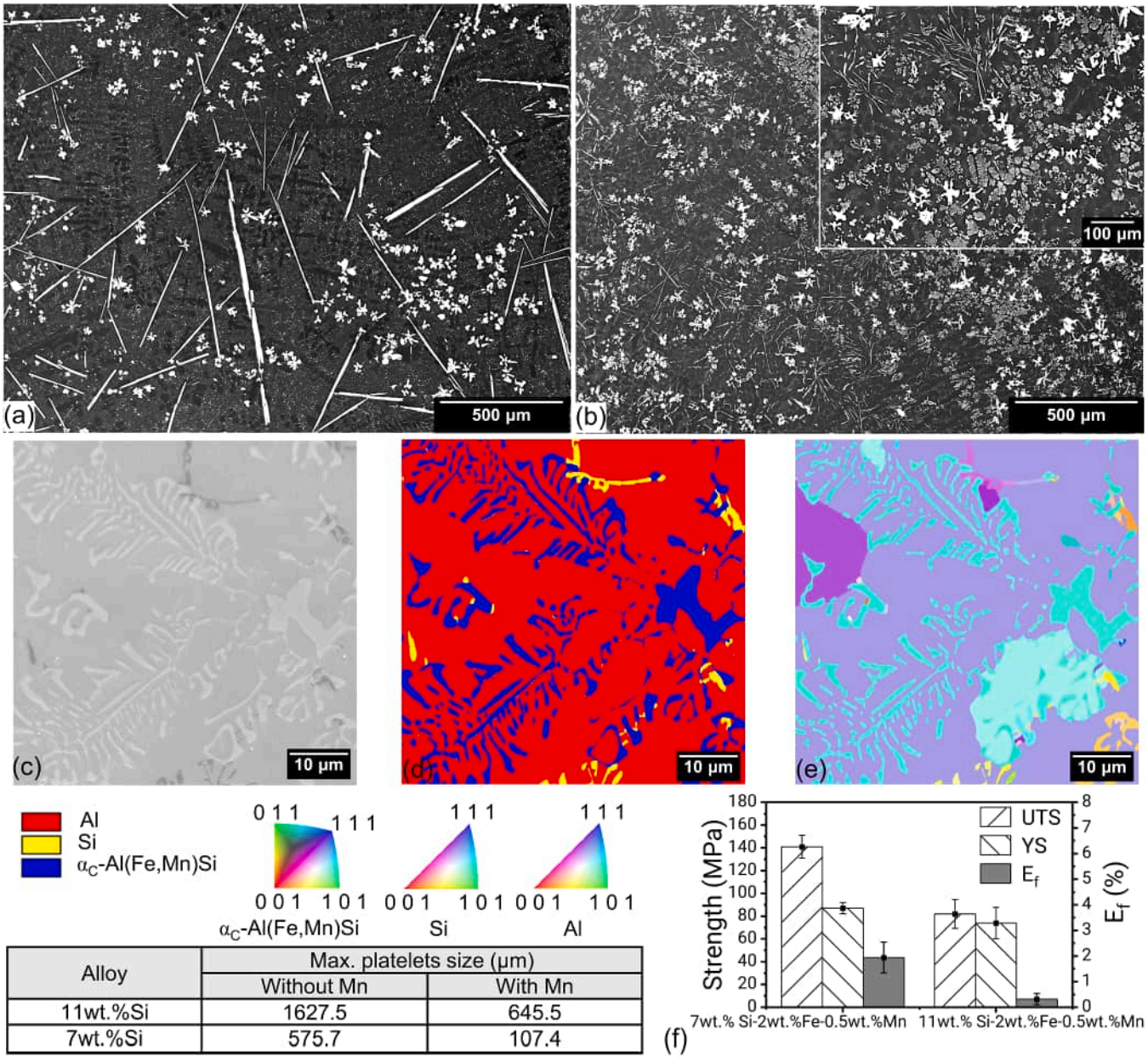

Alloy	Max. platelets size (µm)	
	Without Mn	With Mn
11wt.%Si	1627.5	645.5
7wt.%Si	575.7	107.4

Fig. 15. Microstructure images from the center of the severely-contaminated alloys after Mn addition: (a) Al-11wt.%Si-2wt.%Fe-0.5wt.%Mn alloy with coarse platelet and coarse polyhedral phases; (b) Al-7wt.%Si-2wt.%Fe-0.5wt.%Mn alloy showing coarse platelet and coarse polyhedral phases, as well as a highly-branched Chinese-script phase. (c) Magnified view of the coarse polyhedral and Chinese-script phases in the Al-7wt.%Si-2wt.%Fe-0.5wt.%Mn alloy. (d) EBSD phase map. (e) IPF map illustrating the crystallographic orientations of the coarse polyhedral and highly-branched Chinese-script phases. (f) Ultimate tensile strength (UTS), yield strength (YS), and elongation at fracture (E_f) of the severely-contaminated alloys after the addition of Mn.

Table 8
Compositions of the observed phases in the Mn-added severely-contaminated alloys.

Alloy	Morphology	Composition (at.%)				Calculated formula
		Al	Si	Fe	Mn	
11wt.%Si-2wt.%Fe-0.5wt.%Mn	Coarse platelets	66.2 ± 0.9	17.8 ± 2.8	13.3 ± 1.6	2.7 ± 0.9	$Al_{4.1}(Fe,Mn)Si_{1.1}$
	Fine platelets	72.9 ± 4.6	19.2 ± 3.5	6.7 ± 1.8	1.2 ± 0.2	$Al_{9.2}(Fe,Mn)Si_{2.4}$
	Fine polyhedral	65.4 ± 1.5	16.9 ± 0.9	14.5 ± 0.6	3.3 ± 0.2	$Al_{3.9}(Fe,Mn)_{1.05}Si$
	Coarse Polyhedral	72.3 ± 1	11.0 ± 1.1	12.6 ± 0.5	4.1 ± 0.4	$Al_{6.6}(Fe,Mn)_{1.52}Si$
7wt.%Si-2wt.%Fe-0.5wt.%Mn	Fine polyhedral	76.4 ± 3.9	11.9 ± 1.6	9.6 ± 1.9	2.1 ± 0.4	$Al_{6.53}(Fe,Mn)Si_{1.02}$
	Fine Platelet	76.6 ± 2.6	15.1 ± 2.0	7.1 ± 0.5	1.2 ± 0.1	$Al_{9.23}(Fe,Mn)Si_{1.82}$
	Chinese-script	81.1 ± 3.6	8.5 ± 1.7	8.1 ± 1.8	2.3 ± 0.6	$Al_{9.54}(Fe,Mn)_{1.22}Si$
	Coarse polyhedral	74.1 ± 0.7	8.8 ± 0.2	12.7 ± 0.6	4.4 ± 0.2	$Al_{8.41}(Fe,Mn)_{1.94}Si$

17.7 ± 2.5 μm and 17.5 ± 3.5 μm. Both alloys near the center feature coarse platelet and coarse polyhedral phases. Additionally, the Al-7wt.%Si-2wt.%Fe-0.5wt.%Mn alloy exhibits a highly-branched Chinese script phase resembling a fishbone (Fig. 15(c)). This phase grows with the same orientation as the neighboring polyhedral phase, as seen in the inverse pole figure map (Fig. 15(e)). The maximum size of the platelet phases in the Al-7wt.%Si-2wt.%Fe-0.5wt.%Mn and Al-11wt.%Si-2wt.%Fe-0.5wt.%Mn alloys measures 107.4 μm and 645.5 μm, respectively. The introduction of Mn to the severely-contaminated alloys significantly reduced the maximum size of the platelet phases compared to the Mn-free alloys (Fig. 11(c)). Fig. 14(f) depicts the tensile properties of the severely-contaminated alloys after the addition of 0.5wt.% Mn. The far-from-eutectic Al-7wt.%Si-2wt.%Fe-0.5wt.%Mn alloy exhibits mean YS and UTS values of 87 ± 5 MPa and 141 ± 10 MPa, respectively, and a mean E_f of 1.9 ± 0.6%. In contrast, the near-eutectic Al-11wt.%Si-2wt.%Fe-0.5wt.%Mn alloy exhibits a mean YS and UTS of 74 ± 14 MPa and 82 ± 13 MPa, respectively, and a mean E_f of 0.3 ± 0.2%. Table 8 presents the compositions of the observed phases, including those in the refined region near the wall.

3.4. Interfacial energy and nucleation barriers of Fe-IMC phases

Fig. 16 presents the crystal planes with the highest packing densities in the α_C, α_H, γ, δ, and β Fe-IMC phases (detailed packing densities of planes are provided in supplementary material S2). These planes correspond to the (301), (0001), (0001), (110), and (100) planes, respectively. The calculated structural factors n_s, $Z_{s,eff}$, and $Z_{L,eff}$ for these planes are shown in Table 9.

Figs. 17(a)–17(c) present the solid–liquid interfacial energy ($\gamma_{S/L}$) between the liquid phase and the Fe-IMC phases during the solidification of three alloys: a moderately-contaminated ternary eutectic alloy (Al–12.67wt.%Si–0.89wt.%Fe), a severely-contaminated far-from-eutectic alloy (Al–7wt.%Si–2wt.%Fe), and a severely-contaminated near-eutectic alloy (Al–11wt.%Si–2wt.%Fe), respectively. All three alloys exhibit the same general trend. The β phase consistently shows the lowest $\gamma_{S/L}$, followed by δ, γ, α_C, and finally α_H. Additionally, the $\gamma_{S/L}$ for each Fe-IMC phase increases as the temperature decreases. In the far-from-eutectic alloy (Fig. 17(b)), when the temperature is above 610 °C, the $\gamma_{S/L}$ of the δ phase is almost identical to that of the β phase.

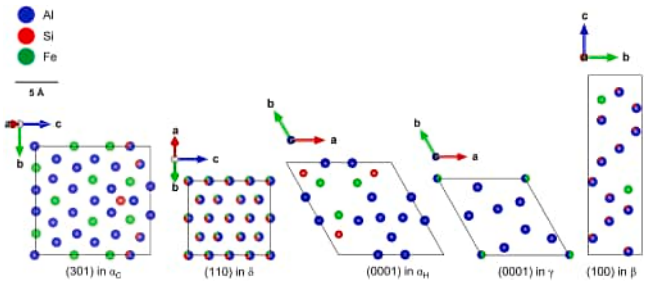

Fig. 16. Crystallographic planes with the highest planar packing densities in α_C, α_H, γ, δ, and β Fe-IMC phases.

Table 9
Calculated structural factors of the planes with the highest planar packing densities in α_C, α_H, γ, δ, and β Fe-IMC phases.

Fe-IMC phase	Crystal plane	n_s ($\times 10^{18}$ atoms/m^2)	$Z_{s,eff}$	$Z_{L,eff}$
α_C	(301)	19.58	74.33	318.37
α_H	(0001)	11.37	67.55	145.15
γ	(0001)	9.84	34.12	115.33
δ	(110)	20.74	41.76	392.95
β	(100)	8.31	34.57	198.00

Fig. 17(d) demonstrates the nucleation energy barrier and critical nucleus size for the γ phase in the severely-contaminated near-eutectic alloy (Al–11wt.%Si–2wt.%Fe) at 590 °C assuming a spherical nucleus shape. On the other hand, Figs. 17(e1) and 17(e2) illustrate the corresponding data for the β phase for the same alloy and temperature, assuming a spherical and a spheroidal atoms cluster shape (with an aspect ratio of 50), respectively. For spherical β clusters, the γ phase has a larger critical nucleus size and higher nucleation energy barrier compared to the β phase. However, when the β clusters are spheroidal, the β phase exhibits a much larger critical nucleus size and higher nucleation energy barrier than the γ phase. The critical nucleus size of γ is about 2.9 nm (Fig. 17(d)), while for β it is about 1 nm for spherical clusters and 25 nm for spheroidal clusters. The nucleation energy barrier of the γ phase is >10 times higher than that of the β phase in the case of spherical clusters (Fig. 17(d) vs. 17(e1)). Conversely, for spheroidal β clusters, the nucleation barrier for the β phase is >20 times greater than that of γ (note the different y-axis scale in Fig. 17(e2)). A similar comparison is shown in Figs. 17(f)–17(g2) for the α_C and β phases in the moderately-contaminated ternary eutectic alloy (Al–12.67wt.%Si–0.89wt.% Fe) at 570 °C. When β clusters assume a spherical shape, their critical nucleus size and nucleation energy barrier become lower than that of the α_C phase (Fig. 17(g1) vs. 17(f)). However, for spheroidal β clusters, the critical nucleus size and nucleation energy barrier of the β phase surpass that of the α_C. The critical nucleus size of α_C is about 2.2 nm (Fig. 17(f)), whereas the critical nucleus size of β phase is about 0.4 nm for spherical clusters and 11 nm for spheroidal clusters (Figs. 17(g1) and 17(g2)). The nucleation energy barrier of the α_C phase is >70 times higher than that of the β phase for spherical clusters (Fig. 17(f) vs. 17(g1)). In contrast, the nucleation barrier for the β phase is about four times higher than that of α_C when β phase clusters assume a spheroidal nucleus shape (note the different y-axis scale in Fig. 17(g2)).

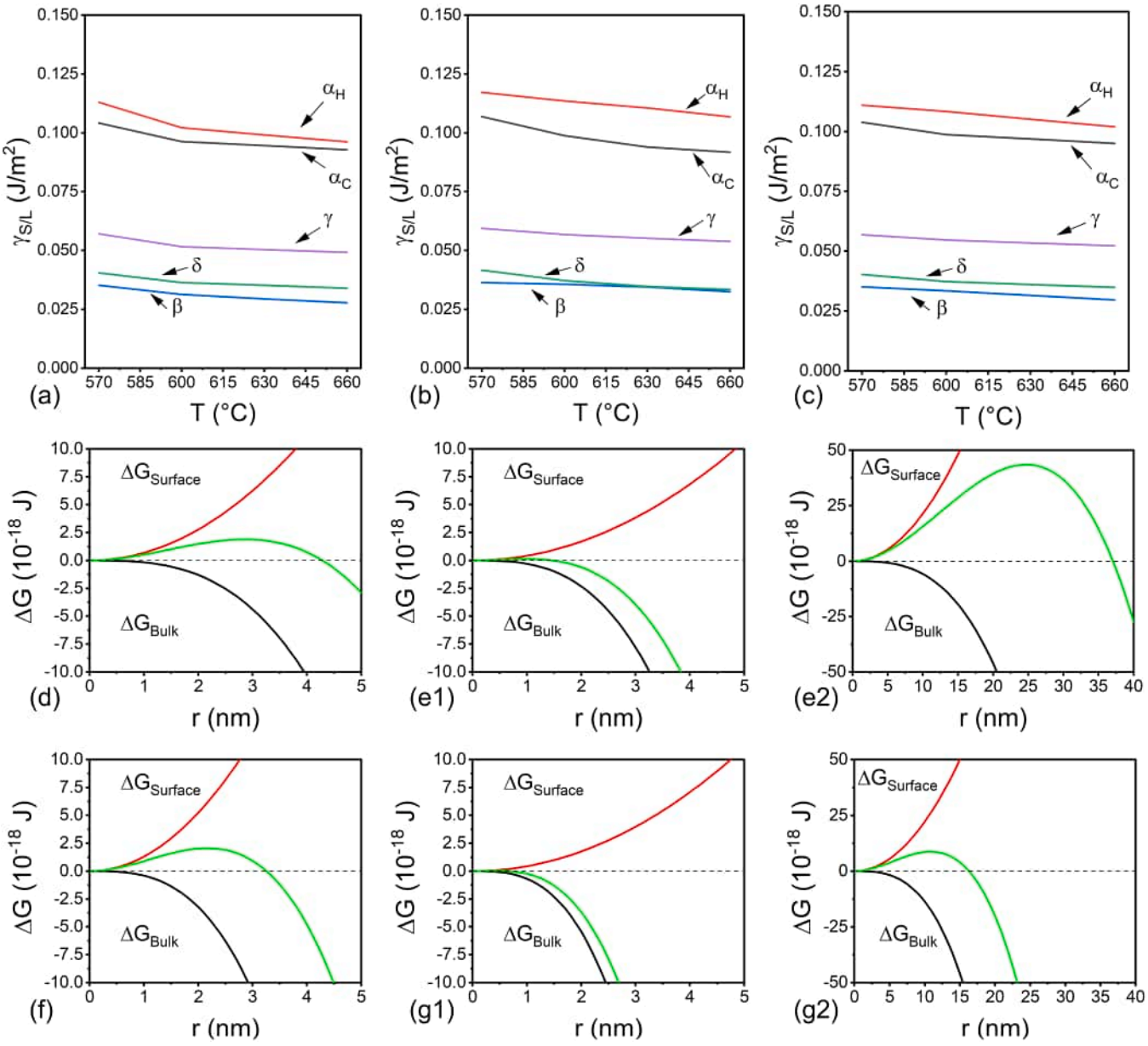

Fig. 17. Estimated specific solid/liquid interfacial energies ($\gamma_{S/L}$) and nucleation energy barriers (ΔG). (a-c) $\gamma_{S/L}$ as a function of temperature in a ternary-eutectic moderately-contaminated alloy (Al-12.67wt.%Si-0.89wt.%Fe), a far-from-eutectic severely-contaminated alloy (Al-7wt.%Si-2wt.%Fe), and a near-eutectic severely-contaminated alloy (Al-11wt.%Si-2wt.%Fe), respectively. (d) The nucleation energy barrier of γ phase in a near-eutectic severely-contaminated alloy (Al-11wt.%Si-2wt.%Fe) at a temperature of 590 °C assuming a spherical nucleus shape. (e1, e2) The nucleation energy barrier of β phase in a near-eutectic severely-contaminated alloy (Al-11wt.%Si-2wt.%Fe) at a temperature of 590 °C assuming spherical and spheroidal nucleus shapes, respectively, where *r* represents the major radius of the spheroid with an aspect ratio of 50. (f) The nucleation energy barrier of α_C phase in a ternary-eutectic moderately-contaminated alloy (Al-12.67wt.%Si-0.89wt.%Fe) at a temperature of 570 °C assuming a spherical nucleus shape. (g1, g2) The nucleation energy barrier of β phase in a ternary-eutectic moderately-contaminated alloy (Al-12.67wt.%Si-0.89wt.%Fe) at a temperature of 570 °C assuming spherical and spheroidal nucleus shape, respectively, where *r* represents the major radius of the spheroid with an aspect ratio of 50.

4. Discussion

The modeling approach in this study (Fig. 2) utilizes the simplified assumptions of the Scheil-Gulliver solidification model to approximate industrial casting conditions and predict solute segregation during solidification. The solute concentration in the liquid phase is crucial for accurately calculating the Gibbs free energy of different phases. The Scheil-Gulliver model simulates the upper limit of solute partitioning between solid and liquid phases. This is because it assumes infinite diffusion in the liquid and negligible diffusion in the solid. In contrast, diffusion-based models generally provide more accurate predictions for solute distribution by accounting for elemental diffusivity in solid and liquid phases. However, for the Al-Si-Fe-Mn system examined in this work, we believe the Scheil-Gulliver assumptions would yield reliable results for two reasons. First, Si, Fe, and Mn are sluggish substitutional diffusing elements in the solid phase, making considerable back diffusion into the solid unlikely. This contrasts with interstitial elements, such as C in Fe-based alloys, where the classical Scheil model would be unsuitable due to notable back diffusion. Second, the assumption of infinite diffusion in the liquid can be realized in practice through fluid mixing mechanisms, such as convection currents driven by thermal gradients or Marangoni flows influenced by local variations in

interfacial tension.

The classical Scheil model becomes unreliable under conditions of significant solute trapping during rapid cooling, where high solidification velocities reduce solute partitioning [75–77]. In such cases, the non-equilibrium partition coefficient deviates from its equilibrium value, becoming a function of the solidification velocity. High solidification velocities that induce significant solute trapping transition the solidification morphology from dendritic with secondary dendrite arms to cellular or banded (similar to those observed in additive manufacturing) [76,78,79]. In our study, the solidified microstructures exhibited predominantly a dendritic morphology suggesting that solute trapping is negligible. In scenarios of significant solute trapping, such as in additive manufacturing or welding, it is crucial to employ non-classical Scheil-Gulliver models that incorporate a non-equilibrium and velocity-dependent partition coefficient. These models enable more accurate predictions of solute segregation and, consequently, precipitation driving force. It is interesting to mention that the author attempted to use the non-classical Scheil with solute trapping model integrated within ThermoCalc. However, the predicted Fe-IMC phases according to the Scheil with solute trapping model did not differ from those predicted by the classic Scheil model, even at unrealistically high solidification velocities. We argue that, within the framework of this study, classical Scheil calculations provide reliable solute segregation values. The formation kinetics of Fe-IMC phases likely account for the discrepancies between the phases predicted by Scheil calculations (whether classical or non-classical) and those observed in the microstructures. This will be discussed in depth in the following sections.

4.1. Fe tolerance in the moderately-contaminated alloys (0.8 wt.% Fe)

The predicted Fe and Mn tolerances (Fig. 4) exhibit a qualitative agreement that pertains to the role of Mn as a neutralizer for Fe. Thermodynamic calculations propose that eliminating the platelet β phase (i.e., a corrected fraction of one) while simultaneously preventing the pre-eutectic formation of Fe-IMC phases is unattainable (Fig. 4(b)). Thus, a trade-off between the corrected phase fraction and the targeted Fe tolerance occurs. This result fundamentally agrees with the conventional wisdom suggesting that Mn addition should aim for partial correction of the platelet β phase [80]. Nevertheless, we anticipate that the predicted formation of the phases and their respective fractions will deviate from experimental observations at elevated cooling rates. This arises from the simplified assumptions of the Scheil-Gulliver model [54,55], which do not account for the role of nucleation kinetics in phase formation. Further elaboration on this aspect is provided in the following sections.

4.1.1. Microstructure characteristics and correlation with thermodynamic calculations

Both Al-7wt.%Si-0.8wt.%Fe and Al-11wt.%Si-0.8wt.%Fe alloys contain 0.8wt.% Fe and trace amounts of Mn. Based on the Fe and Mn tolerances depicted in Fig. 4(a), the Fe contamination level considerably exceeds the Fe tolerance in the 7wt.%Si alloy while only slightly surpassing it in the 11wt.%Si alloy. Thus, the pre-eutectic formation of the platelet β phase in the Al-7wt.%Si-0.8wt.%Fe alloy is expected to occur at a much earlier stage of solidification compared to the Al-11wt.%Si-0.8wt.%Fe alloy. The exact temperature at which the β phase becomes thermodynamically stable at the Al-7wt.%Si-0.8wt.%Fe alloy is approximately 16 °C higher than in the Al-11wt.%Si-0.8wt.%Fe alloy, as indicated by Figs. 5(b) and 5(c). Hence, per our hypothesis, we anticipate that the size of the platelet β phase in the Al-11wt.%Si-0.8wt.%Fe alloy will be considerably smaller than in the Al-7wt.%Si-0.8wt.%Fe alloy. In contrast to these expectations, the actual phases observed in the microstructures differ from those predicted through Scheil calculations.

Two aspects highlight the variance between the Fe-IMC phases observed in the moderately-contaminated alloys and those anticipated by the Scheil-Gulliver solidification model. Firstly, the stoichiometry of the platelet phase, particularly its high Si/Fe ratio, indicates likely the formation of the δ phase [56,80]. This means that the δ phase forms instead of the β phase predicted by Scheil calculations. Secondly, according to Scheil calculations, the Fe-IMC phases expected in the microstructures should exclusively manifest as β platelets without the presence of any Chinese-script or polyhedral phases. This prediction is based on the negligible presence of Mn in the alloys, suggesting that the corrected fraction value should approach zero (Fig. 4(b)). In contrast to these predictions, the experimentally observed microstructures not only feature a platelet phase but also encompass a high volume fraction of Chinese-script phases (Figs. 6 and 7). The formation of these Chinese-script phases was unforeseen by the Scheil calculations. EBSD indexing according to trigonal γ-Al_3FeSi and cubic α-AlMnSi crystal structures yielded acceptable confidence indexes greater than 0.1 and an excellent fit. The latter suggests that the metastable α_C Chinese-script phase in the Al-Fe-Si system is an isomorph or near-isomorph to the α-AlMnSi phase in the Al-Mn-Si system. The formation of the Chinese-script and the platelet δ phases was induced by the non-equilibrium solidification conditions in the region close to the mold wall. The SDAS values in this region suggest that both alloys experienced similar cooling rates, roughly around 3 K/s. This estimation is based on empirical relations found in the literature [81–86]. Despite the non-equilibrium solidification conditions, differences exist between the non-equilibrium phases identified in this work and those reported in prior studies.

Gorny et al. [87] previously studied the formation of Fe-IMC phases in an Al-7wt.%Si-0.5wt.%Fe alloy under cooling rates ranging from 0.017 to 50 K/s. They reported the formation of a non-equilibrium Chinese-script phase at solidification rates greater than 0.8 K/s. In their investigation, the composition of the Chinese-script phase was measured as $Al_{6.27}Fe_{1.8}Si$, and the crystal structure was identified as hexagonal. Both the composition and crystal structure were consistent with the α_H-Al_8Fe_2Si. Furthermore, the platelet phase observed in their research displayed a composition of $Al_{3.6}Fe_{1.03}Si$, indicating the formation of β-$Al_{4.5}FeSi$. In contrast, the stoichiometries and crystal structures of the Chinese-script and platelet phases in our study differ from the findings of Gorny et al. [87]. This discrepancy can be clarified through calculations of the driving force.

The precipitation driving force serves as a crucial scaling parameter for comprehending the kinetics of phase transformations. A positive driving force indicates phase stability and a tendency to precipitate, while a negative driving force suggests phase instability. By comparing the calculated driving force of different phases, we can roughly estimate the precipitation sequence and gain insights into the formation possibility of specific phases. The driving force is influenced by the local composition of the liquid phase at the solidification front under Scheil conditions, as well as by the temperature [61,72]. The ternary eutectic composition was selected as a suited model system with high engineering relevance to calculate the driving force of the Fe-IMC phases for two reasons. First, it possesses a narrow solidification range, thereby simplifying the calculations. Second, the non-equilibrium solidification process in eutectic systems typically concludes when the concentration of solutes segregated into the liquid reaches the eutectic composition. Hence, the ternary eutectic composition enables evaluating the formation of Fe-IMC phases at the end of solidification. As illustrated in Fig. 5(a), the first Fe-IMC phase exhibiting a positive driving force and a tendency to precipitate from the supersaturated liquid is β. However, the driving force lines for both β and δ phases closely approximate each other. This implies that the δ phase could potentially form instead of the β phase if the nucleation and growth kinetics of the β phase are slower than those of δ. Likewise, the driving force lines for the α_H phase reported in the work of Gorny et al. [87] and the α_C phase observed in this study nearly coincide. Therefore, we can conclude that the occurrence of both phases is possible from a driving force perspective. Determining which phase ultimately appears in the microstructure depends on other nucleation and growth parameters, such as interfacial energy and

density of viable nucleation sites, which is discussed in more depth in Section 4.4. Another Fe-IMC phase exhibiting a precipitation tendency is the γ phase. Consistent with our driving force predictions (Fig. 5(a)), the γ phase was detected in the microstructure of the moderately-contaminated alloys. Notably, the γ phase in the moderately-contaminated alloys assumes a very low volume fraction compared to the α_C phase (Fig. 7). Because both phases display similar Chinese-script morphology, they are likely to be confused with each other in a non-correlative metallographic analysis. As a result, distinguishing the γ phase from the α_C phase is challenging when relying solely on EDS or small-area EBSD scans. To accurately identify the γ phase, a large-area EBSD scan with a sufficiently small step size is recommended. This difficulty in detection explains the limited reports on the formation of the γ phase in commercial Al-Si alloys, with only one such report (to the best of the authors' knowledge) by Yu et al. [22], who conducted a transmission electron microscopy study on an Al-10wt.% Si-0.3wt.%Fe alloy. All the remaining Fe-IMC phases display a negative driving force, indicating that their formation is unlikely.

It is important to acknowledge the limitations associated with the parallel tangent construction procedure employed in this study. This method assumes the absence of the capillarity effect, hence neglecting the increase in free energies (per mole) of particles as their radius or respectively local curvature features decrease. This increase in free energy is attributed to the interfacial energy, which rises as the ratio of interfacial area to volume increases [72]. Consequently, the driving force in the presence of capillarity forces is lower than in its absence. The authors initially considered incorporating the capillarity effect into the analysis. We attempted to estimate the increase in Gibbs free energy (and the consequent decrease in driving force) employing the Gibbs–-Thomson equation for spherical particles [61,88], expressed as:

$$\Delta G = \frac{2 \cdot \gamma \cdot V_m}{r} \tag{8}$$

where γ is the specific interfacial energy, V_m is the molar volume of the precipitate, and r is the precipitate radius. However, by inserting the equilibrium molar volume of the Fe-IMC phases and arbitrarily small values for the interfacial energy, we found that the change in Gibbs free energy for small atomic clusters remained positive unless the clusters grew to a few nanometers in size. Only at this point did the change in Gibbs free energy become negative. This implies that atomic clusters would form and grow despite a negative driving force and a positive change in Gibbs free energy, which contradicts thermodynamic principles. This discrepancy arises from a mathematical artifact associated with the existence of a minimum cluster size (since the cluster radius cannot be smaller than that of an individual atom). Additionally, thermal fluctuations cause continuous formation and decomposition of clusters. Therefore, the applied equation is ill-defined for small atomic clusters, and atomistic models capable of capturing rare event dynamics must be considered to avoid the significant overestimation of the capillarity effect. Therefore, to maintain robustness and avoid the undue use of speculative assumptions, we neglected the capillarity effect and focused solely on the maximum driving force. Another limitation to consider is the nucleus composition. The nucleus composition is imperative for determining the driving force value and the precipitate/matrix interface energy [62]. Therefore, different nuclei compositions can yield varying nucleation activation energy barrier and nucleation rate values. According to Baker and Cahn [89], the thermodynamically possible nucleus composition ranges between two compositions. These two compositions correspond to where the tangent to the liquid phase Gibbs energy curve at the initial liquid composition intersects the precipitating solid phase Gibbs energy curve. These compositions typically result in a lower driving force compared to the assumed composition used in the parallel tangent procedure. Even though the calculated maximum driving force may overestimate the actual driving force, it remains a valuable tool for understanding phase transformations.

The Si content markedly impacts the development of Fe-IMC phases in the moderately-contaminated alloys (Fig. 6 and Table 4). Although the observed phases deviate from the predictions of the Scheil model, the near-eutectic alloy displays a more favorable microstructure in terms of the microstructure-property relationship. The differences in the characteristics of the Fe-IMC phases between the alloys are unlikely due to cooling rate variations, as the cooling conditions were identical for both alloys. This assertion is supported by the SDAS values. The SDASs were measured from the same micrographs used for quantifying the phase fractions and the shape descriptors of the Fe-IMC phases to ensure representative results. The Si concentration in the alloys influences the driving force evolution of the platelet and the Chinese script phases during solidification.

The precipitation driving force of the Fe-IMC phases during solidification explains the capability of the near-eutectic alloy to suppress the platelet phases and promote the Chinese-script phases. In the far-from-eutectic alloy, when the platelet β phase becomes stable, the near-eutectic alloy is still in the liquid state (Figs. 5(b) and 5(c)). As the undercooling of the β phase in the far-from-eutectic alloy reaches a point where the platelet δ phase stabilizes, the platelet phases in the near-eutectic alloy remain unstable. Only when the temperature in the near-eutectic alloy approaches the eutectic temperature do the platelet phases become thermodynamically stable. From the evolution of these driving forces, we can infer that the formation of the platelet δ phase in the far-from-eutectic alloy preceded the Al + Si eutectic reaction, i.e., occurred as a pre-eutectic reaction. This is evidenced by the presence of the relatively large δ platelets that are parallel to the adjacent Al dendrites in the far-from-eutectic alloy (Fig. 6(a)). In a related study, Kim et al. [90] observed the solidification behavior of Fe-enriched Al-Si-Cu alloys by synchrotron X-ray radiography. They reported that the platelet β phase that forms from the liquid through a binary eutectic reaction with the Al phase tends to grow parallel to neighboring Al dendrites. Unlike the varying formation temperatures of the platelet phases across the alloys, the Chinese-script phase occurrence is restricted to slight undercooling below the eutectic temperature. Therefore, there exists a wide window in the formation temperatures between the platelet phases and the Chinese-script phase in the far-from-eutectic alloy as opposed to a narrow window in the near eutectic alloy (Fig. 5(b) vs. 5(c)). The wide window suggests that far-from-eutectic alloys necessitate a higher undercooling and critical cooling rate to hinder the formation of the platelet β and δ phases and encourage the Chinese-script α phase. Furthermore, since the platelet phases tend to form at higher temperatures in the far-from-eutectic alloy, there is more time available for crystal growth. Hence, the maximum size of the platelet phase in the far-from-eutectic alloy is considerably higher than in the near-eutectic alloy. Owing to these factors, the near-eutectic alloy displays a more refined microstructure and a lower volume fraction of the detrimental platelet phase than the far-from-eutectic alloy.

4.1.2. *Mechanical properties and fracture behavior*

In cast Al alloys, there is a general consensus that the mechanical properties are linked to the solidification conditions through SDAS or dendrite cell size rather than by dendritic grain size [91–94]. Despite the variation in dendritic grain sizes with Si content (consistent with literature observations [95,96]), the SDAS values are approximately similar for both, the near-eutectic and the far-from-eutectic alloy variants (Fig. 6). In any case, the impact of SDAS on the yield strength of cast Al-Si alloys is known to be negligibly small [91,93]. However, tensile ductility depends on both SDAS and the characteristics of hard particles. These parameters influence the rate at which stress builds up on the particles, eventually leading to particle cracking [92,97]. Since the SDAS values are equivalent between near-eutectic and far-from-eutectic alloys, the dislocation slip distances are expected to be comparable [92]. Therefore, the differences in tensile ductility between the two types of alloys are primarily governed by the characteristics of the hard particles.

The near-eutectic alloy contains a significantly higher weight

percentage of Si, which can impact the mechanical properties. Si is inherently brittle, and its average elastic modulus and hardness are comparable to those of Fe-IMC phases [33,42,44]. It is well-established that an increase in the fraction of the platelet Si phase in Al-Si alloys leads to a reduction in ductility [98–100]. Given these considerations, one might anticipate that the near-eutectic alloy would exhibit degraded tensile properties compared to the far-from-eutectic alloy. Contrary to this expectation, the mechanical performance of the near-eutectic alloy demonstrates a considerable improvement of around 21% and 36.4% in the mean UTS and mean E_f, respectively, over the far-from-eutectic alloy. This can be attributed to the distribution of the Fe-IMC and Si phases within the alloys.

To comprehend the observed variations in the tensile properties, insights into the underlying damage mechanisms are essential. The fracture surface micrographs (Figs. 8(b)-8(d)) indicate that all the Fe-IMC and Si phases are potential damage initiation sites. When several brittle phases are present in the microstructure, the initiation and progression of cracks are influenced by their size, morphology, and clustering. Particles with large sizes and high aspect ratios display a reduced surface-to-volume ratio, leading to locally elevated stress concentration caused by the accumulation and pile-up of dislocation bands. Eventually, this results in particle cracking once the particle fracture stress is reached [92,101,102]. The large size and high aspect ratio of the platelet phases increase the likelihood of long cracks developing along the major axis of the platelets. These cracks pose a great threat, as they propagate rapidly through the brittle medium without undergoing plastic buffering and crack arresting. This heightens the risk of larger crack formation and linkage, leading ultimately to failure. In contrast, owing to the branched morphology and smaller size of the Chinese-script phase cracks initiating in the brittle fine branches are more prone to plastic arresting by the surrounding soft Al matrix. As a result, there is a lower probability of these cracks evolving into larger ones. This characteristic topological feature renders the Chinese script phase less detrimental to the mechanical properties. On the other hand, despite the elevated phase fraction of the Si phase in the near-eutectic alloy, it is finer than the platelet Fe-IMC phase (see Section 3.1.2 and Figs. 6(a) and 6(b)). This mitigates its negative impact on the properties compared to the platelet Fe-IMC phases. The finer Si size is due to the constrained formation of Si to the eutectic temperature in hypoeutectic Al-Si alloys. Conversely, the platelet Fe-IMC phases in the far-from-eutectic alloy are stable at a higher temperature, thus they have more time to coarsen. Based on the likelihood of crack formation in the Fe-IMC and Si phases, we can attribute the minor variation in tensile performance between the alloys to the following mechanisms. In the far-from-eutectic alloy, the higher volume fraction and larger maximum size of the detrimental platelet Fe-IMC phase undermine the benefits gained from the lower phase fraction and smaller maximum size of the Si phase. On the other hand, in the near-eutectic alloy, the lower volume fraction and smaller maximum size of the platelet Fe-IMC phase are counteracted by the higher phase fraction, larger maximum size, and clustering of the Si and the Chinses-script phases.

Lastly, we anticipate that the differences in mechanical properties between the alloys will diminish under rapid cooling conditions while becoming more apparent as the cooling rate decreases. This is because the phase fraction and size of the platelet phases rise in both alloys as they become less undercooled. However, this increase will be more pronounced in the far-from-eutectic alloy, as it requires higher undercooling to inhibit the platelet phases and reduce their size. During such slow cooling conditions, Mn addition may be crucial to neutralize Fe. The necessity arises from the hindered formation of the metastable Chinese script α_C-AlFeSi phase due to the reduced undercooling of the platelet phases. In this case, the Fe correction is achieved by forming the stable α_C-$Al_{15}(Fe, Mn)_3Si_2$ phase.

4.2. Fe tolerance in severely-contaminated alloys (2wt.% Fe)

In the preceding section, the Fe-contamination level in the moderately-contaminated alloys (0.8wt.% Fe) closely approaches the maximum predicted Fe tolerance of 0 .89wt.% Fe (Fig. 4(a)). However, as the Fe-contamination level sharply exceeds this value, it can cause substantial changes in phase equilibria. Consequently, the types of Fe-IMC phases that precipitate and the impact of undercooling can differ significantly from the case of moderate contamination. Thus, the severely-contaminated alloys (2.0wt.% Fe) with Fe concentrations more than twice the value of the maximum predicted tolerance were examined.

4.2.1. Microstructure characteristics and correlation with thermodynamic calculations

The formation of Fe-IMC phases in the severely-contaminated alloys is profoundly altered by the cooling rate. The cooling rate can be approximated at 50 K/s near the walls and 10 K/s near the center based on the SDAS values [81–86]. Near the wall, the high cooling rate promotes the formation of a fine polyhedral phase with a composition range akin to the platelet β phase (Table 6). Consequently, one might erroneously conclude that a rapid cooling rate would result in the spheroidization of the β phase. Contrary to this assumption, the monoclinic β phase does not form; instead, the trigonal γ phase does (Figs. 10(c) and 10(d)). The morphology of the γ phase transforms from a regular polyhedron in the near-eutectic alloy to a hollow polyhedron in the far-from-eutectic alloy. This morphological contrast is likely due to a difference in the solidification stage at which the γ phase forms. In the far-from-eutectic alloy, γ phase formation occurs through a coupled eutectic growth with the Al dendrites, while in the near-eutectic alloy, it forms as a primary crystal. This argument is reinforced by the precipitation driving force of the γ phase during solidification (Figs. 9(a) and 9(b)). In the far-from-eutectic alloy, the γ phase attains thermodynamic stability at approximately the dendrite formation temperature (613 °C). Whereas for the near-eutectic alloy, the γ phase becomes stable at a considerably higher temperature than the dendrite formation temperature (608 °C vs. 588 °C). Fundamentally, we can deduce that the γ phase formation in both alloys is pre-eutectic. This conclusion is drawn from the presence of the γ phase within the Al dendrites (Figs. 10(a) and 10(b)) rather than being embedded in the interdendritic region between the eutectic Si flakes. The latter is the case with the metastable Chinese-script phase in the Al-11wt.%Si-2wt.%Fe alloy (Fig. 10(b)). The absence of the metastable Chinese-script phase in the far-from-eutectic alloy further supports the claim that near-eutectic alloys promote its formation. It is noteworthy to elucidate the morphological distinctions between the hollow polyhedral γ phase and the Chinese-script α_C phase. The Chinese script α_C resembles a complex, highly-branched hollow polyhedron, whereas the γ phase manifests a simpler, lowly-branched, or even non-branched hollow polyhedral form. Near the center, the relatively slower cooling rate fails to inhibit the formation of the platelet phases. In both alloys, we can distinguish two categories of platelet phases based on their size: coarse and fine platelets. The stoichiometries of the coarse and fine platelet phases align with the compositions of the β phase and δ phase, respectively, as suggested by the Fe:Si ratios [56,80]. The Fe-IMC phases observed in the microstructure agree with the potential phases expected to form based on driving force calculations. Nevertheless, they deviate from those predicted by the Scheil-Gulliver solidification model (Table 5).

The presence of the platelet phases at the casting center of the Al-11wt.%Si-2wt.%Fe alloy agrees to a certain extent with the predictions of the Scheil model (Table 5), while in the Al-7wt.%Si-2wt.%Fe alloy, they deviate remarkably. The predicted solidification path for the Al-11wt.%Si-2wt.%Fe alloy indicates the formation of the β phase as both a primary and a eutectic phase, with no other Fe-IMC phases expected in the microstructure. This aligns partially with the experimental observation at the casting center, where the presence of the δ phase

contradicts the predictions of the Scheil model (Table 5). In the Al-7wt.%Si-2wt.%Fe alloy, the solidification path suggests the initiation of solidification with the primary α_H formation. As solidification progresses, the primary α_H phase should dissolve and transform into the β phase through a quasi-peritectic reaction. However, quasi-peritectic reactions involve sluggish diffusion of elements in the solid phase. Consequently, it may be anticipated that rapid cooling would hinder the β phase formation in the far-from-eutectic alloy. Hence, the microstructure should not contain any platelet β phase, with the polyhedral α_H phase being the only observed Fe-IMC. Contrary to expectations, a platelet-shaped β phase is present in the microstructure with no evidence of α_H phase formation. Similar findings were reported by Becker et al. [57] during the solidification of an Al-7.1wt.%Si-1.5wt.%Fe alloy, where the α_H phase ceased to form with increased cooling rates. This can be attributed to the nucleation competition between the β and α_H phases. As shown in Fig. 9(a), a slight undercooling by only 4 °C of the α_H phase from its formation temperature at 622 °C results in a precipitation tendency of the β phase. Therefore, the occurrence of the β phase rather than the α_H phase at elevated cooling rates suggests that the β phase experiences a lower nucleation undercooling compared to the α_H phase. This is because during nucleation competition, particles with a smaller nucleation undercooling, which is the difference between the equilibrium formation temperature and the actual nucleation temperature, are anticipated to nucleate first [103]. Although both alloys feature similar platelet Fe-IMC phases at the casting centers, they significantly differ in size.

The Si content has a prominent influence on the size of the platelet phases at the casting center of the severely-contaminated alloys. The far-from-eutectic Al-7wt.%Si-2wt.%Fe alloy offers better refinement ability to the platelet phase compared to the near-eutectic Al-11wt.%Si-2wt.%Fe alloy (Fig. 11). This contrasts with previous findings in moderately-contaminated alloys, where the maximum size of the platelet phase was lower in near-eutectic Al-11wt.%Si-0.8wt.%Fe alloy than in far-from-eutectic Al-7wt.%Si-0.8wt.%Fe alloy. Variations in the cooling rate, as evidenced by SDAS measurements, are negligible and do not contribute to the observed size difference. The smaller size of the coarse platelet β phase in the far-from-eutectic alloy can be explained through thermodynamic calculations. Initially, we can see from Fig. 9(c) that the temperature at which the driving force of the platelet β turns positive is slightly lower in the Al-7wt.%Si-2wt.%Fe alloy compared to the Al-11wt.%Si-2wt.%Fe alloy. The difference between the two temperatures is only about 2 °C. This case markedly differs from the moderately-contaminated alloys, where there is a substantial disparity in the precipitation temperature of the β phase between the Al-7wt.%Si-0.8wt.%Fe and Al-11wt.%Si-0.8wt.%Fe alloys (Figs. 5(b) and 5(c)). Thus, we can eliminate the delayed formation of the platelet β in the Al-7wt.%Si-2wt.%Fe alloy in contrast to the Al-11wt.%Si-2wt.%Fe alloy as the cause behind the observed refinement of the β phase. Secondly, at approximately 613 °C, which is the Al dendrite formation temperature in the Al-7wt.%Si-2wt.%Fe alloy, there is a sharp increase in the β phase driving force in the Al-7wt.%Si-2wt.%Fe alloy. According to nucleation theory, increasing the precipitation driving force leads to a smaller nucleus size and a higher nucleation rate [61,104]. As a result, more seeds become available for growth, leading to a finer grain structure. Hence, the greater precipitation driving force of the β phase in the Al-7wt.%Si-2wt.%Fe alloy, compared to the Al-11wt.%Si-2wt.%Fe alloy, explains the smaller platelet size. The size distribution of the platelet phases in the alloys affects their mechanical properties.

4.2.2. Mechanical properties and fracture behavior

The Al-7wt.%Si-2wt.%Fe alloy demonstrates superior mechanical properties than the Al-11wt.%Si-2wt.%Fe alloy due to the refined size of the platelet phase. Nevertheless, it is crucial to highlight that the standard deviation of the tensile properties in the Al-7wt.%Si-2wt.%Fe alloy is relatively high (the mean UTS and E_f values are 79 ± 37 MPa and 0.7 ± 0.5 %, respectively). This indicates a significant dispersion of the obtained tensile values about the mean. We validated the accuracy of the data by conducting tensile tests on specimens from two separate melts, testing a total of 11 tensile specimens. The underlying cause behind the large error bars could be the existence of shrinkage cavities in the cast pieces, as depicted in Fig. 11(a). Pores act as stress concentrators and reduce the effective cross-sectional area through which the load is distributed. This results in localized deformations and initiation of cracks at lower applied stresses [105,106]. The occurrence of pores at the cast center was expected, considering the elevated Fe content and pouring temperatures employed in this study. A high volume fraction of coarse intercepted Fe-IMC platelets restricts the molten metal flow during casting, leading to shrinkage cavities formation [1,10,107]. In addition, the high pouring temperature, even under near vacuum conditions, can cause intensified porosity. This happens likely due to the increased gas pickup in superheated melts [108,109]. The combination of pores and coarse platelet Fe-IMC phases is responsible for the early fracture of the tensile specimens. Technological issues such as shrinkage cavities can be mitigated by employing advanced casting methods like squeeze casting or high-pressure die casting, which enhance the liquid metal filling capacity.

The fracture behavior in the severely-contaminated alloys is governed primarily by the coarse platelet phase. This behavior contrasts the moderately-contaminated alloys wherein all the brittle phases play a major role in fracture. One potential crack initiation site is at branched coarse platelet particles. These branched structures originate from the physical obstruction of the growing platelet phases by adjacent growing Al dendrites or other platelet particles [110,111]. The intersection between two branched particles creates a notch formation. Such formations trigger stress concentration and potentially lead to longitudinal transgranular cracking. Subsequently, crack linkage occurs primarily along the coarse platelet Fe-IMC particles, especially those that are oriented perpendicular to the tensile axis (Fig. 12(d2)). Despite the growing longitudinal cracks, their propagation seems to be arrested when they diverge into the platelet/matrix interface (Fig. 12(c)). This behavior indicates strong cohesion between the platelet Fe-IMC phases and the Al matrix.

4.3. The influence of Mn on the severely-contaminated alloys (2wt.% Fe)

The addition of Mn to the severely-contaminated alloys is advantageous, particularly during slow and intermediate cooling, but offers no potential benefits during rapid cooling. The calculated SDAS values suggest similar cooling conditions as observed in the severely-contaminated samples without Mn addition, i.e., 50 K/s near walls and 10 K/s at the center. The chemical compositions of the mutual phases between the Mn-added and Mn-free severely-contaminated alloys are closely similar (Tables 6 and 8). This is because Mn and Fe are known to replace each other in the crystal structure of Fe-IMC phases [57,112]. As evident from the microstructure images of the region near the walls (Fig. 14), the Mn introduction did not yield any improvements to the already refined Fe-IMC phases. In contrast, Mn addition reduced the maximum size of the platelet phases by 60.3% and 81.3% for the near-eutectic (11wt.% Si) and far-from-eutectic (7wt.% Si) alloys, respectively, at the cast center (Fig. 15). Despite size improvements, the coarse platelet β phase persists in the microstructure of the Al-11wt.%Si-2wt.%Fe-0.5wt.%Mn alloy, suggesting that further enhancements could be realized with the addition of more Mn. On the other hand, the coarse platelet β phase was not detected in the Al-11wt.%Si-2wt.%Fe-0.5wt.%Mn alloy, and only the finer platelet δ phase was present. This indicates that Mn addition to the severely-contaminated alloys affects the formation of the platelet β phase in the near-eutectic alloy (11wt.% Si) differently from the far-from-eutectic alloy (7wt. %Si). Thermodynamic calculations explain this discrepancy.

The far-from-eutectic and near-eutectic alloys exhibit different driving force evolution and predicted solidification paths. In the far-from-eutectic alloy, the undercooling window between the α_C-Al_{15}(Fe,

$Mn)_3Si_2$ and β phases is wider compared to the near-eutectic alloy (Fig. 13). Applying the concept of nucleation competition as discussed in Section 4.2.1, a slight undercooling of the α_C-Al_{15}(Fe, $Mn)_3Si_2$ phase by only 3 °C is adequate for the β phase to become thermodynamically stable in the near-eutectic alloy, whereas it necessitates an 18 °C undercooling in the far-from-eutectic alloy. This indicates that inhibiting the formation of the β phase is more challenging in the near-eutectic alloy than in the far-from-eutectic alloy. Consequently, far-from-eutectic alloys require less Mn to suppress the formation of the platelet β phase compared to near-eutectic alloys, which demand a higher Mn content to widen the undercooling window. Moreover, the predictions of the Scheil-Gulliver solidification model provide insights into the platelet β phase formation (Table 7). In the solidification path of the Al-7wt.%Si-2wt.%Fe-0.5wt.%Mn alloy, a peritectic (or quasi-peritectic) reaction occurs at 607 °C, where the α_C-Al_{15}(Fe, $Mn)_3Si_2$ phase must dissolve for the β phase to form. However, this reaction is unlikely to proceed under rapid cooling conditions due to diffusion constraints. Conversely, the Al-11wt.%Si-2wt.%Fe-0.5wt.%Mn alloy does not involve any peritectic reactions for β platelet formation but undergoes a eutectic reaction at 613 °C (Table 7). Therefore, the suppression of β platelet formation due to solid-solid phase transformation does not occur in the near-eutectic alloy. Although the Mn-free Al-7wt.%Si-2wt.%Fe alloy follows a solidification path similar to the Mn-added Al-7wt.%Si-2wt.%Fe-0.5wt.% Mn alloy in terms of solid-solid phase transformation (Table 5), the absence of the α_H-Al_8Fe_2Si phase is notable in the microstructure of the former while the presence of α_C-Al_{15}(Fe, $Mn)_3Si_2$ is evident in the latter. This likely stems from the narrow undercooling window between the α_H and β phases (only 4 °C) compared to the wider window for the α_C and β phases (18 °C). Additionally, it suggests a higher nucleation rate for the α_C phase compared to the α_H phase, as the α_C emerged in the microstructure of the Al-11wt.%Si-2wt.%Fe-0 .5wt.%Mn alloy (Fig. 15(a)) even under the narrow 3 °C undercooling window (Fig. 13(b)).

It is noteworthy to discuss the identical growth orientation observed between the eutectic highly-branched Chinese-script α_C-Al_{15}(Fe, $Mn)_3Si_2$ phase and the adjacent primary polyhedral α_C-Al_{15}(Fe, $Mn)_3Si_2$ phase (Fig. 15(e)). This similar orientation suggests that the primary polyhedral α_C-Al_{15}(Fe, $Mn)_3Si_2$ phase, forming early during solidification, acts as a seed crystal for the nucleation of the Chinese-script α_C-Al_{15}(Fe, $Mn)_3Si_2$ phase, which forms at a later stage. The Chinese-script phase grows through a coupled eutectic reaction with the Al dendrites [1,10,12]. Therefore, the formation of the Al dendrites at a high temperature is a prerequisite for the early development of the Chinese-script phase during solidification. This renders the far-from-eutectic alloys advantageous, as Al dendrites are stable at elevated temperatures in these alloys compared to near-eutectic alloys. Consequently, we can deduce that far-from-eutectic alloys may have a greater potential to reduce the phase fraction of platelet phases in favor of increasing the phase fraction of the Chinese-script phase. This occurs as Fe segregates at the solid/liquid interface and is then absorbed by the thermodynamically stable α_C-Al_{15}(Fe, $Mn)_3Si_2$ phase, thus hindering the formation of the platelet phases. However, it is essential to note that this process is diffusion-controlled and heavily reliant on the cooling rate during solidification.

The enhanced ability of Mn addition to neutralize or, respectively, 'repair' Fe contamination in severely-contaminated far-from-eutectic alloys is reflected in the improvements of the tensile properties of these alloys after Mn addition. Significant improvements were observed in the far-from-eutectic alloy, while the near-eutectic alloy showed only modest overall enhancements (Fig. 15(f)). Notably, the variability in the values of the tensile properties that was pronounced in the Al-7wt.%Si-2wt.%Fe alloy (Fig. 12(a)) is no longer observed after Mn addition. This is attributed to the elimination of the coarse platelet phase in the far-from-eutectic alloy, which previously led to the formation of shrinkage cavities and caused premature failure.

4.4. Interfacial energy aspects

Interfacial energy plays a critical role in nucleation kinetics. A higher interfacial energy corresponds to a greater nucleation energy barrier, which renders the formation of stable nuclei more difficult and reduces the nucleation rate [72]. Nevertheless, directly measuring interfacial energy is often challenging. As a result, interfacial energy values are typically obtained indirectly through modeling or fitting to experimental data [63]. Here, we aim to use the modeling results of the driving force, interfacial energy, nucleation energy barrier, and critical radius to postulate the formation kinetics of Fe-IMC phases and discuss these modeling results in light of the observed microstructural characteristics.

By qualitatively examining the interfacial energy results (Figs. 17(a)-17(c)) and without considering the effects of nuclei shapes, we can draw several general conclusions that align with microstructural observations. First, in the Al-7wt.%Si-2wt.%Fe alloy, particularly in the region near the center subjected to intermediate cooling conditions (Fig. 11(a)), the equilibrium α_H phase does not form despite possessing the highest nucleation driving force (Fig. 9(a)). Instead, platelet β and δ phases are observed. This agrees with the estimated specific interfacial energies (Fig. 17(b)). The α_H phase consistently exhibits the highest specific interfacial energy, while the β and δ phases possess the lowest, with the interfacial energy of δ phase nearly equal to that of the β phase. Consequently, the α_H phase is the most difficult to nucleate, whereas the δ and β phases nucleate more readily. Second, in the Al-11wt.%Si-2wt.%Fe alloy, also in the center region experiencing intermediate cooling rates (Fig. 11(b)), the platelet β phase forms predominantly. This occurs even though the δ and α_H phases exhibit a positive driving force with slight undercooling of the β phase. If the β phase had a considerably higher interfacial energy than the δ or α_H phases, one would expect the formation of the δ or α_H phases instead of or alongside the β phase. However, this does not occur. Moreover, the higher interfacial energy of δ compared to β in the Al-11wt.%Si-2wt.%Fe alloy in contrast to the nearly equal interfacial energies of δ and β in the Al-7wt.%Si-2wt.%Fe alloy (Figs. 17(b) and 17(c)) suggests that the formation of the fine platelet δ phase is easier in the Al-7wt.%Si-2wt.%Fe alloy than in the Al-11wt.%Si-2wt.%Fe alloy. This aligns with the experimental results as we observe the presence of fine platelet δ phase in the Al-7wt.%Si-2wt.%Fe alloy and its absence in the Al-11wt.%Si-2wt.%Fe alloy (Fig. 11). A third observation that Further supports the interfacial energy results is the γ phase formation in severely contaminated alloys (Fig. 10). During rapid cooling of both Al-7wt.%Si-2wt.%Fe and Al-11wt.%Si-2wt.%Fe alloys, the γ phase forms instead of the platelet δ and β phases, as well as instead of the polyhedral α_C and α_H phases. This observation is consistent with the interfacial energy data, as the γ phase is the polyhedral phase with the lowest interfacial energy compared to the polyhedral α_C and α_H phases. Therefore, the formation of the γ phase is expected to dominate over the other polyhedral phases. However, a question arises as to why the polyhedral γ phase forms instead of the β and δ phases during rapid cooling. To address this question, we need to consider the nuclei shapes.

The exact shape of the nucleus is not well-established. However, for crystals that exhibit anisotropic growth due to strong anisotropy in interfacial energy, it is reasonable to presume that the nucleus shape resembles the equilibrium crystal shape [72]. When considering that the β phase assumes a spheroidal nucleus with an aspect ratio of 50, roughly similar to that of the coarse platelet phases in the Al-11wt.%Si-2wt.%Fe alloy, the β phase nucleation barrier becomes >20 times higher than that of the γ phase (Fig. 17(e2) vs. 17(d)). Additionally, the critical nucleus size of the β phase is over 25 times larger than that of the γ phase. This substantial increase in the nucleation energy barrier reduces the nucleation rate of the β phase. Moreover, the large critical nucleus size (25 nm) lowers the probability that atomic clusters can reach the critical nucleus size and form stable nuclei through thermal fluctuations. Given the large critical spheroidal nucleus size of the β phase, we can speculate that the γ phase forms exclusively during rapid cooling due to mobility constraints. Under intermediate and slow cooling rates, atoms have

adequate time and higher mobility at elevated temperatures, allowing them to reach the critical nucleus size for the β phase. However, during rapid cooling, mobility constraints prevent atomic clusters from reaching the critical size required to form stable β nuclei. We hypothesize that the pre-critical clusters of the β phase act as precursors for the γ phase nucleation, which has a lower energy barrier and smaller critical nucleus size. This hypothesis is supported by the observation that the γ phase has an identical composition to the β phase (Table 6). Furthermore, it might be that the nucleation of the β phase follows a non-classical pathway in which the β phase nucleates through the aggregation of stable γ phase clusters. Further research is necessary to validate this hypothesis.

All the aforementioned agreements pertain to the severely-contaminated alloys, in which Fe-IMC phases precipitate from the liquid before Al dendrites have formed or constituted a considerable fraction of the solid phase. However, in the moderately-contaminated alloys, Fe-IMC phases precipitate from the remaining liquid droplets after Al dendrites or even eutectic Si have already formed and accounted for a significant fraction of the solid phase. Consequently, two discrepancies arise when comparing the interfacial energy results with the observed microstructures of the moderately-contaminated alloys. First, although the β phase has a lower interfacial energy than the δ phase and both exhibit a platelet shape, the δ phase forms instead of the β phase (Figs. 6 and 7, and Table 3). Second, the phase fraction of the α_C phase is significantly higher, while the γ phase shows a substantially lower fraction (Fig. 7). This occurs despite the γ phase having much lower interfacial energy than the α_C phase, and both phases adopting polyhedral shapes. To explain these discrepancies, it is important to bear in mind that moderately-contaminated alloys contain additional interfaces, namely the Al dendrites and eutectic Si substrates. These additional interfaces can act as potent nucleation sites for some Fe-IMC phases while being less effective for others. For instance, if we compare the lattice parameters of the tetragonal δ phase and monoclinic β phase (Table 1) to the lattice parameter of Al ($a = 4.049$ Å), we can speculate that the interface between the tetragonal δ phase and Al dendrites likely has a lower lattice mismatch and less incoherency than the interface between the monoclinic β phase and Al dendrites. This would result in a lower δ/Al interfacial energy compared to β/Al interfacial energy. Similarly, we can also speculate that the Al dendrites and eutectic Si substrates favor the α_C phase in contrast to the trigonal γ phase. Indeed, what seems to be a nucleation relationship has been observed between the α_C phase and the eutectic Si (Figs. 7(e1)-7(e3)).

Finally, the quantitative results derived from CNT may deviate from experimental observations due to the assumptions of the CNT especially when applied to nanoscale systems [113–115]. For instance, CNT assumes that the physical properties of the clusters (such as composition, enthalpy, and entropy) are identical to that of macroscopic particles. This can lead to an overestimation of the driving force or an underestimation of the interfacial energy. Therefore, the quantitative results suggested by CNT should be interpreted with caution. This necessitates sophisticated modeling techniques like molecular dynamics simulations and density functional theory that consider atomic-scale interactions, atomic clustering behavior, and interface diffusion. Future research employing these advanced techniques will provide deeper insights into classical and non-classical nucleation pathways of Fe-IMC phases.

5. Conclusions

This study integrates thermodynamic calculations and experiments to investigate means for embracing Fe impurity in recycled Al-Si alloys. Evaluating the precipitation driving force and interfacial energy of Fe-containing intermetallic phases during non-equilibrium solidification under Scheil conditions is a suited and robust approach for assessing their formation tendency and predicting microstructure characteristics. The main conclusions of this work are as follows:

- The amount of Si in Fe-contaminated Al-Si alloys influences phase equilibria. Near-eutectic alloys with higher Si content differ notably from far-from-eutectic alloys with lower Si content in terms of the magnitude of the precipitation driving force evolution of Fe-IMC phases and their interfacial energy characteristics. As a result, these differences impact phase transformation reactions, govern which non-equilibrium phases emerge and their respective phase fractions, and determine the temperature and solidification stage at which Fe-IMC phases form and develop their sizes and distinctive morphologies. This contrast in the formation of Fe-IMC phases affects the Fe tolerance in Al-Si alloys.
- In Al-Si alloys with moderate Fe contamination (0.8wt.% Fe) at which Fe-IMC phases become thermodynamically stable at later solidification stages after the formation of Al dendrites, near-eutectic compositions enhance Fe tolerance by promoting the metastable Chinese script phase and inhibiting the detrimental platelet phases. This occurs because far-from-eutectic alloys require greater undercooling to suppress the platelet phases formation, making it more challenging to prevent their formation. In contrast, near-eutectic alloys exhibit a narrower undercooling window. Thus, it is easier to hinder the platelet phases formation. This leads to a refined microstructure and improved mechanical performance compared to far-from-eutectic alloys.
- In Al-Si alloys with moderate Fe contamination (0.8wt.% Fe), Mn addition becomes redundant with the increase in cooling rate. High cooling rates promote the formation of the metastable Chinese-script phase, thus achieving a high corrected fraction without Mn addition. However, in slow cooling casting processes, the controlled introduction of Mn can be advantageous to counter the dominance of the platelet phases over the metastable Chinese-script phase, especially in far-from-eutectic alloys.
- In Al-Si alloys with severe Fe contamination (2.0wt.% Fe) at which Fe-IMC phases form as primary crystals and become thermodynamically stable before the formation of the Al dendrites, far-from-eutectic compositions exhibit enhanced Fe tolerance over near-eutectic alloys. This is attributed to the higher precipitation driving force of the platelet phases in far-from-eutectic alloys, which increases the nucleation rate and reduces the critical nucleus size. Consequently, far-from-eutectic alloys are more effective at refining the detrimental platelet phases and mitigating their harmful effect. However, during rapid cooling, both near-eutectic and far-from-eutectic alloys demonstrate comparable Fe tolerance. This is due to the occurrence of the polyhedral γ phase instead of the platelet β phase in both alloys as a result of nucleation constraints.
- Introducing Mn to severely-contaminated alloys (2.0wt.% Fe) processed under rapid cooling rates (estimated as 50 K/s for the alloys studied in this work) is unnecessary. The strong undercooling effectively inhibits the platelet β and δ phases and facilitates the fine polyhedral γ phase formation. However, during slow and intermediate cooling (up to 10 K/s for the investigated alloys), the addition of Mn becomes essential to tackle the coarse platelet phases.
- In Mn-doped severely-contaminated alloys, the amount of Mn needed to eliminate the primary coarse platelet-shaped phases in far-from-eutectic alloys is lower than in near-eutectic alloys. This difference stems from the wider undercooling window observed between the α_C-$Al_{15}(Fe, Mn)_3Si_2$ and β phases in far-from-eutectic alloys. As a result, under non-equilibrium solidification conditions of far-from-eutectic alloys, it is challenging for the β phase to win the nucleation competition and nucleate ahead of the primary α_C-$Al_{15}(Fe, Mn)_3Si_2$ phase. In contrast, near-eutectic alloys require a lower nucleation undercooling of the primary α_C-$Al_{15}(Fe, Mn)_3Si_2$ phase for the β phase to form as coarse primary crystals.
- The formation of non-equilibrium Fe-IMC phases is a complex process influenced by numerous parameters, including the nucleus composition, degree of undercooling, and interfacial energy. The early nucleation stages of Fe-IMC phases are still poorly understood,

and non-classical nucleation pathways may be activated for certain Fe-IMC phases, such as the β phase. Therefore, more sophisticated modeling techniques like molecular dynamics or Monte Carlo simulations and density functional theory models that account for atomic interactions, clustering behavior, and interface diffusivity are necessary to bridge this knowledge gap.

CRediT authorship contribution statement

Waleed Mohammed: Writing – review & editing, Writing – original draft, Methodology, Investigation, Formal analysis, Conceptualization. **Xinren Chen:** Writing – review & editing, Conceptualization. **Dirk Ponge:** Writing – review & editing, Supervision. **Dierk Raabe:** Writing – review & editing, Supervision.

Declaration of competing interest

The authors declare that they have no known competing financial interests or personal relationships that could have appeared to influence the work reported in this paper.

Acknowledgements

This work was supported by the Amazon Development Center Germany GmbH under the Amazon & Max Planck Society Science Hub sustainability project award 2023. D. Klapproth and F. Rütters are gratefully acknowledged for performing the casting process.

Supplementary materials

Supplementary material associated with this article can be found, in the online version, at doi:10.1016/j.actamat.2025.120932.

Appendix A

The thermodynamic parameters of the Fe-IMC phases are provided in Table A1 below. The commercial encrypted TCAL 5 database used in this work restricts access to the detailed thermodynamic parameters. The authors believe that the following parameters selected from the literature [15, 116] can yield comparable results.

Table A 1
Thermodynamic parameters of Fe-IMC phases obtained from the literature [15,116].

τ1 or τ9
Model:
$(Al,Si)_{0.625}(Fe)_{0.375}$
Interaction parameters:
$G^{\tau 1}_{Al:Fe} = -22698.4 + 0.625\cdot {}^{\circ}G^{fcc}_{Al} + 0.375\cdot {}^{\circ}G^{bcc}_{Fe}$
$G^{\tau 1}_{Si:Fe} = -14651.3 + 0.625\cdot {}^{\circ}G^{dia}_{Si} + 0.375\cdot {}^{\circ}G^{bcc}_{Fe}$ ${}^{0}L^{\tau 1}_{Al,Si:Fe} = -45346.3 + 0.9465\cdot T$
${}^{1}L^{\tau 1}_{Al,Si:Fe} = 31401.9 - 16.83733\cdot T$
τ2 or γ
Model:
$(Al)_{0.5}(Fe)_{0.2}(Si)_{0.1}(Al,Si)_{0.2}$
Interaction parameters:
$G^{\tau 2}_{Al:Fe:Si:Al} = -27300 + 6.8\cdot T + 0.7\cdot {}^{\circ}G^{fcc}_{Al} + 0.2\cdot {}^{\circ}G^{bcc}_{Fe} + 0.1\cdot {}^{\circ}G^{dia}_{Si}$
$G^{\tau 2}_{Al:Fe:Si:Si} = -28700 + 8\cdot T + 0.5\cdot {}^{\circ}G^{fcc}_{Al} + 0.2\cdot {}^{\circ}G^{bcc}_{Fe} + 0.3\cdot {}^{\circ}G^{dia}_{Si}$
τ3
Model:
$(Al)_{0.55}(Fe)_{0.25}(Si)_{0.2}$
Interaction parameters:
$G^{\tau 3}_{Al:Fe:Si} = -24987.74 - 0.88568\cdot T + 0.55\cdot {}^{\circ}G^{fcc}_{Al} + 0.25\cdot {}^{\circ}G^{bcc}_{Fe} + 0.2\cdot {}^{\circ}G^{dia}_{Si}$
τ4 or δ
Model:
$(Al)_{0.4166}(Fe)_{0.1667}(Si)_{0.25}(Al,Si)_{0.1667}$
Interaction parameters:
$G^{\tau 4}_{Al:Fe:Si:Al} = -18100 + 0.5833\cdot {}^{\circ}G^{fcc}_{Al} + 0.1667\cdot {}^{\circ}G^{bcc}_{Fe} + 0.25\cdot {}^{\circ}G^{dia}_{Si}$
$G^{\tau 4}_{Al:Fe:Si:Si} = -24700 + 7\cdot T + 0.4166\cdot {}^{\circ}G^{fcc}_{Al} + 0.1667\cdot {}^{\circ}G^{bcc}_{Fe} + 0.4167\cdot {}^{\circ}G^{dia}_{Si}$
τ5 or α_H
Model:
$(Al)_{0.6612}(Fe)_{0.19}(Si)_{0.0496}(Al,Si)_{0.0992}$
Interaction parameters:
$G^{\tau 5}_{Al:Fe:Si:Al} = -28100 + 9.1\cdot T + 0.7604\cdot {}^{\circ}G^{fcc}_{Al} + 0.19\cdot {}^{\circ}G^{bcc}_{Fe} + 0.0496\cdot {}^{\circ}G^{dia}_{Si}$
$G^{\tau 5}_{Al:Fe:Si:Si} = -25310 + 5\cdot T + 0.6612\cdot {}^{\circ}G^{fcc}_{Al} + 0.19\cdot {}^{\circ}G^{bcc}_{Fe} + 0.1488\cdot {}^{\circ}G^{dia}_{Si}$
τ6 or β
Model:
$(Al)_{0.598}(Fe)_{0.152}(Si)_{0.1}(Al,Si)_{0.15}$
Interaction parameters:
$G^{\tau 6}_{Al:Fe:Si:Al} = -26900 + 12\cdot T + 0.748\cdot {}^{\circ}G^{fcc}_{Al} + 0.152\cdot {}^{\circ}G^{bcc}_{Fe} + 0.1\cdot {}^{\circ}G^{dia}_{Si}$
$G^{\tau 6}_{Al:Fe:Si:Si} = -19800 + 3\cdot T + 0.598\cdot {}^{\circ}G^{fcc}_{Al} + 0.152\cdot {}^{\circ}G^{bcc}_{Fe} + 0.25\cdot {}^{\circ}G^{dia}_{Si}$
τ7
Model:
$(A1,Si)_{0.75}(Fe)_{0.25}$
Interaction parameters:

(continued on next page)

Table A 1 (*continued*)

τ1 or τ9 Model:
$G^{\tau 7}_{Al:Fe} = -20798.1 + 0.75{\cdot}^{\circ}G^{fcc}_{Al} + 0.25{\cdot}^{\circ}G^{bcc}_{Fe}$
$G^{\tau 7}_{Si:Fe} = -9592.9 + 0.75{\cdot}^{\circ}G^{dia}_{Si} + 0.25{\cdot}^{\circ}G^{bcc}_{Fe}$
${}^{0}L^{\tau 7}_{Al,Si:Fe} = -29786.8 + 8.75305{\cdot}T$
τ8
Model:
$(Al,Si)_{0.6667}(Fe)_{0.3333}$
Interaction parameters:
$G^{\tau 8}_{Al:Fe} = -110.7 + 0.6667{\cdot}^{\circ}G^{fcc}_{Al} + 0.3333{\cdot}^{\circ}G^{bcc}_{Fe}$
$G^{\tau 8}_{Si:Fe} = -12111.3 + 0.6667{\cdot}^{\circ}G^{dia}_{Si} + 0.3333{\cdot}^{\circ}G^{bcc}_{Fe}$
${}^{0}L^{\tau 8}_{Al,Si:Fe} = -87571.1 + 8.27759{\cdot}\ T$
τ10
Model:
$(Al)_{0.6}(Fe)_{0.25}(Si)_{0.15}$
Interaction parameters:
$G^{\tau 10}_{Al:Fe:Si} = -26248 + 0.53427{\cdot}T + 0.6{\cdot}^{\circ}G^{fcc}_{Al} + 0.25{\cdot}^{\circ}G^{bcc}_{Fe} + 0.15{\cdot}^{\circ}G^{dia}_{Si}$
τ11
Model:
$(Al)_{0.65385}(Fe)_{0.23077}(Si)_{0.11539}$
Interaction parameters:
$G^{\tau 11}_{Al:Fe:Si} = -24537 + 0.07542{\cdot}T + 0.65385{\cdot}^{\circ}G^{fcc}_{Al} + 0.23077{\cdot}^{\circ}G^{bcc}_{Fe} + 0.11539{\cdot}^{\circ}G^{dia}_{Si}$
α_C
Model:
$(Al)_{0.6957}(Fe,Mn)_{0.1739}(Si)_{0.0435}(Al,Si)_{0.087}$
Interaction parameters:
$G^{\alpha}_{Al:Mn:Si:Al} = -551382 + 250.225{\cdot}T + 18{\cdot}^{\circ}G^{fcc}_{Al} + 4{\cdot}^{\circ}G^{cbcc}_{Mn} + {}^{\circ}G^{dia}_{Si}$
$G^{\alpha}_{Al:Mn:Si:Si} = -525358 + 167.895{\cdot}T + 16{\cdot}^{\circ}G^{fcc}_{Al} + 4{\cdot}^{\circ}G^{cbcc}_{Mn} + 3{\cdot}^{\circ}G^{dia}_{Si}$
$G^{\alpha}_{Al:Fe:Si:Al} = -785324 + 402.33{\cdot}T + 18{\cdot}^{\circ}G^{fcc}_{Al} + 4{\cdot}^{\circ}G^{bcc}_{Fe} + {}^{\circ}G^{dia}_{Si}$
$G^{\alpha}_{Al:Fe:Si:Si} = -716300 + 320{\cdot}T + 16{\cdot}^{\circ}G^{fcc}_{Al} + 4{\cdot}^{\circ}G^{bcc}_{Fe} + 3{\cdot}^{\circ}G^{dia}_{Si}$

Appendix B

$\frac{\partial H_{sol}}{\partial x_{pre}}$ can be derived as follows:

$$H_{sol} = (1 - x_{pre}){\cdot}H_{mat} + x_{pre}{\cdot}H_{pre} \tag{B.1}$$

$$\frac{\partial H_{sol}}{\partial x_{pre}} = H_{pre} - H_{mat} + (1 - x_{pre}){\cdot}\frac{\partial H_{mat}}{\partial x_{pre}} + x_{pre}{\cdot}\frac{\partial H_{pre}}{\partial x_{pre}} \tag{B.2}$$

where H_{sol} is the molar solution enthalpy, x_{pre} is the mole fraction of the precipitate phase, H_{mat} and H_{pre} are the molar enthalpies of the matrix and the precipitate, respectively. This formula can be further simplified by assuming that the Fe-IMC phases have a fixed stoichiometry. Hence $\frac{\partial H_{pre}}{\partial x_{pre}}$ would equal zero since the precipitate molar enthalpy would not change with the increase or decrease in the precipitate phase fraction. For a multicomponent system, the term $\frac{\partial H_{mat}}{\partial x_{pre}}$ can be calculated using the following expression:

$$\frac{\partial H_{mat}}{\partial x_{pre}} = \sum_{i}\frac{\partial H_{mat}}{\partial x_{i,mat}}{\cdot}\frac{\partial x_{i,mat}}{\partial x_{pre}} \tag{B.3}$$

where $x_{i,mat}$ is the mole fraction of component *i* in the matrix. The term $\frac{\partial x_{i,mat}}{\partial x_{pre}}$ can be obtained as follows:

$$X_i = (1 - x_{pre}){\cdot}x_{i,mat} + x_{pre}{\cdot}x_{i,pre} \tag{B.4}$$

where X_i is the mole fraction of component *i* in the system, $x_{i,mat}$ and $x_{i,pre}$ are the mole fractions of component *i* in the matrix and the precipitate, respectively. Taking the partial derivative with respect to x_{pre} :

$$\frac{\partial X_i}{\partial x_{pre}} = x_{i,pre} - x_{i,mat} + (1 - x_{pre}){\cdot}\frac{\partial x_{i,mat}}{\partial x_{pre}} + x_{pre}{\cdot}\frac{\partial x_{i,pre}}{\partial x_{pre}} \tag{B.5}$$

However, the mole fraction of a component *i* in the system is fixed, thus $\frac{\partial X_i}{\partial x_{pre}} = 0$. Moreover, since the Fe-IMC phases are stoichiometric, the mole fraction of a component *i* does not change with the phase fraction of the precipitate, thus $\frac{\partial x_{i,pre}}{\partial x_{pre}} = 0$. Hence the equation can be reduced to:

$$\frac{\partial x_{i,mat}}{\partial x_{pre}} = \frac{x_{i,mat} - x_{i,pre}}{(1 - x_{pre})} \tag{B.6}$$

Thus, the final formula for calculating $\frac{\partial H_{sol}}{\partial x_{pre}}$ becomes:

$$\frac{\partial H_{sol}}{\partial x_{pre}} = H_{pre} - H_{mat} + \sum_i \frac{\partial H_{mat}}{\partial x_{i,mat}} \cdot \left(x_{i,mat} - x_{i,pre}\right) \tag{B.7}$$

The negative of this value corresponds to ΔE_{sol}.

The surface area and volume of an oblate spheroid were calculated using:

$$S = 2 \cdot \pi \cdot r^2 + \pi \cdot \frac{\left(\frac{r}{A}\right)^2}{\sqrt{1 - \frac{1}{(A)^2}}} \cdot \ln \frac{1 + \sqrt{1 - \frac{1}{(A)^2}}}{1 - \sqrt{1 - \frac{1}{(A)^2}}} \tag{B.8}$$

$$V = \frac{4 \cdot \pi \cdot r^3}{3 \cdot A} \tag{B.9}$$

where S is the surface area, r is the major radius of the spheroid, A is the aspect ratio defined as the ratio between the major radius and the minor radius, and V is the volume. The aspect ratio for the oblate spheroid was obtained from the observed aspect ratios of the platelet phases in the microstructure.

References

[1] D. Raabe, D. Ponge, P. Uggowitzer, M. Roscher, M. Paolantonio, C. Liu, H. Antrekowitsch, E. Kozeschnik, D. Seidmann, B. Gault, F. Geuser, A. Dechamps, C. Hutchinson, C. Liu, Z. Li, P. Prangnell, J. Robson, P. Shanthraj, S. Vakili, S. Pogatscher, Making sustainable aluminum by recycling scrap: the science of "dirty" alloys, Prog. Mater. Sci. 128 (2022) 100947.

[2] D. Raabe, The materials science behind sustainable metals and alloys, Chem. Rev. 123 (5) (2023) 2436–2608.

[3] L. Stemper, M.A. Tunes, R. Tosone, P.J. Uggowitzer, S. Pogatscher, On the potential of aluminum crossover alloys, Prog. Mater. Sci. 124 (2022) 100873.

[4] S. Das, Designing aluminium alloys for a recycling friendly world, Materials Science Forum 519 (521) (2006) 1239–1244.

[5] W.S. Miller, L. Zhuang, J. Bottema, A.J. Wittebrood, P. De Smet, A. Haszler, A. Vieregge, Recent development in aluminium alloys for the automotive industry, Mater. Sci. Eng. A 280 (1) (2000) 37–49.

[6] D. Raabe, C.C. Tasan, E.A. Olivetti, Strategies for improving the sustainability of structural metals, Nat 575 (7781) (2019) 64–74.

[7] I. Dugic, F. Henriksson, C. Strebel, Ö. Kosmaz, S. Seifeddine, On the effect of alloying element range on the mechanical properties of recycled aluminium alloy EN AB-46000, in: E. Williams (Ed.), Light Metals, Springer International Publishing, Cham, 2016, pp. 115–120, 2016.

[8] D. Paraskevas, K. Kellens, W. Dewulf, J. Duflou, Closed and open loop recycling of aluminium: a life cycle assessment perspective, 2013.

[9] E. David, J. Kopac, Use of separation and impurity removal methods to improve aluminium waste recycling process, mater, Today Proc 2 (10) (2015) 5071–5079. Part A.

[10] L. Zhang, J. Gao, L. Damoah, D. Robertson, Removal of iron from aluminum: a review, Miner. Process. Extr. Metall. Rev 33 (2012) 99–157.

[11] J.A. Taylor, Iron-containing intermetallic phases in Al-Si based casting alloys, Procedia Mater. Sci. 1 (2012) 19–33.

[12] Z. Que, Y. Wang, C.L. Mendis, C. Fang, J. Xia, X. Zhou, Z. Fan, Understanding Fe-containing intermetallic compounds in Al alloys: an overview of recent advances from the LiME Research Hub, Metals (Basel) (2022).

[13] V. Raghavan, Al-Fe-Si (aluminum-iron-silicon), J. Phase Equilibria Diffus. 30 (2) (2009) 184–188.

[14] G. Ghosh, Al-Fe-Si (Aluminium - Iron - Silicon): datasheet from Landolt-Börnstein - Group IV Physical Chemistry Volume 11A2: "Light Metal Systems. Part 2" in SpringerMaterials (https://doi.org/10.1007/10915967_27), Springer-Verlag Berlin Heidelberg.

[15] Y. Du, J.C. Schuster, Z.-K. Liu, R. Hu, P. Nash, W. Sun, W. Zhang, J. Wang, L. Zhang, C. Tang, Z. Zhu, S. Liu, Y. Ouyang, W. Zhang, N. Krendelsberger, A thermodynamic description of the Al–Fe–Si system over the whole composition and temperature ranges via a hybrid approach of CALPHAD and key experiments, Intermetallics. (Barking) 16 (4) (2008) 554–570.

[16] Á. Griger, V. Stefániay, Equilibrium and non-equilibrium intermetallic phases in Al-Fe and Al-Fe-Si alloys, J. Mater. Sci. 31 (24) (1996) 6645–6652.

[17] L.A. Bendersky, A.J. McAlister, F.S. Biancaniello, Phase transformation during annealing of rapidly solidified Al- rich Al- Fe- Si alloys, Metall. Trans. A 19 (12) (1988) 2893–2900.

[18] L. Sweet, S.M. Zhu, S.X. Gao, J.A. Taylor, M.A. Easton, The effect of iron content on the iron-containing intermetallic phases in a cast 6060 aluminum alloy, Metall. Mater. Trans. A 42 (7) (2011) 1737–1749.

[19] M. Timpel, N. Wanderka, R. Grothausmann, J. Banhart, Distribution of Fe-rich phases in eutectic grains of Sr-modified Al–10wt.% Si–0.1wt.% Fe casting alloy, J. Alloys. Compd. 558 (2013) 18–25.

[20] T. Yanson, M. Manyako, O. Bodak, N. German, O. Zarechnyuk, R. Cerny, V. Pacheco, K. Yvon, Triclinic Fe3Al2Si3 and orthorhombic Fe3Al2Si4 with new structure types, Acta Crystallogr. Sect. C: Cryst. Struct. Commun. 52 (1996) 2964–2967.

[21] J. Roger, E. Jeanneau, J. Viala, Crystal structure of the ternary compound γ-Al3FeSi, Z. Kristallogr, Cryst. Mater 226 (2011) 805–813.

[22] J.M. Yu, N. Wanderka, G. Miehe, J. Banhart, Intermetallic phases in high purity Al-10Si-0.3Fe cast alloys with and without Sr modification studied by FIB tomography and TEM, Intermetallics. (Barking) 72 (2016) 53–61.

[23] D. Munson, A clarification of the phases occurring in aluminium-rich aluminium-iron-silicon alloys, with particular reference to the ternary phase alpha-AlFeSi, J. Inst. Met. 95 (7) (1967) 217–219.

[24] N. German, V. Zavodnik, T. Yanson, O. Zarechnyuk, Crystal structure of FeAl sub 2 Si, Kristallografiya 34 (3) (1989) 738–739.

[25] M.V. Kral, A crystallographic identification of intermetallic phases in Al–Si alloys, Mater. Lett. 59 (18) (2005) 2271–2276.

[26] J. Roger, F. Bosselet, J.C. Viala, X-rays structural analysis and thermal stability studies of the ternary compound α-AlFeSi, J. Solid. State Chem. 184 (5) (2011) 1120–1128.

[27] C. Rømming, V. Hansen, J. Gjønnes, Crystal structure of β-Al4. 5FeSi, Acta crystallogr. Sect. B: struct, Sci 50 (3) (1994) 307–312.

[28] C. Gueneau, C. Servant, F. d'Yvoire, N. Rodier, Fe2Al3Si3, Acta Crystallogr. Sect. C: cryst. Struct, Commun. 51 (12) (1995) 2461–2464.

[29] N. Krendelsberger, F. Weitzer, J.C. Schuster, On the reaction scheme and liquidus surface in the ternary system Al-Fe-Si, Metall. Mater. Trans. A 38 (8) (2007) 1681–1691.

[30] N. German, V. Belskii, T. Yanson, G. Zarechnyuk, Crystal structure of the compound Fe sub 1. 7 Al sub 4 Si, Sov. Phys. Crystallogr. 34 (3) (1989) 437–438.

[31] M. Cooper, K. Robinson, The crystal structure of the ternary alloy α (AlMnSi), Acta Crystallogr. 20 (5) (1966) 614–617.

[32] M. Cooper, The crystal structure of the ternary alloy α (AlFeSi), Acta Crystallogr. 23 (6) (1967) 1106–1107.

[33] X. Zhang, D. Wang, Y. Zhou, X. Chong, X. Li, H. Zhang, H. Nagaumi, Exploring crystal structures, stability and mechanical properties of Fe, Mn-containing intermetallics in Al-Si Alloy by experiments and first-principles calculations, J. Alloys. Compd. 876 (2021) 160022.

[34] J.E. Yoo, A. Shan, I.G. Moon, S.J. Maeng, A study on composition and crystal structure of dispersoids in AlMgSi alloys, J. Mater. Sci. 34 (11) (1999) 2679–2683.

[35] H.Y. Kim, T.Y. Park, S.W. Han, H.M. Lee, Effects of Mn on the crystal structure of α-Al(Mn,Fe)Si particles in A356 alloys, J. Cryst. Growth 291 (1) (2006) 207–211.

[36] C.B. Basak, N. Hari Babu, Morphological changes and segregation of β-Al9Fe2Si2 phase: a perspective from better recyclability of cast Al-Si alloys, Mater. Des. 108 (2016) 277–288.

[37] J.A. Taylor, D.H. St John, J. Barresi, M.J. Couper, An empirical analysis of trends in mechanical properties of T6 heat treated Al-Si-Mg casting alloys, Int. J. Cast Met. Res. 12 (6) (2000) 419–430.

[38] A.M.A. Mohamed, A.M. Samuel, F.H. Samuel, H.W. Doty, Influence of additives on the microstructure and tensile properties of near-eutectic Al–10.8%Si cast alloy, Mater. Des. 30 (10) (2009) 3943–3957.

[39] J. Malavazi, R. Baldan, A.Augusto Couto, Microstructure and mechanical behaviour of Al9Si alloy with different Fe contents, Mater. Sci. Technol 31 (6) (2015) 737–744.

[40] S. Seifeddine, I.L. Svensson, The influence of Fe and Mn content and cooling rate on the microstructure and mechanical properties of A380-die casting alloys, Metall. Sci. Tecnol. 27 (1) (2009).

[41] A. Bjurenstedt, S. Seifeddine, A.E.W. Jarfors, The effects of Fe-particles on the tensile properties of Al-Si-Cu alloys, Metals (Basel) (2016).

[42] J. Mathew, G. Remy, M.A. Williams, F. Tang, P. Srirangam, Effect of Fe intermetallics on microstructure and properties of Al-7Si alloys, JOM 71 (12) (2019) 4362–4369.

[43] L. Kuchariková, D. Medvecká, E. Tillová, J. Belan, M. Kritikos, M. Chalupová, M. Uhríčik, The effect of the β-Al5FeSi phases on microstructure, mechanical and fatigue properties in A356.0 cast alloys with higher Fe content without additional alloying of Mn, Materials (Basel) (2021).

[44] S. Seifeddine, S. Johansson, I.L. Svensson, The influence of cooling rate and manganese content on the β-Al5FeSi phase formation and mechanical properties of Al–Si-based alloys, Mater. Sci. Eng. A 490 (1) (2008) 385–390.

[45] D. Bösch, S. Pogatscher, M. Hummel, W. Fragner, P.J. Uggowitzer, M. Göken, H. W. Höppel, Secondary Al-Si-Mg high-pressure die casting alloys with enhanced ductility, Metall. Mater. Trans. A 46 (3) (2015) 1035–1045.
[46] H.Y. Kim, S.W. Han, H.M. Lee, The influence of Mn and Cr on the tensile properties of A356–0.20Fe alloy, Mater. Lett. 60 (15) (2006) 1880–1883.
[47] J.Y. Hwang, H.W. Doty, M.J. Kaufman, The effects of Mn additions on the microstructure and mechanical properties of Al–Si–Cu casting alloys, Mater. Sci. Eng. A 488 (1) (2008) 496–504.
[48] D. Song, Y. Zhao, Z. Wang, Y. Jia, H. Huang, D. Zhang, W. Zhang, Effect of Mn/Fe ratio on Fe removal efficiency and tensile ductility of an Al–7.0Si–2.4Fe alloy, J. Mater. Res (2021) 1–10.
[49] R. Baldan, J. Malavazi, A.A. Couto, Microstructure and mechanical behavior of Al9Si0.8Fe alloy with different Mn contents, Mater. Sci. Technol 33 (10) (2017) 1192–1199.
[50] T. Gao, K. Hu, L. Wang, B. Zhang, X. Liu, Morphological evolution and strengthening behavior of α-Al(Fe,Mn)Si in Al–6Si–2Fe–xMn alloys, Results. Phys. 7 (2017) 1051–1054.
[51] D. Song, Y. Zhao, Y. Jia, R. Li, N. Zhou, K. Zheng, Y. Fu, W. Zhang, Study of the evolution mechanisms of Fe-rich phases in Al-Si-Fe alloys with Mn modification using synchrotron X-ray imaging, J. Alloys. Compd. 915 (2022) 165378.
[52] Y. Sun, X. Huang, C. Liu, M. Zhou, X. Zhang, Impurity iron separation from molten secondary aluminum by pulsed electric current, J. Alloys. Compd. 934 (2023) 167903.
[53] E. Cinkilic, C.D. Ridgeway, X. Yan, A.A. Luo, A formation map of iron-containing intermetallic phases in recycled cast aluminum alloys, Metall. Mater. Trans. A 50 (12) (2019) 5945–5956.
[54] E. Scheil, Bemerkungen zur schichtkristallbildung, Int. J. Mater. Res. 34 (3) (1942) 70–72.
[55] G.H. Gulliver, The quantitative effect of rapid cooling upon the constitution of binary alloys, J. Inst. Met. 9.
[56] W. Khalifa, F.H. Samuel, J.E. Gruzleski, Iron intermetallic phases in the Al corner of the Al-Si-Fe system, Metall. Mater. Trans. A 34 (3) (2003) 807–825.
[57] H. Becker, T. Bergh, P.E. Vullum, A. Leineweber, Y. Li, Effect of Mn and cooling rates on α-, β- and δ-Al–Fe–Si intermetallic phase formation in a secondary Al–Si alloy, Materialia (Oxf) 5 (2019) 100198.
[58] Z. Zhang, H. Tezuka, E. Kobayashi, T. Sato, Effects of the Mn/Fe ratio and cooling rate on the modification of Fe intermetallic compounds in cast A356 based alloy with different Fe contents, Mater. Trans 54 (8) (2013) 1484–1490.
[59] J.O. Andersson, T. Helander, L. Höglund, P. Shi, B. Sundman, Thermo-Calc & DICTRA, computational tools for materials science, CALPHAD. 26 (2) (2002) 273–312.
[60] H.-L. Chen, Q. Chen, A. Engström, Development and applications of the TCAL aluminum alloy database, CALPHAD. 62 (2018) 154–171.
[61] K. Janssens, D. Raabe, E. Kozeschnik, M. Miodownik, B. Nestler, Computational Materials Engineering: An Introduction to Microstructure Evolution, Elsevier, 2007.
[62] G. Kaptay, Beyond the parallel tangent method to predict the composition of the first nucleating phase from oversaturated solutions, J. Phase Equilib. Diffus. 44 (3) (2023) 445–455.
[63] B. Sonderegger, E. Kozeschnik, Generalized nearest-neighbor broken-bond analysis of randomly oriented coherent interfaces in multicomponent fcc and bcc structures, Metall. Mater. Trans. A 40 (3) (2009) 499–510.
[64] E. Kozeschnik, Mean-field microstructure kinetics modeling, in: F.G. Caballero (Ed.), Encyclopedia of Materials: Metals and Alloys, Elsevier, Oxford, 2022, pp. 521–526.
[65] K. Sugiyama, N. Kaji, K. Hiraga, *Re*-refinement of α-(AlMnSi), Acta Crystallogr. Sect. C: Cryst. Struct. Commun. 54 (1998) 445–447.
[66] K. Sugiyama, N. Kaji, K. Hiraga, Crystal structure of rhombohedral λ-AlFeSi, J. Alloys. Compd. 368 (1) (2004) 251–255.
[67] H. Becker, T. Bergh, P.E. Vullum, A. Leineweber, Y. Li, β- and δ-Al-Fe-Si intermetallic phase, their intergrowth and polytype formation, J. Alloys. Compd. 780 (2019) 917–929.
[68] V. Hansen, B. Hauback, M. Sundberg, C. Rømming, J. Gjønnes, β-Al4.5FeSi: a combined synchrotron powder diffraction, electron diffraction, high-resolution electron microscopy and single-crystal X-ray diffraction study of a faulted structure, Acta Crystallogr. Sect. B: Struct. Sci. 54 (4) (1998) 351–357.
[69] R. Hoppe, Effective coordination numbers (ECoN) and mean fictive ionic radii (MEFIR), Z. Kristallogr. Cryst. Mater. 150 (1–4) (1979) 23–52.
[70] J.L.F. Da Silva, Effective coordination concept applied for phase change (GeTe)m (Sb2Te3)n compounds, J. Appl. Phys. 109 (2) (2011).
[71] R. Hoppe, S. Voigt, H. Glaum, J. Kissel, H.P. Müller, K. Bernet, A new route to charge distributions in ionic solids, J. Less Common Met. 156 (1) (1989) 105–122.
[72] by R. Balluffi, S. Allen, W. Carter, in: Robert W. Balluffi, Samuel M. Allen, W. Craig Carter (Eds.), Kinetics of Materials, Kinetics of Materials, Wiley-VCH, 2005, p. 672. byISBN 0-471-24689-1September 2005.
[73] J. Schindelin, I. Arganda-Carreras, E. Frise, V. Kaynig, M. Longair, T. Pietzsch, S. Preibisch, C. Rueden, S. Saalfeld, B. Schmid, J.-Y. Tinevez, D.J. White, V. Hartenstein, K. Eliceiri, P. Tomancak, A. Cardona, Fiji: an open-source platform for biological-image analysis, Nat. Methods 9 (7) (2012) 676–682.
[74] J.C. Russ, The Image Processing Handbook, 7th edition, 7 ed., CRC Press, London, England, 2016.
[75] W. Kurz, R. Trivedi, Rapid solidification processing and microstructure formation, Mater. Sci. Eng. A 179 (180) (1994) 46–51.
[76] T. Pinomaa, A. Laukkanen, N. Provatas, Solute trapping in rapid solidification, MRS Bull 45 (11) (2020) 910–915.
[77] M.R. Rolchigo, R. LeSar, Modeling of binary alloy solidification under conditions representative of Additive Manufacturing, Comput. Mater. Sci. 150 (2018) 535–545.
[78] J. Berry, A. Perron, J.-L. Fattebert, J.D. Roehling, B. Vrancken, T.T. Roehling, D. L. Rosas, J.A. Turner, S.A. Khairallah, J.T. McKeown, M.J. Matthews, Toward multiscale simulations of tailored microstructure formation in metal additive manufacturing, Mater. Today 51 (2021) 65–86.
[79] N.T. Aboulkhair, M. Simonelli, L. Parry, I. Ashcroft, C. Tuck, R. Hague, 3D printing of aluminium alloys: additive manufacturing of aluminium alloys using selective laser melting, Prog. Mater. Sci. 106 (2019) 100578.
[80] L.F. Mondolfo, Aluminum Alloys: Structure and Properties, Butterworths and Co., Ltd., London, 1976.
[81] A.M. Samuel, F.H. Samuel, Effect of alloying elements and dendrite arm spacing on the microstructure and hardness of an Al-Si-Cu-Mg-Fe-Mn (380) aluminium die-casting alloy, J. Mater. Sci. 30 (7) (1995) 1698–1708.
[82] J.-I. Cho, C.-W. Kim, Y.-C. Kim, S.-W. Choi, C.-S. Kang, The relationship between dendrite arm spacing and cooling rate of Al-Si casting alloys in high pressure die casting, in: H. Weiland, A.D. Rollett, W.A. Cassada (Eds.), ICAA13 Pittsburgh, Springer International Publishing, Cham, 2016, pp. 1493–1498.
[83] R. Chen, Q. Xu, B. Liu, Cellular automaton simulation of three-dimensional dendrite growth in Al–7Si–Mg ternary aluminum alloys, Comput. Mater. Sci. 105 (2015) 90–100.
[84] G. Gustafsson, T. Thorvaldsson, G.L. Dunlop, The influence of Fe and Cr on the microstructure of cast Al-Si-Mg alloys, Metall. Trans. A 17 (1) (1986) 45–52.
[85] T. Sivarupan, C.H. Caceres, J.A. Taylor, Alloy composition and dendrite arm spacing in Al-Si-Cu-Mg-Fe alloys, Metall. Mater. Trans. A 44 (9) (2013) 4071–4080.
[86] M. Okayasu, Y. Ohkura, S. Takeuchi, S. Takasu, H. Ohfuji, T. Shiraishi, A study of the mechanical properties of an Al–Si–Cu alloy (ADC12) produced by various casting processes, Mater. Sci. Eng. A 543 (2012) 185–192.
[87] A. Gorny, J. Manickaraj, Z. Cai, S. Shankar, Evolution of Fe based intermetallic phases in Al–Si hypoeutectic casting alloys: influence of the Si and Fe concentrations, and solidification rate, J. Alloys. Compd. 577 (2013) 103–124.
[88] J.W. Christian, CHAPTER 6 - solid solutions, in: J.W. Christian (Ed.), The Theory of Transformations in Metals and Alloys, 2002, pp. 171–234. Pergamon, Oxford.
[89] J.C. Baker, J.W. Cahn, Thermodynamics of Solidification, the selected works of John W, Cahn (1998) 253–288.
[90] B. Kim, S. Lee, S. Lee, H. Yasuda, Real-time radiographic observation of solidification behavior of Al-Si-Cu casting alloys with the variation of iron content, Mater. Trans 53 (2) (2012) 374–379.
[91] C.H. Cáceres, A rationale for the quality index of Al-Si-Mg casting alloys, Int. J. Cast Met. Res. 10 (5) (1998) 293–299.
[92] Q.G. Wang, Microstructural effects on the tensile and fracture behavior of aluminum casting alloys A356/357, Metall. Mater. Trans. A 34 (12) (2003) 2887–2899.
[93] Q.G. Wang, M. Praud, A. Needleman, K.S. Kim, J.R. Griffiths, C.J. Davidson, C. H. Cáceres, A.A. Benzerga, Size effects in aluminium alloy castings, Acta Mater. 58 (8) (2010) 3006–3013.
[94] C.H. Cáceres, Q.G. Wang, Dendrite cell size and ductility of Al—Si—Mg casting alloys: spear and Gardner revisited, Int. J. Cast Met. Res. 9 (3) (1996) 157–162.
[95] S. Manani, A. Patodi, M.N. Verma, A.K. Pradhan, Comparative study of microstructure and properties of hypoeutectic Al-Si alloys being cast with and without melt thermal treatment, Metallogr. Microstruct. Anal. 11 (3) (2022) 415–424.
[96] J. Liu, J.C. Jie, B. Peng, J.P. Qu, X.L. Wang, T.J. Li, Revealing the effect of Si content on the microstructure and properties of Al–Si alloy by experiments and phase-field simulation, J. Mater. Res. Technol. 27 (2023) 651–663.
[97] C.H. Cáceres, C.J. Davidson, J.R. Griffiths, The deformation and fracture behaviour of an Al Si Mg casting alloy, Mater. Sci. Eng. A 197 (2) (1995) 171–179.
[98] J.R. Davis, Aluminum and Aluminum Alloys, ASM international, Materials Park, OH, USA, 1998.
[99] S. Hegde, K.N. Prabhu, Modification of eutectic silicon in Al–Si alloys, J. Mater. Sci. 43 (9) (2008) 3009–3027.
[100] J.G. Kaufman, E. Rooy, Aluminum alloy castings: properties, Processes And Applications (2004).
[101] R. Doglione, In situ investigations on the ductility of an Al-Si-Mg casting alloy, JOM 64 (1) (2012) 51–57.
[102] W. Yu, H. Zhao, L. Wang, Z. Guo, S. Xiong, The influence of T6 treatment on fracture behavior of hypereutectic Al-Si HPDC casting alloy, J. Alloys. Compd. 731 (2018) 444–451.
[103] F. Gao, Z. Fan, Competition for nucleation and grain initiation during solidification, Metals (Basel) 12 (9) (2022) 1512.
[104] G. Gottstein, Solidification, in: G. Gottstein (Ed.), Physical Foundations of Materials Science, Springer, Berlin Heidelberg, Berlin, Heidelberg, 2004, pp. 357–388.
[105] H. Cao, Z. Luo, C. Wang, J. Wang, T. Hu, L. Xiao, J. Che, The stress concentration mechanism of pores affecting the tensile properties in vacuum die casting metals, Materials (Basel) (2020).
[106] M. Waldemar, T. Oscar, C. César, G. César, Effect of porosity on the tensile properties of low ductility aluminum alloys, Mater. Res. 7 (2004).
[107] C. Puncreobutr, P.D. Lee, K.M. Kareh, T. Connolley, J.L. Fife, A.B. Phillion, Influence of Fe-rich intermetallics on solidification defects in Al–Si–Cu alloys, Acta Mater. 68 (2014) 42–51.

[108] J. Mathew, M.A. Williams, P. Srirangam, X-ray computed tomography studies on porosity distribution in vacuum induction cast Al-7Si alloys, JOM 73 (12) (2021) 3866–3872.
[109] A.M. Samuel, E. Samuel, V. Songmene, F.H. Samuel, A review on porosity formation in aluminum-based alloys, Materials (Basel) (2023).
[110] D.-F. Song, Y.-L. Zhao, Z. Wang, Y.-W. Jia, D.-X. Li, Y.-N. Fu, D.-T. Zhang, W.-W. Zhang, 3D Fe-rich phases evolution and its effects on the fracture behavior of Al–7.0Si–1.2Fe alloys by Mn neutralization, Acta Metall. Sin.-Engl. Lett. 35 (1) (2022) 163–175.
[111] C. Puncreobutr, A.B. Phillion, J.L. Fife, P. Rockett, A.P. Horsfield, P.D. Lee, In situ quantification of the nucleation and growth of Fe-rich intermetallics during Al alloy solidification, Acta Mater. 79 (2014) 292–303.
[112] S.G. Shabestari, The effect of iron and manganese on the formation of intermetallic compounds in aluminum–silicon alloys, Mater. Sci. Eng. A 383 (2) (2004) 289–298.
[113] K.F. Kelton, A.L. Greer, Chapter 4 - beyond the classical theory, in: K.F. Kelton, A. L. Greer (Eds.), Pergamon Materials Series, 2010, pp. 85–123. Pergamon.
[114] D. Gebauer, P. Raiteri, J. Gale, H. Cölfen, On classical and non-classical views on nucleation, Am. J. Sci. 318 (2018) 969–988.
[115] S. Karthika, T.K. Radhakrishnan, P. Kalaichelvi, A review of classical and nonclassical nucleation theories, Cryst. Growth Des. 16 (11) (2016) 6663–6681.
[116] J. Lacaze, L. Eleno, B. Sundman, Thermodynamic assessment of the aluminum corner of the Al-Fe-Mn-Si system, Metall. Mater. Trans. A 41 (9) (2010) 2208–2215.